Technische Universität München
Fakultät für Physik
Lehrstuhl für Physik funktionaler Schichtsysteme, E10

Low damping and linearly polarized GHz magnetization dynamics in the chiral magnet Cu_2OSeO_3 hosting spin helices and skyrmions

Ioannis Stasinopoulos

Vollständiger Abdruck der von der Fakultät für Physik der Technischen Universität München zur Erlangung des akademischen Grades eines

Doktors der Naturwissenschaften

genehmigten Dissertation.

Vorsitzender:	Prof. Dr. Michael Knap
Prüfer der Dissertation:	1. Prof. Dr. Dirk Grundler
	2. Prof. Dr. Christian Pfleiderer

Die Dissertation wurde am 15.12.2016 bei der Technischen Universität München eingereicht und durch die Fakultät für Physik am 17.03.2017 angenommen.

Abstract

The insulating chiral magnet Cu_2OSeO_3 hosting topologically nontrivial spin order (Skyrmions and spin helices) is investigated via broadband microwave spectroscopy. We show that the spin helices exhibit linearly polarized magnetization dynamics at an unexpectedly small frequency of about 2 GHz. The two eigenmodes are cross-polarized, leading to linear dichroism in Cu_2OSeO_3. A Gilbert damping parameter of 1×10^{-4} is measured for geometrically confined spin waves at 5 K. Using pulsed induced microwave magnetometry, we find that depending on the waveguide used, the relaxation time of the helix eigenmodes varies up to 30 times due to dephasing.

Zusammenfassung

Es wird der isolierende chirale Magnet Cu_2OSeO_3 mit nichttrivialer Spinordnung (Skyrmionen und Spinhelices) anhand breitbandiger Mikrowellenspektroskopie untersucht. Wir zeigen, dass die Spinhelices linear polarisierte Magnetisierungsdynamik bei einer unerwartet kleinen Frequenz von 2 GHz aufweisen. Die beiden Eigenmoden sind kreuz-polarisiert und führen zu linearem Dichroismus in Cu_2OSeO_3. Ein Gilbert-Dämpfungsparameter in Höhe von 1×10^{-4} wird für geometrisch beschränkte Spinwellen bei 5 K gemessen. Mittels gepulster Induktions-Mikrowellen-Magnetometrie finden wir heraus, dass die Relaxationszeit der helikalen Eigenmoden abhängig von dem verwendeten Wellenleiter wegen Dephasierung bis zu einem Faktor 30 variiert.

Contents

ABSTRACT i

INTRODUCTION vii

1 THEORETICAL ASPECTS 1
1.1 Energy contributions 1
1.2 Magnetization dynamics in ferromagnets 7
1.2.1 Equation of motion & ferromagnetic resonance 7
1.2.2 Influence of cubic anisotropy 12
1.2.3 Spin relaxation and Gilbert damping . . . 13
1.2.4 Ellipticity 15
1.3 The chiral magnet Cu_2OSeO_3 18
1.4 Magnetization dynamics in chiral magnets 23
1.4.1 Ginzburg-Landau model 23
1.4.2 Magnetic resonance 24

2 EXPERIMENTAL ASPECTS 33
2.1 High-frequency basics 33
2.1.1 Transmission line theory 33
2.1.2 Skin effect 39
2.1.3 Scattering parameters 40
2.2 Measurement principle 44
2.2.1 CPW Field distribution 46
2.2.2 Excitation profile 53
2.3 He-flow cryostat 59
2.3.1 Measurement procedure 62

2.3.2 Calibration and signal-to-noise ratio 63
2.4 Pulsed induced microwave magnetometry 65
2.5 Variable temperature insert 69
2.5.1 Experimental apparatus 69
2.5.2 3D field access 74
2.5.3 Angle calibration 75
2.5.4 Measurement procedure 75
2.6 Sample preparation 77
2.6.1 Preparation of coplanar waveguides 77
2.6.2 Preparation of Cu_2OSeO_3 samples 79

3 OPTIMIZATION OF COPLANAR WAVEGUIDES 81
3.1 Quasi-static approach 81
3.1.1 Conformal mapping 81
3.1.2 CPW modes 83
3.2 Electromagnetic simulations 88
3.2.1 Taper design 88
3.2.2 General optimization algorithm 91

4 MAGNETIC RESONANCE IN THE FIELD-POLARIZED PHASE 93
4.1 Gilbert damping 93
4.2 Magnetostatic waves in a bounded medium . . . 104
4.3 Cubic anisotropy 109

5 MAGNETIC RESONANCE IN THE NONCOLLINEAR SPIN PHASES 111
5.1 Linearly polarized magnetization dynamics 111
5.2 Cubic anisotropy 127
5.3 VTI measurements 129
5.4 Time-resolved dynamics 133

6 SUMMARY AND OUTLOOK 143

A LIST OF SAMPLES 147

B CPW DIMENSIONS 149

C SIMULATION PARAMETERS 151

BIBLIOGRAPHY 153

LIST OF ABBREVIATIONS 171

LIST OF FIGURES 173

ACKNOWLEDGEMENTS 177

LIST OF PUBLICATIONS 181

Introduction

Chiral magnets is a material class hosting complex chiral spin order, i.e. spin helices and magnetic Skyrmions. The latter are topologically stable vortex-like spin whirls induced by the lack of inversion symmetry in the atomic unit cell. While they were initially predicted in the field of particle physics, a hexagonal Skyrmion lattice (SkL) was observed by Mühlbauer *et al.* via small-angle neutron scattering experiments in the chiral magnet MnSi for the first time in 2009 [Müh09]. A year later, Jonietz *et*

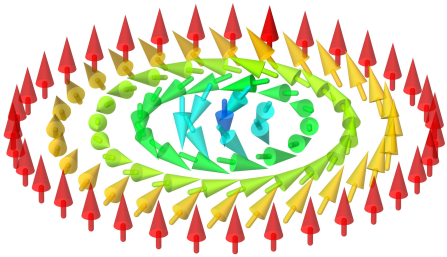

Figure 1: Schematic representation of a chiral Skyrmion. Arrows denote spins of electrons. The central spin (blue) points against the magnetic field. Image from [Eve12].

al. detected the rotation of the Skyrmion lattice under a remarkably low electric current density in the order of $\mu A\,m^{-2}$ [Jon10]. Based on this property, related to the weak pinning of the SkL to crystal defects, new perspectives for the design of low-

energy-consumption devices were proposed [FCS13; Sam13]. Additionally, spin-polarized current-driven creation and anihilation of individual Skyrmions in ultrathin magnetic films has been achieved [Rom13]. These findings open the way towards technological applications, such as the realization of logic elements [ZEZ15] and information storage systems [Kan16; Wie16; ZEZ15].

For the emerging field of magnonics, which deals with collective spin excitations (magnons) [KDG10; KG14], the SkL is of high interest, since it represents a self-organized, periodic modulation of magnetic properties. The lattice constant at the 10 nm scale is not routinely feasible via state-of-the-art nanolithography. The collective spin dynamics of the SkL lie in the GHz range and are probed by microwave absorption experiments. Theoretical calculations about the expected eigenmodes in all the phases of a chiral magnet were presented by Mochizuki *et al.* and were experimentally observed by Onose *et al.* in 2012 [Moc12; Ono12]. Schwarze *et al.* measured the eigenmodes of a metallic, a semiconducting and an insulating chiral magnet and modelled the dynamics by a universal mean-field theory [Sch15].

The development of future magnon-based devices for microwave applications requires in particular materials with a low spin wave damping [Chu15; KG14; ZD11]. Insulating compounds are advantageous over metals as they avoid damping via eddy currents at high-frequencies and magnons scattering at free charge carriers [GM96; Spa64]. Indeed, metals have not yet reached the remarkably low level of damping [Sch16] in the ferrimagnetic insulator yttrium-iron-garnet (YIG), which holds the benchmark with a Gilbert damping parameter $\alpha_{\text{intr}} = 3 \times 10^{-5}$ at room temperature [SCH10].

Low damping chiral magnets would generate new prospects by particularly combining complex spin order with long-distance

magnon transport in future devices. At low temperatures, they would further enrich the physics in magnon-photon cavities that call for materials with small α_{intr} to achieve high-cooperative magnon-to-photon coupling in the quantum limit [Gor14; Hue13; Tab14; Zha14]. The discovery of the SkL in the insulating chiral magnet Cu_2OSeO_3 [Sek12] is thus of particular interest in this respect. Schwarze *et al.* presented promising preliminary results on the damping in this compound, compared to other chiral magnets [Sch15]. Additional functional aspects were reported in Cu_2OSeO_3: dichroism for microwaves caused by the magnetoelectric coupling [Moc15; Oka13; Oka15] and nonreciprocal wave propagation at large wave vector k [Sek16] induced by the antisymmetric Dzyaloshinskii-Moriya interaction (DMI). The control of Skyrmions with electric fields is another functional aspect to be pursued in the future [MW15; SIT12].
A stable SkL was found in a metallic Co-Zn-Mn alloy beyond 300 K [Tok15]. Furthermore, several groups reported the observation of room temperature Skyrmions in transition-metal-based magnetic multilayers [Bou16; But15; Jia15; Mor16; Woo16; Yu16]. In these kind of systems, a large DMI is induced by the symmetry breaking at the interface [BR01; CL98]. However, the design of an insulating chiral magnet at room temperature remains a challenge.

This thesis is structured as follows: Chapter 1 introduces basic theoretical concepts. In Chapter 2 we describe the experimental methods used and developed in this work. In Chapter 3 we give an outline of the optimization procedure for the design of coplanar waveguides (CPWs). The results obtained from magnetic resonance measurements in the field-polarized and noncollinear spin phases of Cu_2OSeO_3 are presented in Chapter 4 and 5,

respectively. Finally, we give a summary and outlook of this work in Chapter 6.

1 Theoretical Aspects

1.1 Energy contributions

The *magnetization* of a material is defined as the sum of the magnetic moments $\mathbf{m}_i$ of N magnetic dipoles in a given volume V

$$\mathbf{M} = \frac{\sum_{i=1}^{N} \mathbf{m}_i}{V}. \tag{1.1}$$

The response to an external magnetic field $\mu_0 H$ is described by the magnetic *susceptibility tensor* $\underline{\chi}$ [OHaoo], so that

$$\mathbf{M} = \underline{\chi}\mathbf{H}. \tag{1.2}$$

The magnetic *flux density* $\mathbf{B}$ consists of the contribution from the external magnetic field H and the response of the material

$$\mathbf{B} = \mu_0(\mathbf{M} + \mathbf{H}) = \mu_0(\underline{\chi} + \underline{1})\mathbf{H}. \tag{1.3}$$

If the latter is homogeneous and isotropic, the tensor $\underline{\chi}$ reduces to a scalar entity χ. In *ferromagnetic* materials $\chi \gg 0$. Here, the magnetization is maintained even after removal of the external magnetic field. In contrast, *paramagnetic* materials exhibit significantly smaller values $\chi > 0$, and build up a finite magnetization $\mathbf{M}$ only when exposed to an external magnetic field.

Various fundamental interactions at the microscopic level determine the energy landscape inside a material and hence its type (ferromagnet, paramagnet, chiral magnet and others).

Exchange interaction

It results from the symmetry requirements on a many-electron wave function (*Pauli's exclusion principle*) [CDL86]. This interaction is described quantum-mechanically by the Heisenberg-exchange Hamiltonian for a spin lattice [AM76]

$$\mathcal{H}_{ex} = -\sum_{i,j} J_{i,j}\, \mathbf{S}_i \cdot \mathbf{S}_j, \tag{1.4}$$

with the exchange integral $J_{i,j}$ describing the overlap of the wave functions of a spin at the lattice site i and j, respectively. $\mathbf{S}_i$, $\mathbf{S}_j$ are the spin operators. In most cases, summation only over the next neighbors provides enough calculation accuracy due to the short-range nature of the exchange interaction, inherent from the small overlap of the wave functions [Kit66]. $J_{i,j} > 0$ and $J_{i,j} < 0$ favour parallel (ferromagnetism) and antiparallel spin alignment (antiferromagnetism), respectively.
In the continuum approach, we treat the magnetization $\mathbf{M}$ as a vector field $\mathbf{M}(\mathbf{r})$ with the location vector $\mathbf{r}$, varying slowly enough over the distance of a unit cell [Gie05] and obtain the scalar free energy

$$E_{ex} = \int dV\, J(\nabla \mathbf{M}(\mathbf{r}))^2. \tag{1.5}$$

Here we perform a volume integral, where J includes only nearest neighbor interactions and $\nabla = \partial/\partial x + \partial/\partial y + \partial/\partial z$.

Zeeman interaction

A magnetization $\mathbf{M}$ subjected to an external magnetic field $\mu_0\mathbf{H}$ contributes with the term

$$E_{\text{Zeeman}} = -\mu_0\, \mathbf{M} \cdot \mathbf{H} \tag{1.6}$$

to the free energy.

Dzyaloshinskii-Moriya interaction (DMI)

It is directly related to the spin-orbit coupling [Dzy58; Mor60]. The DMI is *antisymmetric* with respect to permutation of spins. It is present in lattice structures lacking inversion symmetry, as in the chiral magnet Cu_2OSeO_3 studied in this thesis. The corresponding Hamiltonian is given by

$$\mathcal{H}_{\text{DM}} = \mathbf{D}_{i,j} \cdot (\mathbf{S}_i \times \mathbf{S}_j), \tag{1.7}$$

with the Dzyaloshinskii-vector $\mathbf{D}_{i,j}$. The corresponding linear order term of the free energy is

$$E_{\text{DM}} = \int dV\, D\mathbf{M}(\mathbf{r}) \cdot (\nabla \times \mathbf{M}(\mathbf{r})), \tag{1.8}$$

with the coupling strength D.

The three types of interactions presented above form the primary structure-giving elements in our samples, i.e. these are sufficient to produce the spin configurations under observation. However, taking into account additional *secondary* energy contributions is necessary for an accurate description of the spin system in real samples. These are the demagnetization and crystal anisotropy energy.

Demagnetization energy

The long-ranged dipolar interactions between the spins [Kit47] favour antiparallel spin orientation to minimize stray fields. An additional effective magnetic field H_{dem} is introduced to describe this effect. Its derivation holds only for the *magnetostatic* case defined by

$$\mu_0 \nabla \cdot (\mathbf{M} + \mathbf{H}_{dem}) = 0 \tag{1.9}$$

$$\nabla \times \mathbf{H}_{dem} = 0. \tag{1.10}$$

These are Maxwell's equations for the overall magnetic field inside the sample $\mathbf{M} + \mathbf{H}_{dem}$ under the absence of an external magnetic field $\mu_0 \mathbf{H}$, time-varying electric fields and electrical currents. In analogy to the electrostatic case [Jac62], where the electrical charge density $\rho(\mathbf{r})$ generates the electric field

$$\mathbf{E}(\mathbf{r}) = -\int d\mathbf{r}' \, \nabla_{\mathbf{r}} \frac{\rho(\mathbf{r}')}{|\mathbf{r} - \mathbf{r}'|}, \tag{1.11}$$

so-called magnetic *surface charges* $\sigma_M = \mathbf{n}(\mathbf{r})\mathbf{M}(\mathbf{r})$ are assumed to generate the demagnetizing field

$$\mathbf{H}_{dem}(\mathbf{r}) = -\frac{\mathbf{M}}{4\pi} \int_S dS' \, \nabla_{\mathbf{r}} \frac{\mathbf{n}(\mathbf{r}')}{|\mathbf{r} - \mathbf{r}'|} = -\underline{N}(\mathbf{r})\mathbf{M}. \tag{1.12}$$

$\underline{N}$ and $\mathbf{n}$ is the *demagnetizing tensor* and the surface normal vector of the magnetic sample respectively. The integration is carried out over the surface S of the sample. Equation (1.12) is valid only if the magnetization is uniform $\mathbf{M}(\mathbf{r}) = \mathbf{M}$ [Gie05]. Although $\underline{N}$ is space-dependent in general, it is independent of the position $\mathbf{r}$ if $\mathbf{M}$ lies along a main axis of an ellipsoid. In this case, diagonalization of $\underline{N}$ is possible, the corresponding tensor elements N_i $(i = x, y, z)$ are independent of the scale of the sample and

$$N_x + N_y + N_z = \mathrm{Tr}[\underline{N}] = 1. \tag{1.13}$$

The dipolar energy contribution to the free energy reads

$$E_{dem} = -\frac{\mu_0}{2} \mathbf{M} \cdot \mathbf{H}_{dem}. \tag{1.14}$$

The factor $1/2$ acounts for the double counting within the spin pairs. We note that although the dipolar interaction is significantly weaker than the short-ranged exchange and DMI interactions, the contributions from all the spins in the sample, including distant ones, render both energy scales comparable. Finally, the similar structure of Eqs. (1.6) and (1.14) illustrates the fact that dipolar interactions are described by the presence of the magnetic field $\mathbf{H}_{dem}$.

Crystal anisotropy energy

The crystal lattice structure is mediated to the spins via the spin-orbit coupling. This results in an anisotropy of the spin orientation with respect to specific crystallographic axes. The corresponding free energy in the case of a simple uniaxial anisotropy (the crystal field imposes one specific direction to the magnetization) is given by [Vlao8]

$$E_{cryst,uni} = \int d\mathbf{r}\, K_1 \sin^2\theta, \tag{1.15}$$

where θ denotes the relative angle between the magnetization $\mathbf{M}$ of the sample and a specific anisotropy axis. K_1 is the first order anisotropy constant. For $K_1 > 0$ and $K_1 < 0$ the magnetization orients along (easy axis) and orthogonal (hard axis) to the specific crystallographic axis, respectively.
In this work we study bulk cubic crystals. In this case we ex-

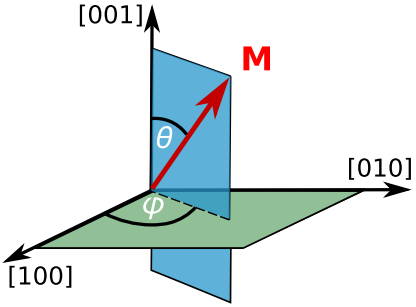

Figure 1.1: Angle definition for the calculation of the crystal anisotropy energy inside a sphere of cubic magnet.

presss the anisotropy energy with a power series in projections of the magnetization $\mathbf{M}$ on the crystal axes [GM96]

$$\begin{aligned} E_{cryst,cub} =& \frac{1}{4} K_1 \left(\sin^2 2\theta + \sin^4\theta \cdot \sin^2 2\phi\right) \\ &+ \frac{1}{16} K_2 \sin^2\theta \cdot \sin^2 2\theta \cdot \sin^2 2\phi, \end{aligned} \tag{1.16}$$

with θ being the angle between $\mathbf{M}$ and the cubic axis considered, and ϕ the angle in the basal plane perpendicular to this axis (Fig. 1.1). K_1 and K_2 are the first and second anisotropy constants, respectively.

All the contributions to the free energy of the system sum up to a total energy E_{tot} and we define the effective magnetic field comprising all the relevant interactions

$$\mathbf{H}_{eff} = -\frac{1}{\mu_0} \nabla_{\mathbf{M}} E_{tot}. \tag{1.17}$$

$\mathbf{H}_{eff}$ enters the description of the magnetization dynamics, that will be introduced in Section 1.2.

1.2 Magnetization dynamics in ferromagnets

1.2.1 Equation of motion & ferromagnetic resonance

The magnetic moment of an electron is defined based on its angular momentum $\mathbf{l}$ as

$$\mathbf{m} = -\frac{g\mu_B}{\hbar}\mathbf{l} = -\gamma\mathbf{l}, \tag{1.18}$$

with the free-electron g-factor $g \approx 2$, the Bohr magneton μ_B and the reduced Plack's constant $\hbar$. The negative sign enters due to the negative electron charge. The *gyromagnetic ratio* $\gamma = g\mu_B/\hbar$ is the relating entity between the magnetic moment and the mechanical angular momentum. It is characteristic of the magnetic system and its exact value may vary e.g. in the presence of strong spin-orbit coupling originating from a crystal field in a solid.
We now average over all magnetic moments in a sample according to Eq. (1.1), to obtain the total angular momentum $\mathbf{L}$. The fundamental relationship between the mechanical torque $\mathbf{T}$ and $\mathbf{L}$ yields

$$\mathbf{T} = \frac{d\mathbf{L}}{dt} = -\frac{1}{\gamma}\frac{d\mathbf{M}}{dt}, \tag{1.19}$$

where Eq. (1.18) has been used.
As presented in Section 1.1, the effective field $\mathbf{H}_{eff}$ (1.17) describes all the relevant interactions in our samples. This field exerts a torque

$$\mathbf{T} = \mathbf{M} \times \mathbf{H}_{eff} \tag{1.20}$$

on the magnetization $\mathbf{M}$. Combining expressions (1.19) and (1.20), one obtains

$$\frac{d\mathbf{M}}{dt} = -\gamma\mathbf{M} \times \mathbf{H}_{eff}. \tag{1.21}$$

Equation (1.21) describes a precessional motion[1] of $\mathbf{M}$ around $\mathbf{H}_{\text{eff}}$ at the *Larmor frequency*

$$\omega_L = -\gamma H_{\text{eff}} = \frac{g\mu_B}{\hbar} H_{\text{eff}}. \tag{1.22}$$

In reality, damping mechanisms force $\mathbf{M}$ into a spiral path and alignment with $\mathbf{H}_{\text{eff}}$. This is illustrated in Fig. 1.2 (b). A *phe-*

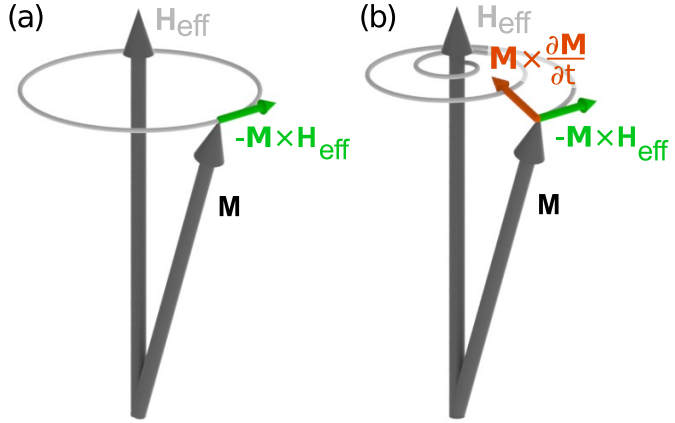

Figure 1.2: (a) Precessional motion of the macrospin $\mathbf{M}$ around the effective magnetic field $\mathbf{H}_{\text{eff}}$ without damping. (b) The damping (red) combined with the torque from the effective field (green) drive $\mathbf{M}$ along a spiral path before aligning with $\mathbf{H}_{\text{eff}}$.

nomenological description of weak damping was given by by Gilbert [Gil04] leading to the Landau-Lifshitz-Gilbert (LLG) equation

$$\frac{d\mathbf{M}}{dt} = -\gamma\mu_0\, \mathbf{M} \times \mathbf{H}_{\text{eff}} + \frac{\alpha_{\text{intr}}}{M_s}\left(\mathbf{M} \times \frac{d\mathbf{M}}{dt}\right), \tag{1.23}$$

1 The precessional motion is proven by showing that $\frac{d\mathbf{M}^2}{dt} = 0$ and $\frac{d(\mathbf{M}\mathbf{H}_{\text{eff}})}{dt} = 0$ [Gie05].

with the phenomenological, dimensionless intrinsic Gilbert damping parameter α and the saturation magnetization M_s. Note that within a classical approach, the precession described by Eq. (1.23) applies also to a microscopic magnetic moment $\mathfrak{m}$ (after adapting the prefactors).

In the prospect of linearizing the LLG equation, we decompose the magnetization and *external* field into equilibrium and dynamic components:

$$\mathbf{M} = \mathbf{M}_{\text{equ}} + \mathfrak{m}(t) \tag{1.24}$$

$$\mathbf{H} = \mathbf{H}_{\text{equ}} + \mathfrak{h}(t) \tag{1.25}$$

We now make the following assumptions:

(i) $|\mathbf{M}_{\text{equ}}| \approx M_s$,

(ii) the precession takes place at small angles, which implies together with $\frac{d\mathbf{M}^2}{dt} = 0$ (conservation of the modulus $|\mathbf{M}|$) that $\mathfrak{m} \perp \mathbf{M}_{\text{equ}}$ in good approximation,

(iii) the demagnetizing tensor $\underline{N}$ is diagonal, i.e. the sample is well-described by an ellipsoid and

(iv) the excitation $\mathfrak{h}(t) = \mathfrak{h}\, e^{i\omega t}$ and response from the sample $\mathfrak{m}(t) = \mathfrak{m}\, e^{i\omega t}$ is harmonic.

We insert this into the LLG equation (1.23) and retain only linear terms. The solution of the resulting differential equation $\mathfrak{m}(t) = \underline{\chi}(\omega)\mathfrak{h}(t)$ is expressed with the help of the frequency dependent *dynamic susceptibility tensor* $\underline{\chi}(\omega)$ [Gie05].
We note that assumption (iv) concerning harmonic excitation applies in the case of our experiments (see Section 2.2), since we use the harmonically oscillating magnetic field of transverse electromagnetic waves (TEMs) as the source of the spin excitation.

Interestingly, assuming an *uniaxial* excitation field $\mathbf{h} = (h\,e^{i\omega t}, 0, 0)$ we obtain off-diagonal components in $\underline{\chi}(\omega)$. This means that a dynamic field $\mathbf{h}(t) \parallel \hat{e}_x$ induces a dynamic magnetization $\mathbf{m}(t)$ not only in $\hat{e}_x$ direction, but also along $\hat{e}_y$ [Vlao8]. Thus, a uniaxial excitation does not lead to a uniaxial oscillation of the magnetization.

Choosing

$$\mathbf{H} = \begin{pmatrix} h_x(t) \\ 0 \\ H_{equ} \end{pmatrix}, \tag{1.26}$$

we set

$$\mathbf{M} = \begin{pmatrix} m_x(t) \\ m_y(t) \\ M_s \end{pmatrix}, \tag{1.27}$$

due to the equilibrium condition $\mathbf{H}_{equ} \parallel \mathbf{M}_s$. We obtain the x-component of the dynamic susceptibility tensor [Gieo5]

$$\chi_{xx}(\omega) = \frac{\omega_M\left(\omega_H + (N_y - N_z)\omega_M - i\alpha_{intr}\omega\right)}{\left(\omega_r^2 - (1+\alpha_{intr}^2)\omega^2\right) - i\alpha_{intr}\omega\left[2\omega_H + (N_x + N_y - 2N_z)\omega_M\right]} \tag{1.28}$$

with $\omega_M = \gamma\mu_0 M_s$, $\omega_H = \gamma\mu_0 H_{equ}$ and

$$\omega_r = 2\pi f_r = \gamma\mu_0\sqrt{(H_{equ} + (N_x - N_z)M_s)(H_{equ} + (N_y - N_z)M_s)}. \tag{1.29}$$

Expression (1.29) is known as the *Kittel formula* or *Kittel mode* in ferromagnets [Kit48]. It describes the influence of demagnetization fields (see Section 1.1) defined by the *shape* of the sample on the resonance frequency of the spins f_r. Eq. (1.29) is a correction to the Larmor frequency ω_L (1.22) taking finite size effects into

account. We refer to Ref. [Vlao8] for a more detailed discussion on the influence of the sample shape on f_r. For the derivation of Eq. (1.29) we assumed a uniform excitation in the entire sample, which means that all spins precess in phase. This is referred to as ferromagnetic resonance (FMR).
The real and imaginary parts[2] of $\chi_{xx}(f)$ are plotted in Fig. 1.3 for $\mu_0 H_{equ} = 0.5\,T$, $\mu_0 M_s = 0.131\,T$, $\gamma/2\pi = 28\,GHz/T$ and two different values for α_{intr}. The demagnetization factors for a rod-shaped sample[3] were chosen. $\mathrm{Re}[\chi_{yy}(f)]$ and $\mathrm{Im}[\chi_{yy}(f)]$ exhibit their inflection point and maximum, respectively, at the frequency $f' = f_r$ for vanishingly small α_{intr}. With increasing damping, f' shifts to lower values. In our case $f' = 12.90\,GHz$ and $f' = 12.72\,GHz$ for $\alpha_{intr} = 1 \times 10^{-4}$ and $\alpha_{intr} = 0.1$, respectively. Note also the slight asymmetry of the lineshapes with inceasing damping and the deviation of $\mathrm{Im}[\chi_{yy}(f)]$ from a Lorentzian lineshape (blue dashed line).

Finally, we explain why we refrained from using $\mathbf{H}_{eff}$ [Eq. (1.17)] instead of the external field in the expressions above. In the case of chiral magnets, $\mathbf{H}_{eff}$ is characterized among others by the DMI, which produces noncollinear spin textures described by a nontrivial distribution $\mathbf{M}(\mathbf{r})$ inside the sample. In this section, we assumed a homogeneous magnetization inside the sample. The approach outlined above for the description of the dynamics thus retains its validity only in the field-polarized phase of chiral magnets (see Section 1.3). In the noncollinear spin phases, a Ginzburg-Landau mean-field model has been developed, which will be presented in Sec. 1.4.

2 For the corresponding analytical expressions, we refer to Ref. [Gieo5].
3 $N_x = 0.07$, $N_y = 0.40$, $N_z = 0.53$. See also Appendix A.

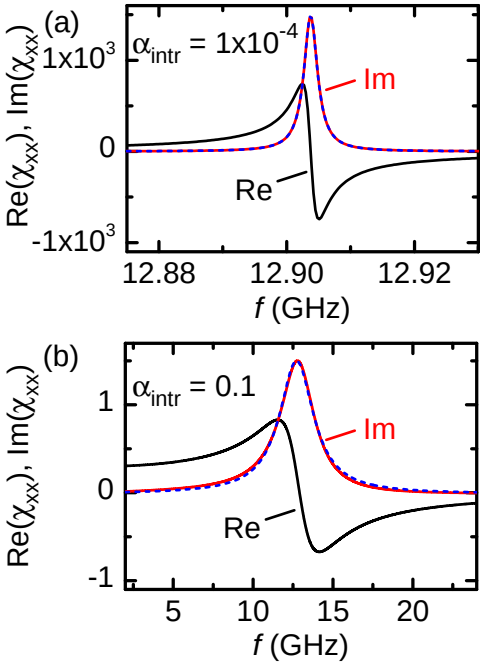

Figure 1.3: Real and imaginary parts of the dynamic susceptibility χ_{xx} as a function of the frequency f for (a) $\alpha_{intr} = 1 \times 10^{-4}$ and (b) $\alpha_{intr} = 0.1$. A slight deviation of the fitted Lorentzian lineshapes (blue dashed line) is observed with increasing α_{intr}.

1.2.2 Influence of cubic anisotropy

We now present an extended version of the Kittel formula (1.29) including the influence of cubic anisotropy (see Section 1.1) on the resonance frequency f_r of a ferromagnet or, equivalently,

a field-polarized chiral magnet. We consider the Hamiltonian density

$$\mathcal{H} = \frac{\mu_0}{2}\,\mathbf{M}\cdot\underline{N}\cdot\mathbf{M} + \frac{K}{M_s^4}\left(M_x^4 + M_y^4 + M_z^4\right) - \mathbf{B}_{ext}\cdot\mathbf{M}. \quad (1.30)$$

with the (first) anisotropy constant K and the externally applied magnetic flux density $\mathbf{B}_{ext}$. We then obtain [GM96]

$$f_r = \frac{\gamma}{2\pi}\Bigg\{\left(4\frac{K}{M_s} - (B_{ext} + \mu_0 M_s\,(N_x - N_z))\right) \left(4\frac{K}{M_s} - (B_{ext} + \mu_0 M_s\,(N_y - N_z))\right)\Bigg\}^{1/2} \quad (1.31)$$

and

$$f_r = \frac{\gamma}{2\pi}\Bigg\{\left(\frac{8}{3}\frac{K}{M_s} + (B_{ext} + \mu_0 M_s\,(N_x - N_z))\right) \left(\frac{8}{3}\frac{K}{M_s} + (B_{ext} + \mu_0 M_s\,(N_y - N_z))\right)\Bigg\}^{1/2} \quad (1.32)$$

for $\mathbf{H} \parallel \langle 100\rangle$ and $\mathbf{H} \parallel \langle 111\rangle$, respectively.

1.2.3 Spin relaxation and Gilbert damping

In this Section we discuss the origin of the damping in magnetic materials and compare different evaluation routes. Spin relaxation takes place via energy dissipation within the magnetic system or from the magnetic system to e.g. the phonons [Leno6; SLK61]. Such damping mechanisms lead to *intrinsic* linewidth broadening by imposing a finite lifetime τ to the magnetization

precession, independent of the excitation or detection process. In insulating materials, localized magnetic moments act as scattering sites for magnons [Zak07]. Also, magnon-phonon interactions contribute significantly to the damping. Relaxation in metallic samples on the other hand is mainly determined by scattering at free charge cariers [GM96; Rez13]. Furthermore, the presence of eddy currents and other effects can also contribute to the damping [HUW02]. Finally, we note that an inhomogeneous spin excitation causes *extrinsic* linewidth broadening [VB10]. We address this in Section 4.1.

The intrinsic Gilbert damping parameter α_{intr} is typically determined from FMR experiments with field modulation. When extracting the field linewidth ΔH at a fixed resonance frequency f_r, ΔH is assumed to vary according to [HCH85; Kal06]

$$\mu_0 \gamma \cdot \Delta H = 4\pi \, \alpha_{\text{intr}} \cdot f_r + \mu_0 \gamma \cdot \Delta H_0, \tag{1.33}$$

where ΔH_0 is the contribution due to inhomogeneous broadening. This approach describes viscous damping, i.e. the linewidth increases linearly with frequency and Eq. (1.33) is valid as long as this type of damping dominates over nonlinear effects, e.g. scattering within the magnetic subsystem [Len06].
When performing frequency-swept measurements at a fixed field H, the linewidth Δf obtained is considered to scale linearly with the resonance frequency as [Pat68]

$$\Delta f = 2 \, \alpha_{\text{intr}} \cdot f_r + \Delta f_0, \tag{1.34}$$

with the inhomogeneous broadening Δf_0. The conversion from Eq. (1.33) to Eq. (1.34) is valid when f_r scales linearly with H and $\mathbf{H}$ is applied along a magnetic easy or hard axis of the material [FZ13; KCC05].

The relaxation time τ_0 attributed to a homogeneous excitation (FMR) is given by [Sta93]

$$\tau_0^{-1} = 2\pi\,\alpha_{\text{intr}} \cdot f(k=0), \tag{1.35}$$

where $f(k=0)$ is the FMR frequency. τ_0 differs however from τ_k, the relaxation time under an inhomogeneous excitation. Following Ref. [Sta93], one finds

$$\tau_k^{-1} = \frac{f(k=0)^2 + f^2}{2\tau_0 f \cdot f(k=0)} \tag{1.36}$$

for spin waves in the region of small wave vectors k. When evaluating damping parameters in this work, we will consider frequencies f that are close to f_0. In this case, $\tau_k \approx \tau_0$ and the evaluated Gilbert parameter represents a good estimate for α_{intr}.

1.2.4 Ellipticity

We define the ellipticity of the homogeneous dynamic magnetization $\mathbf{m}(t)$ oscillating in the xy plane as

$$|\varepsilon| = \frac{\sqrt{|m_x{}^2 - m_y{}^2|}}{\max[m_x, m_y]}. \tag{1.37}$$

According to the orthodox understanding of magnetic resonance [GM96], inside a general ellipsoid of a field-polarized ferromagnetic material, ε is given by

$$\varepsilon = \sqrt{(N_y - N_x)/(N_y - N_z + H/M)}, \tag{1.38}$$

where M is the static magnetization pointing along $\hat{z}$, parallel to the external field $\mathbf{H}$ and N_i ($i = x, y, z$) are the components of

the demagnetization tensor with $N_x + N_y + N_z = 1$. Note that we restrict our discussion to $N_y \geqslant N_x$, for which Eq. (1.38) is valid[4].
We plot the latter as a function of N_x for several values of H ranging from $H = N_z M$ to $H = 3M$ in Fig. 1.4. Here we con-

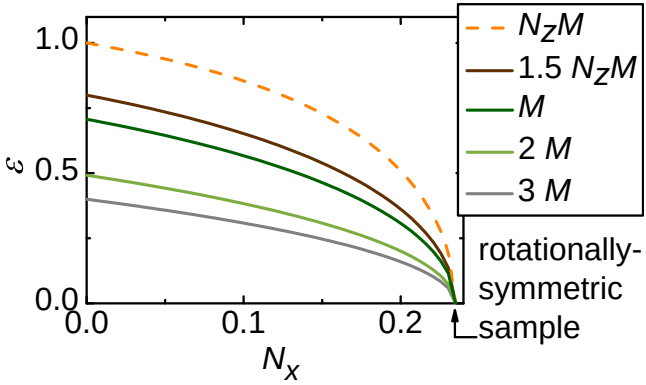

Figure 1.4: Ellipticity ϵ of the magnetization precession in a ferromagnet for different values of H as a function of the demagnetization factor N_x. We assume $N_z = 0.53$. An oscillating linearly polarized $\epsilon = 1$ magnetization is not realized.

sider $N_z = 0.53$ without loss of generality[5]. M is kept as a free parameter and $N_y = 1 - N_z - N_x$. We plot the results up to $N_x = 0.235 = N_y$.
For a rotationally-symmetric sample shape ($N_x = N_y$), the oscillating magnetization is circularly polarized with ellipticity $\varepsilon = 0$ at all fields. For $N_x < N_y = 1 - N_z - N_x (= 0.235$ in this case), the polarization is elliptically deformed so that $\varepsilon > 0$. The max-

4 For $N_y < N_x$, exchange N_x and N_y in Eq. (1.38).
5 $N_z = 0.53$ is the value corresponding to the samples measured in this work (see Chapter 5.1).

imum value of ε is obtained in the limit of zero internal field $H_{int} = H - N_z M = 0$ (orange dashed line), where

$$\varepsilon(H_{int} = 0) = \sqrt{1 - N_x/N_y}. \tag{1.39}$$

In the limit $\epsilon \to 1$, we get $N_x/N_y \to 0$. At the same time, the Kittel resonance frequency reduces to

$$\omega(H_{int} = 0) = \gamma\mu_0 M\sqrt{N_x N_y}. \tag{1.40}$$

and vanishes as $N_x/N_y \to 0$. Finally, below the shape-anisotropy field, i.e. $H < N_z M$, $H \parallel M$ can only be achieved in a sample with $N_x = N_y > N_z$. Here, we obtain $\epsilon = 0$ according to Eq. (1.38). In summary, we showed that the case $\epsilon = 1$, i.e. linear polarization of the uniform mode in a ferromagnet is not anticipated.

1.3 The chiral magnet Cu_2OSeO_3

In this work we study the cubic insulating compound Cu_2OSeO_3 with a B20 crystal structure [Bau14]. The atomic unit cell is shown in Fig. 1.5 and has an edge length of about 9 Å [EP86]. The Cu^{2+} sites are surrounded by a square pyramid

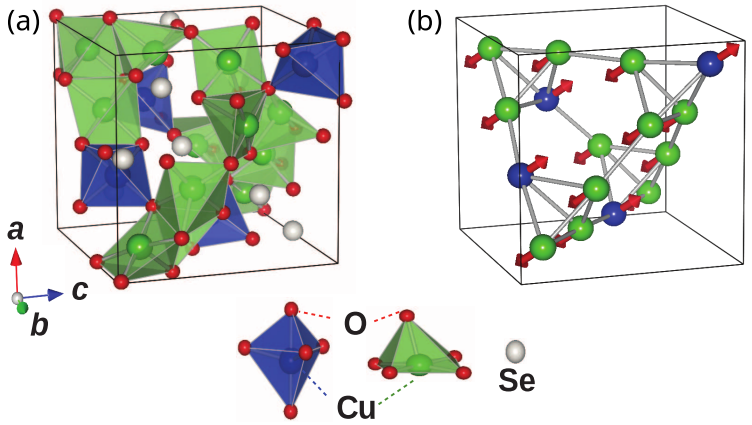

Figure 1.5: (a) Unit cell of Cu_2OSeO_3 consisting of Cu^{2+} ions surrounded by a square pyramid or trigonal bipyramid of oxygen atoms (see sketch below). (b) 3:1 ferrimagnetic alignment in the field-polarized phase resulting from the two copper ion sublattices. Figure adapted from Ref. [Sek12].

(green) and trigonal bipyramid (blue) of oxygen atoms (red spheres), respectively [Sek12]. Under an external field in the order of 100 mT or higher, this results in a 3:1 ratio of spins oriented parallel and antiparallel to the field direction, respectively [Fig. 1.5 (b)]. This *ferrimagnetic* alignment is stable up to 14 T [Bel10].
Due to the characteristic lack of inversion symmetry in the B20

crystal structure, non-inversion-symmetric magnetic structures are allowed [Eve12]. These result as an interplay of the DMI interaction and the exchange interaction (see Section 1.1), which favours perpendicular and parallel spin alignment, respectively. A helical spin configuration with a pitch vector $Q = 2\pi/\lambda_{helix}$ is formed, where Q is proportional to the ratio D/J of the DMI and exhange constant. Figure[6] 1.6 (a) illustrates this spin configuration (*helical phase*), which is stabilized below the critical temperature T_c and the critical magnetic field H_{c1}. The helix pitch length λ_{helix} amounts to 616 ± 45 Å in Cu_2OSeO_3 [Ada12]. Due to the crystal anisotropy, the spin helices align with **Q**

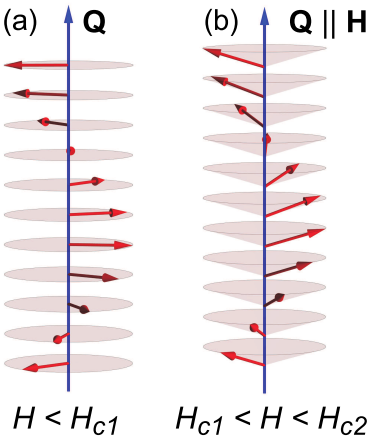

Figure 1.6: (a) Helical phase: the spins lie perpendicularly to the helix pitch vector **Q**. (b) Conical phase: for $H > H_{c1}$, **Q** is pinned along **H** and the spins cant towards the field direction.

along the four equivalent ⟨100⟩ directions at zero field. A finite external magnetic field $H > H_{c1}$ orients the pitch vectors parallel to its direction [BGP13; Eve12]. With further increasing

6 Johannes Waizner, private communication.

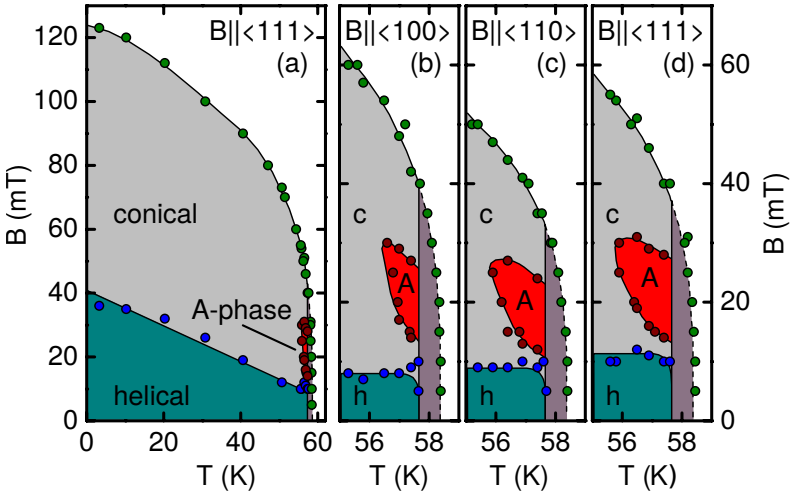

Figure 1.7: Phase diagram of Cu_2OSeO_3 for an external magnetic field applied along different crystallographic orientations. Below T_c, the SkL is stabilized within the narrow A-phase pocket (red). Figure taken from Ref. [Ada12].

field, the individual spins align towards the direction of **H** as illustrated in Fig. 1.6 (b). The material is then in the so called *conical phase*.

Above the second critical field H_{c2}, the spins are parallel with the magnetic field. Nevertheless, the ferrimagnetic configuration is retained. The material is in the *field-polarized (FP)* phase.

The phase diagram in Fig. 1.7 provides the reader with the absolute magnetic field and temperature values typical for Cu_2OSeO_3. We see that for a narrow temperature regime below T_c, the *A-phase* (red) is stabilized. The corresponding spin arrangement is illustrated in Fig.[7] 1.8. The spins form a vortex-like texture called "Skyrmion" with the outer spins pointing parallel (red) and the central one antiparallel (dark green) to

7 Johannes Waizner, private communication.

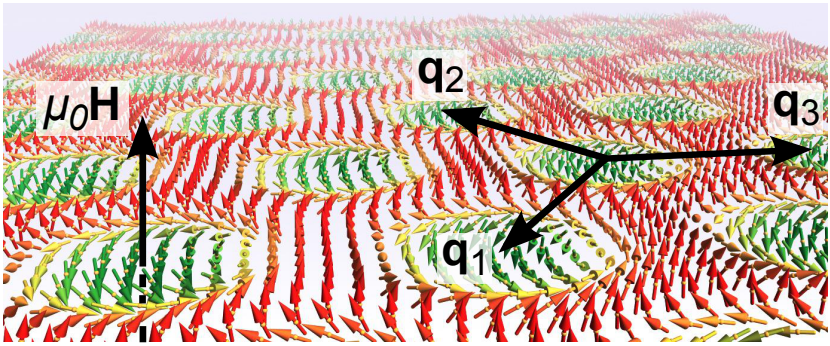

Figure 1.8: Sketch of the SkL with six-fold rotational symmetry. Small yellow spheres depict single electrons. Spins (arrows) pointing parallel and anti-parallel to the external magnetic field are depicted in red and green, respectively. In first order, the Skyrmion lattice is spanned by three helical pitch vectors $\mathbf{q}_i$ ($i = 1, 2, 3$) perpendicular to the externally applied field $\mathbf{H}$.

the external field direction. The rest of the spins cover the intermediate orientations (orange, yellow, light green).

Skyrmions in B20 compounds are stabilized in a narrow temperature regime by thermal fluctuations [BF13; Müho9]. They assemble in a triangular lattice building a two-dimensional Skyrmion Lattic (SkL) with a lattice parameter $2\lambda_{helix}/\sqrt{3}$ [Eve12]. The modulation of the spin orientation is described by three helical pitch vectors $\mathbf{q}_i$ ($i = 1, 2, 3$) in first order, i.e. the structure is well-defined in reciprocal space [Müho9].

A characteristic property of the SkL in B20 compounds is the decoupling from the atomic lattice. This means that the plane depicted in Fig. 1.8 lies perpendicular to the external magnetic field, regardless of the orientation of the latter relative to crystallographic axes [Eve12].

The SkL is a three-dimensional spin structure, where planes like

in Fig.[8] 1.8 are continuously repeated filling the sample volume. The spin configuration at the surface of B20 compounds, has been addressed in Refs. [Mil13; Zha16]. We note that recently, Tokunaga *et al.* found stable Skyrmions in a bulk crystal above room temperature [Tok15].

8 Johannes Waizner, private communication.

1.4 Magnetization dynamics in chiral magnets

1.4.1 Ginzburg-Landau model

In this section we present the approach developed by Johannes Waizner (University of Cologne) and Markus Garst (TU Dresden) for the theoretical description of collective spin excitations in chiral magnets[9]. The corresponding experimental data recorded in the framework of this thesis are presented in Chapter 5.
Chiral magnets exhibit complex, non-collinear spin textures, such as spin helices and Skyrmions (see Section 1.3). A mean-field approach based on a Ginzburg-Landau free energy functional of the magnetization containing a static and time-dependent part is set up in analogy to the total free energy E_{tot} (see Section 1.1)

$$\mathcal{F} = \mathcal{F}_0 + \mathcal{F}_{dip}. \tag{1.41}$$

$\mathcal{F}_0 = \int d\mathbf{r}\, f_0$ contains the energy density [BJ80; Nak80]

$$f_0 = \frac{1}{2}\phi(r - J\nabla^2)\phi + D\phi(\nabla \times \phi) + \frac{u}{4!}(\phi^2)^2 - \mu_0\mu\phi\mathbf{H}, \tag{1.42}$$

where dimensionless units are chosen for the field ϕ and the magnetization density $\mathbf{M} = \mu\phi$ is used. We use a single Bohr magneton per formula unit $\mu = \mu_B/V_{f.u.}$ and the interaction parameter u. $\mathbf{H}$ is the external magnetic field. The energy density r tunes the distance to the phase transition, J is the stiffness in Joule/meter, and D is the DMI constant in Joule/meter^2.

9 For a complete, pedagogical outline on this matter we refer to Refs. [Sch15; Wai13].

Let us consider an exciting magnetic field with spatial periodicity λ_h and corresponding reciprocal vector $k = 2\pi/\lambda_h$. With L being the linear size of the sample, we define the homogeneous excitation as $\lambda_h \gg L$. The contribution from the dipolar interaction F_{dip}, expressed in Fourier space to facilitate the calculation in the spin structures investigated in this thesis, is thus:

$$\mathcal{F}_{dip} = \frac{1}{2} \sum_{\mathbf{k}} \phi_i(-\mathbf{k}) \chi^{-1}_{dip\,ij}(\mathbf{k}) \phi_j(\mathbf{k}) \tag{1.43}$$

with the susceptibility $\chi^{-1}_{dip\,ij}$ given by

$$\chi^{-1}_{dip\,ij}(\mathbf{k}) = \mu_0 \mu^2 \begin{cases} \frac{k_i k_j}{k^2} & \text{if} \quad |\mathbf{k}| \gg 1/L \\ N_{ij} & \text{if} \quad |\mathbf{k}| \ll 1/L. \end{cases} \tag{1.44}$$

For momenta smaller than the inverse of the linear size of the sample L, the susceptibility is determined by the demagnetization tensor N_{ij}. Fourier components with momenta larger than $1/L$ interact via the dipolar interaction.

1.4.2 Magnetic resonance

To calculate the magnetic resonances in chiral magnets, we use the equation of motion (1.21), where the effective field $\mathbf{B}_{eff}$ is obtained via the functional $\mathbf{B}_{eff} = -\delta\mathcal{F}/\delta\mathbf{M}$. Linearizing Eq. (1.21) around the equilibrium configuration allows to determine the eigenmodes and eigenfrequencies. A magnetic time-dependent excitation induces a deviation from the equilibrium configuration $\mathbf{M}(\mathbf{r}, t) = \mu\phi(\mathbf{r}) + \mathbf{m}(\mathbf{r}, t)$, leading to an additional contribution to the effective field $\mathbf{B}_{eff,i}(\mathbf{r}, t)$. The latter is expanded in first order in the deviation $\mathbf{m}(\mathbf{r}, t)$ and contains a time-independent susceptibility $\chi^{-1}_{ij}(\mathbf{r}, \mathbf{k}') = \delta^2\mathcal{F}/(\delta\phi_i(\mathbf{r})\delta\phi_j(\mathbf{r}'))$,

evaluated with the equilibrium configuration of the magnetization. Inserting the latter into Eq. (1.21) and applying a Fourier transformation, one obtains the magnetic excitation spectrum from the eigenvalues of a characteristic matrix, where the amplitudes and the helix pitch orientation are determined by minimizing the corresponding potentials. The magnetic eigenfrequencies and its spectral weights are obtained by diagonalizing numerically the matrix. Analytical expressions for the eigenfrequencies under homogeneous excitation ($\mathbf{k} = 0$) are derived by this ansatz in the field-polarized and the conical phase. This is presented in below, after a short discussion on the influence of an inhomogeneous ac-field.

Spatially inhomogeneous ac field

We consider a spatially inhomogeneous magnetic ac field. As will be shown in Section 2.2.2, the typical momentum of the ac field distribution generated by our experimental setup is much smaller than intrinsic momentum scales determined by $Q = D/J$. For this reason, it is sufficient to confine the discussion to the small momentum limit of the magnetic resonances $\lim_{|\mathbf{k}|\to 0} \lim_{L\to\infty} \omega(\mathbf{k})$. This limit is non-analytic and it does not coincide with the resonance at zero momentum, $\lim_{|\mathbf{k}|\to 0} \lim_{L\to\infty} \omega(\mathbf{k}) \neq \omega(\mathbf{k} = 0)$, due to the long-range nature of the dipolar force [HK51]. Finally, the small momentum limit $\lim_{|\mathbf{k}|\to 0} \lim_{L\to\infty} \omega(\mathbf{k})$ depends on the orientation of the momentum $\mathbf{k}$, giving rise to a band of excitations around the resonances at zero momentum $\omega(0)$ that we will show in Section 5.1.

Field-polarized phase

We obtain a single excitation mode that couples to the magnetic ac field, in agreement with the standard ferromagnetic resonance. The resonance frequency is given by the Kittel formula (1.29). In the case $H > H_{c2}$, the magnetization is almost saturated and we can approximate $M \approx \chi_{con} H_{c2}$, so that the resonance frequency reads

$$\frac{\hbar\omega}{g\mu_0\mu_B H_{c2}} \approx \sqrt{\left[h + (N_x - N_z)\chi_{con}\right]\left[h + (N_y - N_z)\chi_{con}\right]} \tag{1.45}$$

with the reduced field $h = H/H_{c2} > 1$ and the susceptibility

$$\chi_{con} = \frac{\mu_0\mu^2}{JQ^2 + \mu_0\mu^2 N_z}. \tag{1.46}$$

Conical phase

Two eigenmodes with eigenfrequencies are found in the conical phase. They are characterized by the analytical expression

$$\begin{aligned}\frac{\hbar\omega^{\pm}}{g\mu_0\mu_B H_{c2}} = \Big\{ &\Big(1+\frac{1}{4}(N_x+N_y-4N_z)\chi_{con}\Big)\Big(2+(1-2N_z)\chi_{con}\Big)\\ &-h^2\Big(1+\chi_{con}(1+\frac{1}{4}(N_x+N_y-2N_xN_y)\chi_{con}\\ &-N_z(2+(1-N_z)\chi_{con}))\Big)\\ &\pm\frac{1}{4}\chi_{con}\Big[N_x^2\Big(2+(1-2N_z-h^2(1-2N_y))\chi_{con}\Big)^2\\ &+N_y^2\Big(2+(1-2N_z-h^2)\chi_{con}\Big)^2\\ &-2N_xN_y\Big((2+(1-2N_z)\chi_{con})^2\\ &+2h^2(4+(1+N_y-4N_z)\chi_{con})(-2-\chi_{con}+2N_z\chi_{con})\\ &+h^4(8+\chi_{con}(8+(1+2N_y)\chi_{con}\\ &+8N_z(-2+(-1+N_z)\chi_{con})))\Big)\Big]^{1/2}\Big\}^{1/2}. \end{aligned} \tag{1.47}$$

The right-hand side is a function of the reduced magnetic field $h = H/H_{c2} < 1$ and depends on the value of the susceptibility χ_{con} [Eq. (1.46)], that is constant within the conical phase.

In Fig. 1.9 (a), the equilibrium spin configuration in the conical phase is depicted. Note that the distance between adjacent spins is identical for all pairs, hence the helix is painted homogeneously yellow. The excitation by a homogeneous magnetic field leads to individual spin precession according to the LLG equation (1.23). This is illustrated by a red circular arrow in Fig. 1.9 (b). The simultaneous, phase-shifted precession of all the spins in the helix results in the formation of regimes with higher (red-shaded areas) and lower (green-shaded areas) spin density

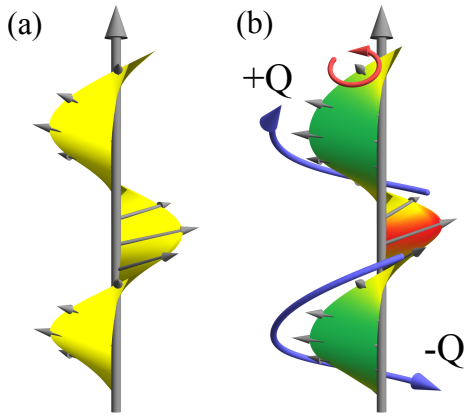

Figure 1.9: (a) Equilibrium spin configuration in the conical mode, where all the spins are equidistant. (b) Eigenmodes of the spin helix. The individual spin-precessional motion (red arrow) gives rise to the collective $\pm Q$ modes travelling along and against the pitch vector. Figure from Ref. [Sch15].

compared to the static case (yellow). These regimes propagate either parallel ($+Q$ mode) or antiparallel ($-Q$ mode) to the helix pitch vector. For $N_x = N_y$ and a right-handed chiral magnet with positive $D > 0$ in Eq. (1.42), the excitation with energy ω^+ corresponds to the $+Q$ mode. The $\pm Q$ helix eigenmodes are present both in the helical and in the conical phase. In general, they are excited at different frequencies. The ω^+ mode smoothly connects to the Kittel result in the limit $H \to H_{c2}$. In the same limit, one finds that the spectral weight of the magnetic resonance due to the ω^- mode vanishes. The internal susceptibility

$$\chi_{con}^{int} = \frac{\chi_{con}}{1 - \chi_{con} N_z} \tag{1.48}$$

is a measure for the strength of the dipolar interaction energy. In the limit $\chi_{con}^{int} \to 0$, Eq. (1.47) reduces to the simple expression

$\frac{\hbar\omega_\pm}{g\mu_0\mu_B H_{c2}} \to \sqrt{2-h^2}$ yielding a doubly degenerate excitation spectrum.
For a spherical sample with $N_i = 1/3$, we obtain

$$\begin{aligned}\left.\frac{\hbar\omega_\pm}{g\mu_0\mu_B H_{c2}}\right|_{N_i=1/3} &= \Big\{2 - \frac{\chi_{con}}{18} - h^2\Big(1 + \frac{\chi_{con}}{3} - \frac{\chi_{con}^2}{9}\Big) \\ &\pm h\frac{\chi_{con}}{18}\Big[\Big(6-\chi_{con}\Big)\Big(2(6+\chi_{con}) \\ &- 3h^2(2+\chi_{con})\Big)\Big]^{1/2}\Big\}^{1/2}. \qquad (1.49)\end{aligned}$$

While $\omega_\pm$ are degenerate at $h = 0$, expression (1.49) gives a non-degenerate spectrum for $h > 0$.

Helical phase

In the helical phase the mean magnetization is not longitudinal to the pitch vector in general and the cubic anisotropy needs to be taken into account. As in the conical phase, one obtains two modes with different magnetic excitation frequencies numerically [Sch15]. We did not observe a significant change in the eigenfrequency of the helical mode near T_c depending on the orientation of $\mathbf{H}$ relative to specific crystallographic axes (see Section 5.2). Therefore we limit ourselves to the use of Eq. (1.47) for modelling the eigenmodes in this phase.

Skyrmion lattice phase

In the SkL phase, two gyrational and one breathing mode are excited by a dynamic magnetic field perpendicular and parallel to the static external field, respectively [Moc12; Ono12; Sch15], as shown in Fig. 1.10. For the gyrational modes, the average

magnetization of each Skyrmion and hence its core rotate counterclockwise (CCW) and clockwise (CW), respectively. In the

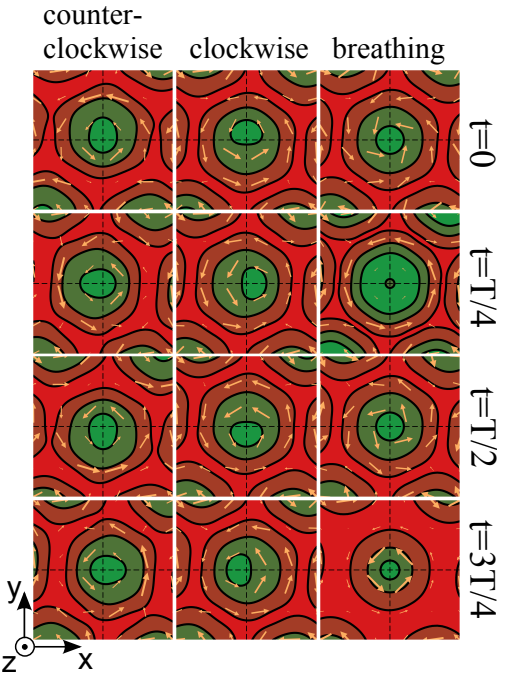

Figure 1.10: Excitation modes in the Skyrmion phase. From left to right: the three different excitation modes; from top to bottom: four "snapshots" during one period of oscillation T. The static magnetic field points along z and towards the observer. Yellow arrows illustrate the in-plane component of the magnetization. Spins point in z and $-z$ direction in the green and red regions, respectively. Figure from Ref. [Sch15].

breathing (BR) mode, the Skyrmion core expands and retracts periodically with time inside the ferromagnetic background. In the framework of this thesis, we address the experimental con-

ditions necessary to excite the different spin helix and Skyrmion modes selectively in Sections 5.1 and 5.3.

Overview of the eigenmodes

In Fig. 1.11 the theoretically expected resonance frequencies with respect to the external magnetic field are given for each phase. Colored areas in the background mark different phases

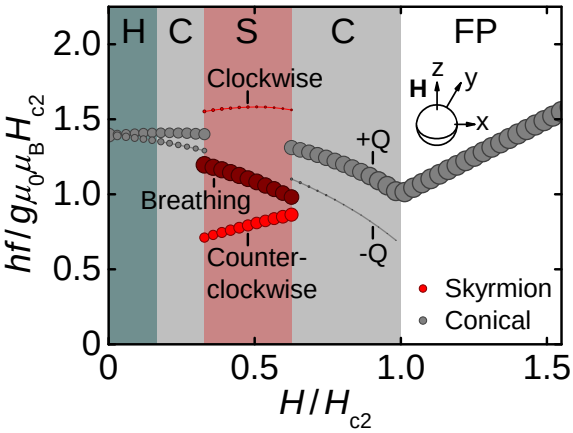

Figure 1.11: Theoretical expectations for the resonance frequencies of a sphere in normalized units taking into account the different phase regimes (colored areas in the background). The dot size scales with spectral weight.

(H: helical, C: conical, S: Skyrmion, FP: field-polarized). The mode in the FP phase is consistent with the Kittel formula (1.29). The calculation is based on the assumption of a homogeneous exciting magnetic field ($k = 0$). For the SkL the solution is solved numerically. The demagnetization factors for a sphere $N_i = 1/3$,

($i = x, y, z$) are used. In this case, the resonance frequency is not influenced by finite-size effects. We see that at zero field the conical modes are degenerate and that the $-Q$ is significantly weaker than the $+Q$ mode at $H > 0$. A large difference in spectral weight (symbol size) is also observed among the SkL modes. T. Schwarze *et al.* demonstrated the universal behavior of the dynamic excitations in chiral magnets by investigating the metallic MnSi, the semiconducting $Fe_{0.8}Co_{0.2}Si$ and the insulating Cu_2OSeO_3 [Sch15]. This is reflected in the use of normalized units in Fig. 1.11, which allows us to discuss the mode behavior in generic terms.

2 Experimental aspects

2.1 High-frequency basics

2.1.1 Transmission line theory

In this part we introduce the transmission line theory at high frequencies based on the references [Bil07] and [DS06].
In Fig. 2.1 a transmission line section of length $dx << \lambda$ is modeled. Four parameters describe the system: the series resistance R, the series inductance L, the shunt conductance G and the shunt capacitance C. All entities are expressed with respect to one length unit, i.e. per meter. V and I denote the voltage and current, respectively, at the beginning of the transmission line section. $V + dV$ and $I + dI$ are measured at the end of the line, R and G describe Ohmic and dielectric losses, respectively. The latter comprise losses due to leakage currents and polarization of the dielectric. We assume the following expressions for the space and time dependency of the voltage and current (sinusoidal excitation)

$$V(x,t) = Re[\tilde{V}(x)\, e^{i\omega t}] \tag{2.1a}$$

$$I(x,t) = Re[\tilde{I}(x)\, e^{i\omega t}] \tag{2.1b}$$

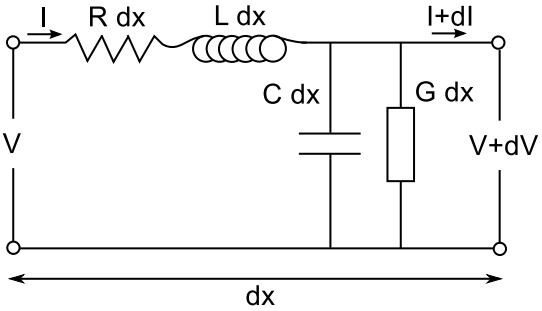

Figure 2.1: Equivalent circuit of a transmission line section dx. R and G describe the real losses of the transmission line.

with $\tilde{V}$ and $\tilde{I}$ the complex amplitudes at position x. The variation of the current $\frac{\partial I}{\partial x}$ and voltage $\frac{\partial V}{\partial x}$ along dx thus leads to the coupled differential equations

$$\frac{\partial V}{\partial x} = -(R + i\omega L)I \tag{2.2a}$$

$$\frac{\partial I}{\partial x} = -(G + i\omega C)V. \tag{2.2b}$$

Algebraic transformations of the latter yield the telegrapher's equations [Sar43]

$$\frac{\partial^2 V}{\partial x^2} = \gamma^2 V \tag{2.3a}$$

$$\frac{\partial^2 I}{\partial x^2} = \gamma^2 I \tag{2.3b}$$

with

$$\gamma = \sqrt{(R + i\omega L)(G + i\omega C)}. \tag{2.4}$$

Note that V and I have a sinusoidal time dependence, which we have removed from our considerations by taking partial derivatives with respect to the spatial variable x. For simplicity, we

replaced $\tilde{V}$ and $\tilde{I}$ by V and I, respectively.
The general solution of the second order differential equations (2.3) is given by linear combinations of exponential functions

$$V(x) = A\, e^{-\gamma x} + B\, e^{\gamma x} \tag{2.5a}$$

$$I(x) = C\, e^{-\gamma x} + D\, e^{\gamma x}, \tag{2.5b}$$

where A, B, C, D denote complex amplitudes, i.e. integration constants from the mathematical point of view. In physical terms, equations (2.5) express a linear combination of travelling plane waves in opposite directions. Then

$$\gamma = \alpha + ik \tag{2.6}$$

is the complex *propagation constant* of each wave with the dimension m^{-1}, consisting of the *attenuation constant* α and the *wave number* or *phase constant*[1] $k = 2\pi/\lambda$. This entity describes the phase rotation of the wave per unit length. It is measured by rad/m, i.e. by m^{-1} and is related to the *phase velocity* by

$$v_{ph} = \frac{\omega}{k}. \tag{2.7}$$

Transforming Eq. (2.2), we obtain a relationship for the coefficients of $V(x)$ and $I(x)$ [DS06]:

$$Z_0 = \frac{A}{C} = -\frac{B}{D} = \sqrt{\frac{R + i\omega L}{G + i\omega C}}. \tag{2.8}$$

Z_0 is the *characteristic impedance* of the line. It is the high-frequency counterpart to the electrical resistance linking a static

1 Strictly speaking, the *phase constant* refers to *transmission lines* and the *wave number* to *plane waves*. In coaxial cables and strip lines both quantities are equal, since both media support transverse electromagnetic (TEM) waves. This is also the case in our waveguides. On the contrary, in non-TEM media like hollow metallic waveguides, both quantities may differ. β is often used as an alternative notation to k.

voltage to a stationary current. It encompasses all parameters describing the circuit. For low frequency ($\omega \to 0$; DC case) we obtain $Z_0 \to \sqrt{R/G}$. As a complex entity, Z_0 may be written in the form

$$Z_0 = R' + iX, \tag{2.9}$$

with R', $X \in \mathbb{R}$. Here R' denotes $\mathrm{Re}(Z_0)$ and is not to be confused with the series resistance R. X is the reactance.
It is important to note that the voltage and the current are well-defined only when dealing with environments that support TEM transmission. In more general cases, Z_0 relates the electric to the magnetic field [Gie05]. The fields are the defining values of the system, i.e. of Z_0, which have to be analyzed for a complete description. Consequently, it is instructive to consider the propagation of *electromagnetic waves* in high frequency transmission lines instead of oscillating currents and voltages.

Low-loss lines

In low-loss lines R and G are small compared to ωL and ωC, respectively. We then obtain by Taylor expansion [DS06]

$$\alpha = \alpha_R + \alpha_G \approx \frac{R}{2}\sqrt{\frac{C}{L}} + \frac{G}{2}\sqrt{\frac{L}{C}} \tag{2.10}$$

and

$$k \approx \omega\sqrt{LC}. \tag{2.11}$$

We discuss the dielectric losses in more detail following Ref. [Heu05]. These are defined by the *loss tangent* $\tan\delta$, which is the parameter of a dielectric material that quantifies its inherent dissipation of electromagnetic energy:

$$\tan\delta = \frac{\epsilon''}{\epsilon'} \tag{2.12}$$

with the complex permittivity $\epsilon = \epsilon' - i\epsilon''$, where $\epsilon' = \epsilon_0 \epsilon_r(\omega)$. The shunt conductance G is then given by

$$G = \omega C \tan\delta \tag{2.13}$$

and the contribution of the dielectric loss α_G for every TEM waveguide reads

$$\alpha_G = \frac{\pi}{\lambda} \tan\delta. \tag{2.14}$$

The dielectric loss depends on the wavelength λ and the loss tangent of the material.
Using the approximation $\tan\delta \approx \delta$ for dielectrics with small loss, we obtain [RWV94]

$$P(x) = P_0 \, e^{-\delta k x} = P_0 \, e^{-\frac{2\pi\delta f}{v_{ph}} x} \tag{2.15}$$

for the electrical power decay along the transmission line, with the source power P_0 and the frequency $f = \omega/2\pi$.
If the cable loss consists mainly of longitudinal losses, i.e. losses in the conductor instead of transverse ones (dielectric losses), the term containing G in (2.10) can be neglected. In this case, the loss can be reduced by increasing the series inductance of the line.
We return to the more general case of low loss lines, where R and G are present and apply the same approximations as for α and k to the impedance [Heu05]. Equation (2.8) is rewritten in the form

$$Z_0 = \sqrt{\frac{L}{C}} \sqrt{\left(1 - i\frac{R}{\omega L}\right) \cdot \left(1 + i\frac{G}{\omega C}\right)^{-1}}. \tag{2.16}$$

In the case of low loss lines this is approximated by

$$Z_0 \approx \sqrt{\frac{L}{C}}. \tag{2.17}$$

The approximation is based on the assumption that R and G are much smaller than ωL and ωC, which contain the energy of the system. Expression (2.17) is the impedance which is referred to when $50\,\Omega$ matching is sought for. This is also the *exact* impedance expression for the loss-free case ($R, G, \alpha = 0$), as can be seen in Eq. (2.8). Interestingly, also Eq. (2.11) becomes an *exact* expression in this case.
For low-loss cables with $\mu_r = 1$, expression (2.11) yields

$$v_{ph} = \frac{\omega}{k} = \frac{c_0}{\sqrt{\epsilon_r}} \approx \frac{1}{\sqrt{LC}} \tag{2.18}$$

with the speed of light in vacuum $c_0 = 1/\sqrt{\mu_0 \epsilon_0}$. The lack of a frequency dependence in the last term of Eq. (2.18) implies that the transmission is dispersion-free, the phase velocity equals the group velocity and the signals are not distorted.
Inserting Eq. (2.18) into (2.17) and eliminating L yields [Heu05]

$$Z_0 \approx \frac{\sqrt{\epsilon_r}}{c_0\, C}. \tag{2.19}$$

Using the above expression for c_0, we define the *impedance of free space*[2]

$$Z_{free} = \sqrt{\frac{\mu_0}{\epsilon_0}} = 120\,\pi\,\Omega \tag{2.20}$$

and obtain

$$Z_0 \approx 120\,\pi\,\frac{\sqrt{\epsilon_r}}{C}\epsilon_0\,\Omega. \tag{2.21}$$

Note that Eqs. (2.18), (2.19) and (2.21) are exact expressions for the loss-free case.
Whether R and G are exactly zero or treated as small compared to ωL and ωC defines the difference between a pure and a quasi TEM mode, respectively. The impedance is similar in both cases.

2 This is a physical constant relating the magnitudes of the electric and magnetic fields of electromagnetic radiation travelling through free space.

However, the attenuation constant α assumes totally different values in the two cases. Thus, the wave propagation, defined by the parameter $\gamma = \alpha + k$ is significantly influenced by small losses.
In addition, Eqs. (2.19) [and (2.21)] imply that the calculation of Z_0 in a homogeneous TEM or quasi-TEM transmission line can be performed after a *capacitance* calculation. The quasi-static approach that will be presented in Section 3.1 is based on this fact. Note that for waveguides with inhomogeneous dielectric, e.g. coplanar waveguides or microstrip lines, ϵ_r has to be replaced by an effective dielectric constant ϵ_{eff}, which is frequency and geometry dependent [Heu05].

2.1.2 Skin effect

The skin effect describes the distribution of a time-varying electrical current $\mathbf{j}$ inside a nonmagnetic electrical conductor with *finite* electrical conductivity σ. The periodic change of the current leads to a time-varying magnetic field $\mathbf{B}(t)$. According to Faraday's law of induction, $\mathbf{B}(t)$ generates an electric field $\mathbf{E}$ which opposes the change in current intensity and its corresponding magnetic field variation (Lenz's law)

$$-\frac{d\mathbf{B}}{dt} = \nabla \times \mathbf{E}. \tag{2.22}$$

$\mathbf{E}$ gives rise to *eddy currents* $\mathbf{j}_e$ inside the conductive material. As a result, an ideal, i.e. loss-free electrical conductor is free of inner fields. In materials with finite electrical conductivity σ, the amplitude of the time dependent electrical current density j decreases exponentially from its surface towards the inner part of the conductor [DS06]. This phenomenon is called *skin effect*

and the depth for which j decreases by a factor of $1/e$ is called the *skin depth* δ. The latter is given by

$$\delta = \sqrt{\frac{2}{\omega\sigma\mu_r\mu_0}} \tag{2.23}$$

with the electrical conductivity $\sigma = \rho^{-1}$, the relative permeability $\mu_r = 1 + \chi$ (χ is the magnetic susceptibility) and the vacuum permeability μ_0. As an example, the resistivity of gold $\rho^{Au} = 2.21 \cdot 10^{-8}\,\Omega m$ yields $\delta^{Au} = 1.15\,\mu m$ at 26.5 GHz considering ($\mu_r^{Au} = 1$). In general, at ferromagnetic resonance μ_r may increase up to several hundreds leading to a decrease of δ down to tens of nanometers.
The skin effect increases the electrical resistance due to confinement of the current near the conductor's surface. The roughness of metallic surfaces can thus have a large influence on the surface resistance [Heu05]. The skin effect introduces dispersive, i.e. frequency-dependent behavior of Z_0 and may also give rise to parasitic effects such as field distortion, impacting on the characteristic impedance Z_0 of e.g. coplanar waveguides.

2.1.3 Scattering parameters

As mentioned in Section 2.1.1, the travelling electromagnetic wave model is preferable over the oscillating voltage and current model when dealing with high frequency circuits. Correspondingly, the description of normalized incident a_i and reflected b_i waves has been introduced [Heu05]. An overview is given in Fig. 2.2 for a two-port device under test (DUT). The

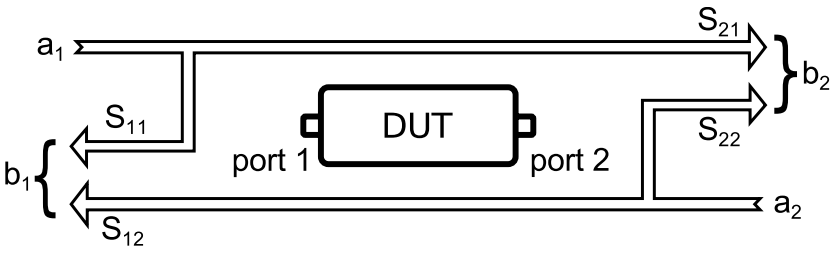

Figure 2.2: Illustration of S-parameters and normalized waves a_i, b_i being reflected by and travelling through a two-port DUT, respectively.

incident and outgoing waves are related by scattering parameters S_{ij} $(i, j = 1, 2)$

$$b_1 = S_{11}\, a_1 + S_{12}\, a_2, \tag{2.24a}$$

$$b_1 = S_{21}\, a_1 + S_{22}\, a_2. \tag{2.24b}$$

The meaning of the different S-parameters is summarized in the following:

$S_{11} = \frac{b_1}{a_1}\big|_{a_2=0}$ reflection parameter at port 1 under impedance-matched port 2

$S_{12} = \frac{b_1}{a_2}\big|_{a_1=0}$ transmission parameter at port 1 under impedance-matched port 1

$S_{21} = \frac{b_2}{a_1}\big|_{a_2=0}$ transmission parameter at port 2 under impedance-matched port 2

$S_{22} = \frac{b_2}{a_2}\big|_{a_1=0}$ reflection parameter at port 2 under impedance-matched port 1

S-parameters are complex values, which can be measured phase-sensitively by a vector network analyzer. Usually logar-

ithmic scaling is used and the conversion from the linear magnitude $|S_{ij}|$ to the logarithmic representation $|S_{ij}|(\mathrm{dB})$ reads

$$|S_{ij}|(\mathrm{dB}) = 10\log_{10}|S_{ij}|^2\,\mathrm{dB} = 20\log_{10}|S_{ij}|\,\mathrm{dB}. \tag{2.25}$$

The following holds for the input electrical power P_{a_2} and the power P_{b_1} measured at port 1:

$$P_{b_1} = |S_{12}|^2\,P_{a_2}. \tag{2.26}$$

P is often normalized to 1 mW and expressed in dBm

$$P(\mathrm{dBm}) = 10\log_{10}\frac{P}{1\mathrm{mW}}\,\mathrm{dBm}, \tag{2.27}$$

allowing easy calculation of e.g. the transmitted power at port 1

$$P_{b_1}(\mathrm{dBm}) = |S_{12}|(\mathrm{dB}) + P_{a_2}(\mathrm{dBm}), \tag{2.28}$$

with $|S_{12}|(\mathrm{dB}) \leqslant 0$ in passive devices.
As a rule of thumb, reflection parameter values $|S_{ii}| < -15\,\mathrm{dB}$ should be sought for during component design in order to minimize power reflection to a few percent (see Table 2.1).

S_{ii}(dB)	$\lvert S_{ii}\rvert$	reflected power
0	1	100%
-3	0.708	50%
-6	0.501	25%
-10	0.316	10%
-20	0.1	1%

Table 2.1: Logarithmic values of S_{ii} compared to linear magnitude values and corresponding reflected electrical power at the DUT.

2.2 Measurement principle

The measurement principle of vector network analyzer-based spin wave spectroscopy (VNA-SWS) [Kalo6] is illustrated in Fig. 2.3. The sample and coplanar waveguide (CPW) are ex-

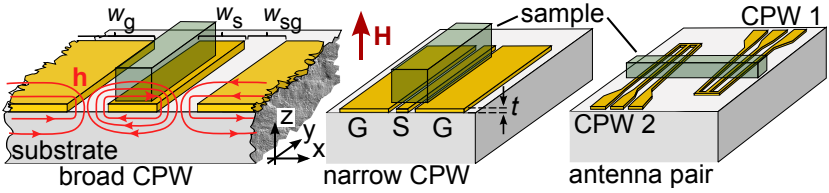

Figure 2.3: Sample-mounted CPWs with signal (S) line width $w_s = 1\,\text{mm}$, $20\,\mu\text{m}$, and $3\,\mu\text{m}$ (not to scale). The static field $\mathbf{H}$ is applied perpendicular to the CPW plane and the rf field $\mathbf{h}$ circulates around the conduction lines.

posed to an external, static magnetic field $\mathbf{H}$. In our setup, the latter is provided by a superconducting magnet. An electromagnetic wave produced by a vector network analyzer (VNA) travels in y-direction through the CPW and the sample, oscillating at radio-frequency (RF). While the *broad* and *narrow* CPW designs used in this work provide the TEM wave with an uninterrupted conductive pathway, the shorted antenna-CPW pair operates as an emitter/detector assembly.
The oscillating magnetic field $\mathbf{h}$ (red lines) contributes to the effective field $\mathbf{H}_{\text{eff}}$ and induces spin precession in the sample. This process is resonant and well-described by the frequency-dependent magnetic susceptibility (1.28), i.e. permeability $\mu(\omega)$ of the sample [Bilo7; Kalo6]. The resonant behavior of $\mu(\omega)$ alters the transmission characteristics of the electromagnetic wave, i.e. the propagation constant $\gamma(\omega)$ defined in Section 2.1.1 by modifying the inductance L of the high-frequency circuit. This

introduces a resonant behavior into the impedance and the S-parameters [Bar86] as well, which is detected by the VNA. Equivalently, the interaction between the sample and the CPW can be described in terms of a voltage V_{ind}, that is induced by the precession of the magnetization, which in turn causes a change of the magnetic flux in the CPW. This approach is outlined in Ref. [Gie05], where analytical expressions for V_{ind} are derived based on the type of excitation.
The exact relation between the S-parameters and the dynamic susceptibilty is complicated. In a first approximation, we use a 2-port evaluation scheme neglecting reflections in this work. This yields the uncalibrated complex effective microwave susceptibility [Bil07; Kal06]

$$\chi_{eff}(f) = i\left(\frac{\ln\left[S_{12}^{meas}(f)\right]}{\ln\left[S_{12}^{ref}(f)\right]} - 1\right), \tag{2.29}$$

where $\ln\left[S_{12}^{meas}(f)\right]$ and $\ln\left[S_{12}^{ref}(f)\right]$ are the natural logarithms of the complex S-parameters measured at the magnetic field of interest and at a reference field, respectively (see Section 2.3.1). Reference [Bil07] gives an overview of additional methods available to extract the frequency-dependent electric and magnetic permeability of the specimen starting from S-parameter data. While these methods yield different degrees of accuracy, it is shown that the resulting resonance positions and linewidths may disagree up to 1% and 10% relative error, respectively. We note that in this work we evaluate the resonance linewidth extracted from the magnitude of the S-parameters at high fields, where this error decreases drastically [Bil07]. At low fields, we use instead a time-resolved inductive measurement technique, presented in Section 2.4.

2.2.1 CPW Field distribution

The dimensions of the CPWs used in this work are summarized in table 2.2.

CPW	material	w_s	w_{sg}	w_g	t	L
broad	Cu/AlO_x	1000	330	5000	50	2500
narrow	Au/Cr/GaAs	20	12.4	295	0.12	9000
antenna	Au/Cr/GaAs	3	3	3	0.12	400

Table 2.2: Dimensions (in μm) of the CPWs used in this work: signal line width (w_s), distance between signal and ground line (w_{sg}), ground line width (w_g), metallization thickness (t), length (L).

Broad CPW

The broad CPW is commercially available[3] with a signal line width of 1 mm. It is a *conductor backed* CPW, i. e. the backside of the substrate is metallized in order to minimize spurious electromagnetic modes [Sim01]. Metallized via holes provide electrical contact between the ground lines, the backside and the electrical ground of our experimental apparatus described in Section 2.3. For a detailed and accurate insight into the field distribution of our CPWs, we performed finite-element (FEM) simulations[4].

3 CS-18, Southwest Microwave, Inc.

4 We used the software *CST Microwave Studio 2014* from CST Computer Simulation Technology, www.cst.com.

For all the simulations presented in this section, we have considered an incident microwave (MW) power of 1 mW and 50 Ω impedance to estimate the field amplitude in mT. The results for the broad CPW are presented in Fig.[5] 2.4. The left panels

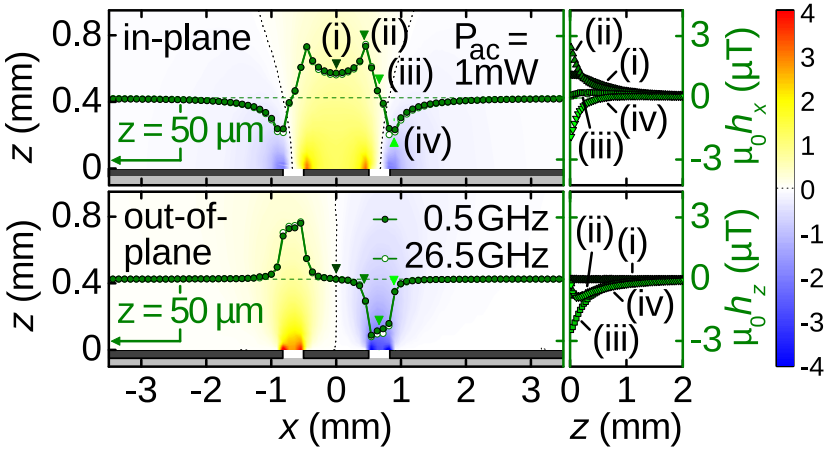

Figure 2.4: Near-field distribution of the broad CPW. The in-plane and out-of-plane components $h_x(x)$ and $h_z(x)$ are shown in the top and bottom panels, respectively, as a function of x. The color-coded field distribution shows a dominat in-plane field above the signal line and an out-of-plane field in the gap between signal and ground line. The line plot shows the spatial distribution of the field at a height of 50 µm above the CPW. The panels on the right-hand side show the dependence of the field component on the height above the CPW. The data were calculated at $f = 0.5$ GHz.

show the color-coded field strength for the in-plane (top) and out-of-plane (bottom) component of the dynamic field **h**. We find a dominant in-plane component h_x above the signal line

5 We thank A. Bauer and M. Kleinhans for assistance in the compilation of the figures in this section.

and a pronounced out-of-plane component h_z above the gaps between the signal (S) and ground (G) lines. At the edges of the metallic leads, the field amplitudes are enhanced due to the finite penetration depth of the RF current (skin effect; see Section 2.1.2).

The green and white circles illustrate $h_x(x)$ and $h_z(x)$ at the fixed height of $z = 50\,\mu m$ for 0.5 GHz and 26.5 GHz, both exhibiting a maximum strength of about $3\,\mu T$. The remarkably good overlap among these two frequencies suggests that the field distribution remains frequency-independent in the range $0.5 - 26.5\,GHz$.

Panels on the right-hand side of Fig. 2.4 show the height dependence of the field amplitude for different positions on the CPW marked by roman numerals on the color-coded plot. A significant field decay with increasing z is observed.

Note that for the broad CPW, the metallized bottom ground surface as well as the via holes were not considered in our simulations, since they were not expected to alter considerably the strong magnetic field components close to the signal line [Simo1] due to the low density of backflowing currents.

In Fig. 2.5 we show the far-field distribution up to several millimeters around the CPW. We observe an overeall decrease in amplitude compared to the near-field. The field enhancement at the lead edges disappears for $z \geqslant 0.5\,mm$.

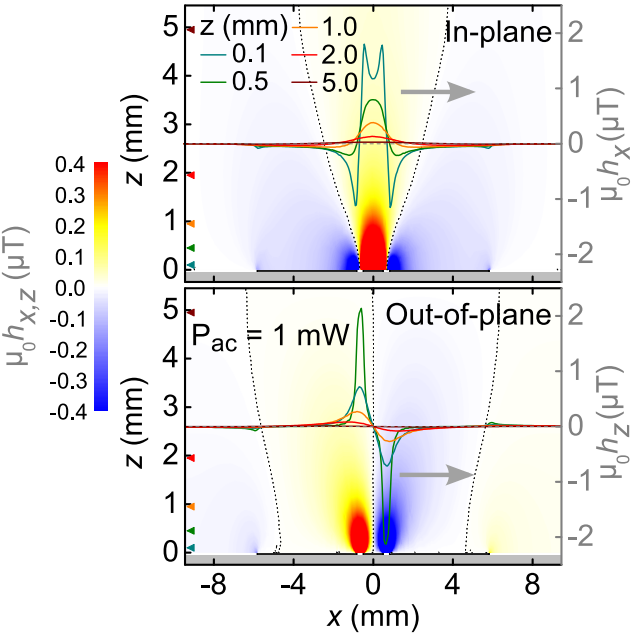

Figure 2.5: Far-field in- and out-of-plane amplitude profile of the broad CPW. Line plots show cuts at different heights above the CPW. Color-coded data correspond to $f = 0.5\,\mathrm{GHz}$.

Narrow CPW

The narrow CPW with a signal line width of $w_s = 20\,\mu m$ was micro-fabricated using optical lithography (see Section 2.6.1). We also model this structure by means of electromagnetic simulations and show the results in Fig. 2.6. The skin depth δ is comparable to the signal line width w_s, leading to a relatively homogeneous field distribution above the signal line and the absence of field spikes at the conductor edges (as in Fig. 2.4). The field intensity decreases approximately ten times faster with increasing z, compared to the broad CPW. In Section 2.2.2, we will draw a detailed comparison of the dynamic field homogeneity in our CPWs.

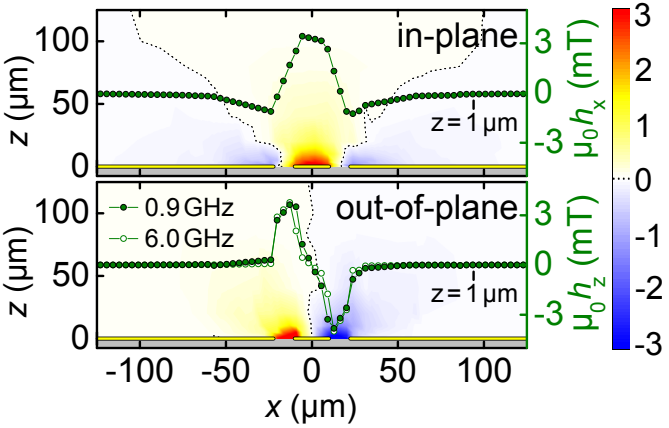

Figure 2.6: In- and out-of-plane field amplitude profile of the dynamic magnetic field **h** of the narrow CPW. The line plot shows the spatial distribution of the field at a height of 1 µm above the CPW. Color-coded data correspond to $f = 0.9\,GHz$.

Antenna-CPW

We now present the results for the antenna-CPW pair[6]. In Fig. 2.7 we compare the near- and far-field profile at two different frequencies for both the in- and the out-of-plane component. The typical dimensions of this assembly are comparable to the minimum mesh cell size (0.1 µm), which explains the discontinuities along z observed in the color-plot. Color-coded data correspond to $f = 26.5\,\mathrm{GHz}$.
Strikingly, the intensity at $f = 2\,\mathrm{GHz}$ is approximately ten times higher compared to $f = 26.5\,\mathrm{GHz}$. While the origin of this enhancement is not entirely clear, it results from the interplay of the following effects: (i) The CPW length amounts to 400 µm, which corresponds to about a quarter of the MW wavelength at $f = 26.5\,\mathrm{GHz}$. Hence, no proper propagation of the wave is allowed in this CPW. The wave is reflected at the shorted end and at the transition to the taper leading to interference and, eventually, amplification. (ii) The skin depth is reduced with increasing frequency leading to a higher current density, i.e. magnetic field amplitude. (iii) The electrical power decay along a transmission line decreases exponentially with increasing frequency [see Eq. (2.15)].

6 We fabricated various CPW pairs with different separation distance. The simulation was performed for a pair with 5 µm separation distance.

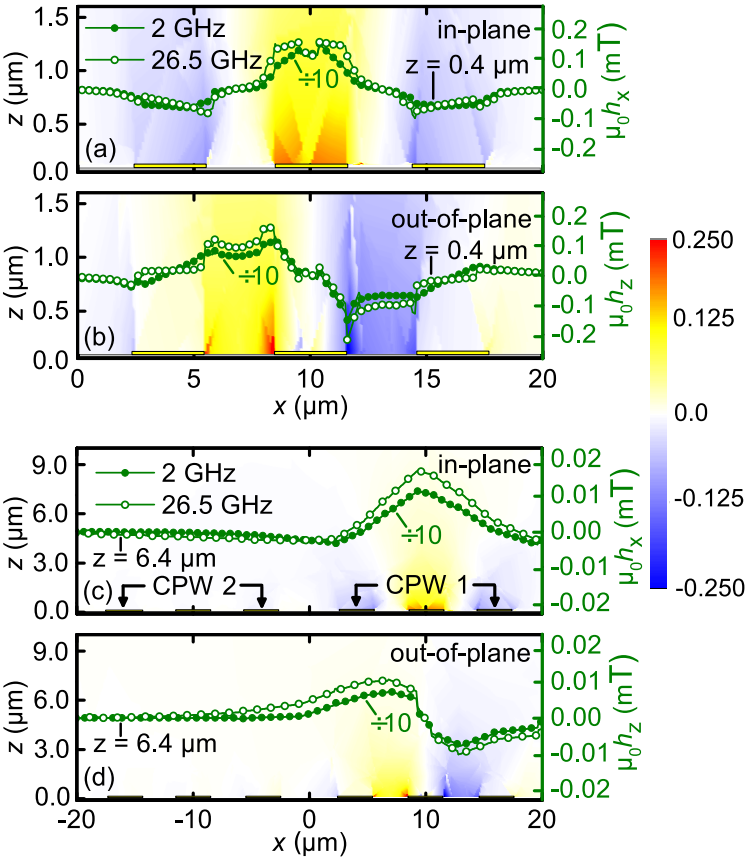

Figure 2.7: (a)-(b) Near- and (c)-(d) far-field field amplitude profile of the antenna-CPW with cuts at $z = 0.4\,\mu m$ and $z = 6.4\,\mu m$, respectively. The results for $f = 2\,GHz$ and $f = 26.5\,GHz$ are compared. Color-coded data correspond to $f = 26.5\,GHz$.

2.2.2 Excitation profile

Ferromagnetic resonance (FMR) is defined as the *uniform* and *coherent* precession of all spins in a material. This corresponds to an excited spin wave with infinite wavelength λ (wave vector $k = 2\pi/\lambda = 0$). The dynamic field distribution $\mathbf{h}(x, z)$ provided by the CPW gives rise to a distribution of finite k-vector values excited with different efficiency [VB10]. Assuming that the sample covers the entire width of CPW, the Fourier transforms of $h_x(x)$ and $h_z(x)$ give access to the k_x-distribution for the in- and out-of-plane excitation, respectively. Based on our simulation results shown in the previous section, we perfomed the Fourier transforms for the different CPWs used in this work and present our results in the following.

Broad CPW

We begin with the normalized wave vector distribution for the broad CPW in Fig. 2.8. We observe a qualitatively similar distribution of the Fourier transforms of $h_x(x)$ and $h_z(x)$. Several peaks are found, corresponding to the dominant spatial field modulation frequencies, characteristic to this CPW. Different colors indicate different heights z above the conducting leads. With increasing z, the peak heights reduce and Fourier components at large k_x vanish. This is expected for the transition between near- and far-field characteristics.

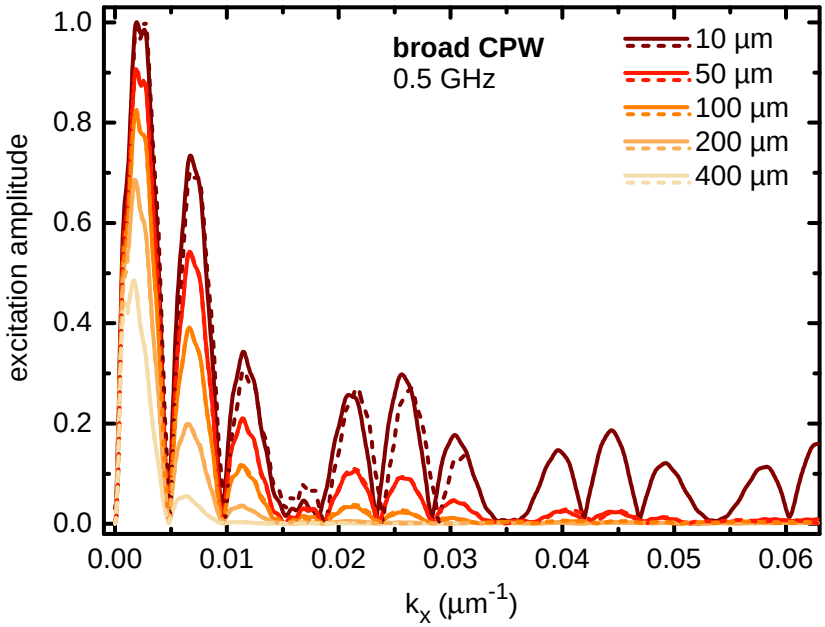

Figure 2.8: Wave vector distribution for the broad CPW at different heights z above the conducting leads. Solid and dashed lines show the in- and out-of-plane wave vector distribution, respectively.

Narrow CPW

The results for the near- and far-field distribution of the narrow CPW are shown in Fig. 2.9 (a) and (b), respectively. Compared to our results in Fig. 2.8, we observe differences between in- and out-of-plane component at large k_x in Fig. 2.9 (a). The largest peak shifts considerably with increasing z to smaller k_x. The relative shift is more pronounced than for the broad CPW. The narrow CPW produces approximately ten times larger wave vec-

tors k_x compared to the broad CPW, reaching up to $0.16\,\mu m^{-1}$ in Fig. 2.9 (b).

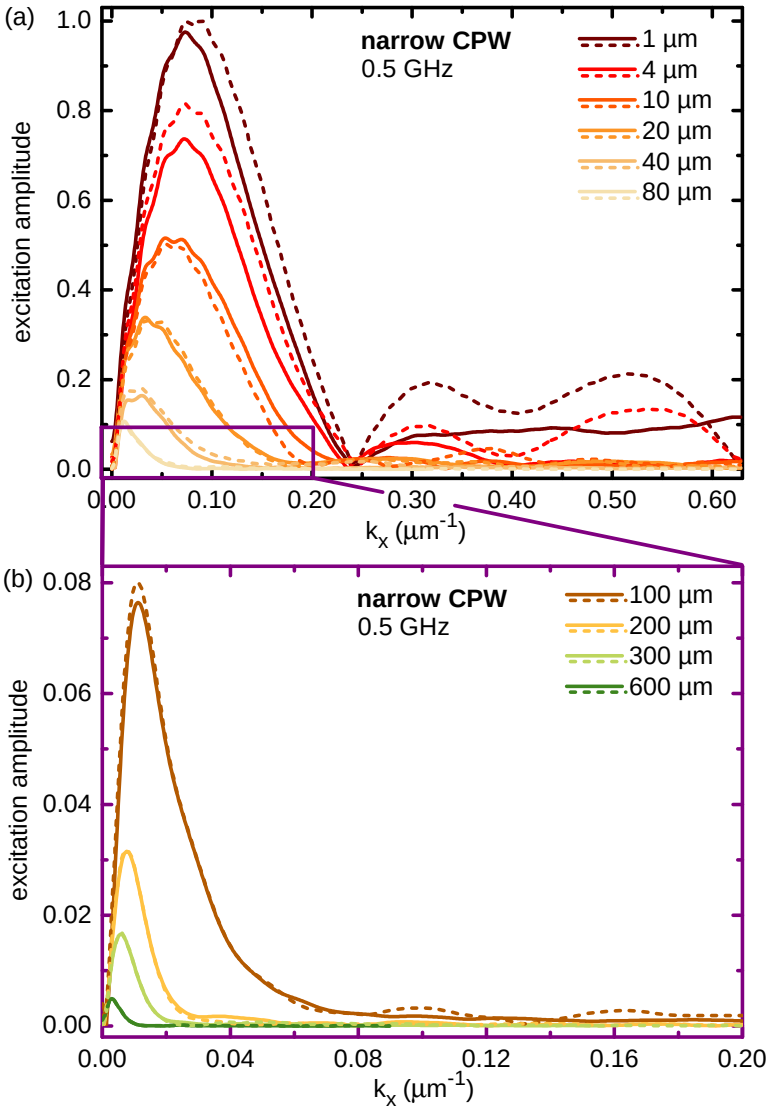

Figure 2.9: Near-(a) and far-field (b) wave vector distribution for the narrow CPW at different heights z above the conducting leads. Solid and dashed lines show the in- and out-of-plane wave vector distribution, respectively.

Antenna-CPW pair

Lithographically fabricated meander-shaped waveguides with small characteristic dimensions provide values up to $k = 8\,\mu m^{-1}$ [VB10]. In Fig. 2.10, we see that this is achieved in the

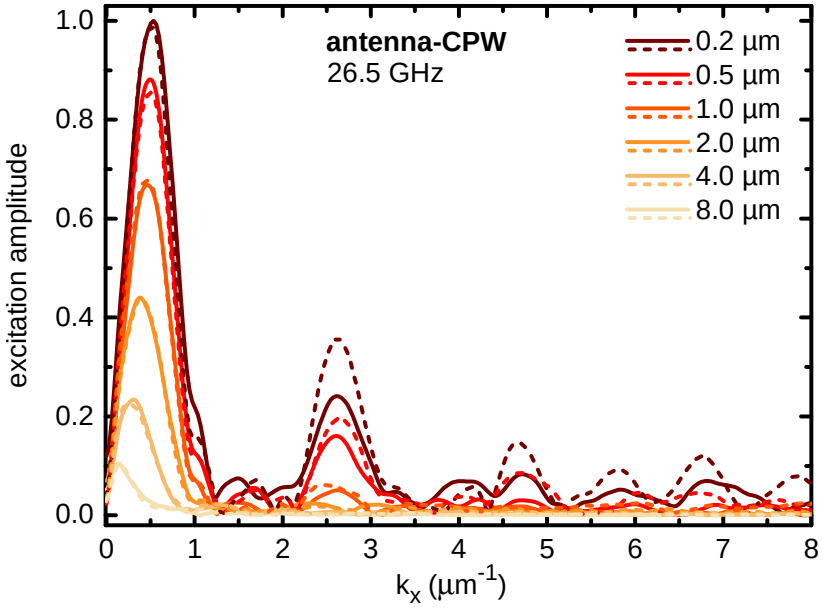

Figure 2.10: Wave vector distribution for the antenna-CPW at different heights z above the conducting leads. Solid and dashed lines show the in- and out-of-plane wave vector distribution, respectively.

proximity (within 200 nm) of the conductors of our antenna-CPW. The main excitation peak lies at an approximately five times higher k_x-value compared to the narrow CPW. Also, the difference among the in- and out-of-plane components is more

pronounced and the transition to the far-field profile takes place at lower values for z.

2.3 He-flow cryostat

Fig. 2.11 shows the cryostat used for temperature-dependent spin-wave spectroscopy. It consists of the following elements: a

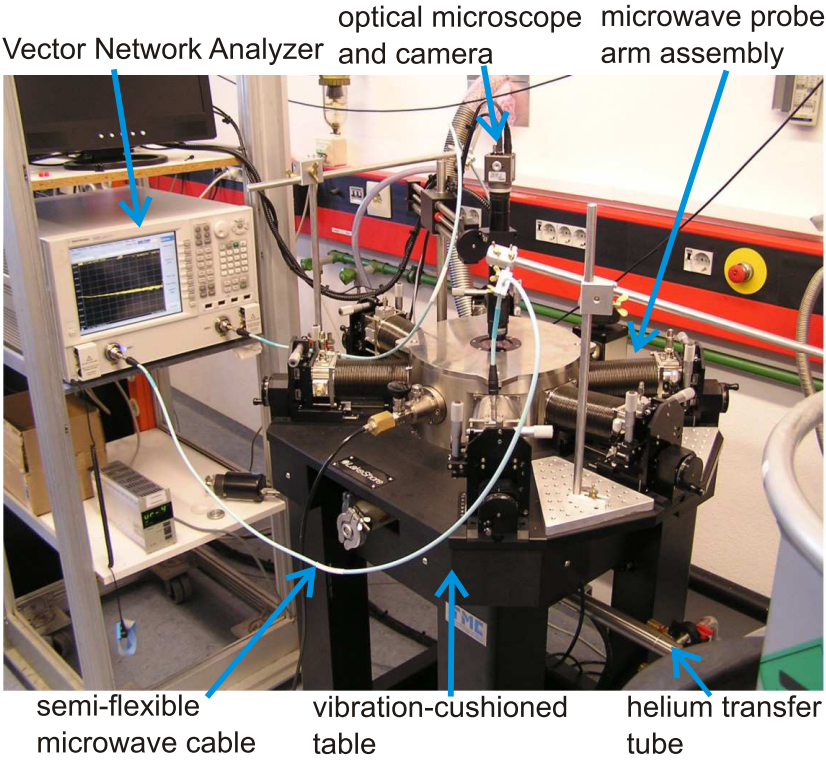

Figure 2.11: The LHe-flow cryostat for high frequency spin-wave spectroscopy measurements at variable temperatures with perpendicular magnetic fields.

commercially available helium flow cryostat with an integrated microwave probe system (model CPX-VF of *Lakeshore*) and a superconducting magnet, a vector network analyzer (VNA) and a

computer system (not shown).
The vacuum chamber ($p \leqslant 10^{-4}$ mbar) hosts a superconductive coil providing an out-of-plane magnetic field up to $\pm 2.5\,T$ and a microwave probe stage. The chamber is mounted on an air-cushioned table to reduce vibrations of the setup while measuring. Liquid helium flow bifurcation within the cryostat allows simultaneous and independent cooling of the sample stage and the magnet. An integrated heater near the sample position ensures automatic temperature control in the range 4.2 K - 400 K. Even when measuring the sample at room temperature, cooling the magnet below 5 K keeps the pressure in the chamber low allowing deactivation of the vacuum pumps (fore and turbo). This avoids mechanical noise.
Figure 2.12 (a) shows the inner part of the cryostat chamber. The superconducting magnet is installed below the ring-shaped brass cover. Rigid microwave cables connect microwave probe tips[7] (250 µm and 2 mm pitch for the narrow and broad CPW, respectively) to the semi-flexible microwave cables (see Fig. 2.11). Once the temperature is stabilized, the probe tips are manually placed on the CPW with the help of the optical microscope and micropositioning system. Then, fully automated measurements are performed. The tips are thermally anchored to the inner radiation shield of the cryostat via copper threads. When measuring at different temperatures varying by more than 5 K, the tips have to be lifted to avoid mechanical damage caused by temperature gradients.
The CPW is stabilized on a copper sample plate using a brass clamp. The sample is placed on top of the CPW and is fixed using a spring-loaded brass clamp. This provides us with an approximately constant mechanical force on the sample, regardles of the temperature set. Thermalization of the sample takes place mainly via the clamp due to its superior heat conductance com-

7 GGB Industries, Inc., U.S.A.

pared to the CPW substrate material (GaAs or alumina). The temperature is measured at the sample stage, below the copper plate.

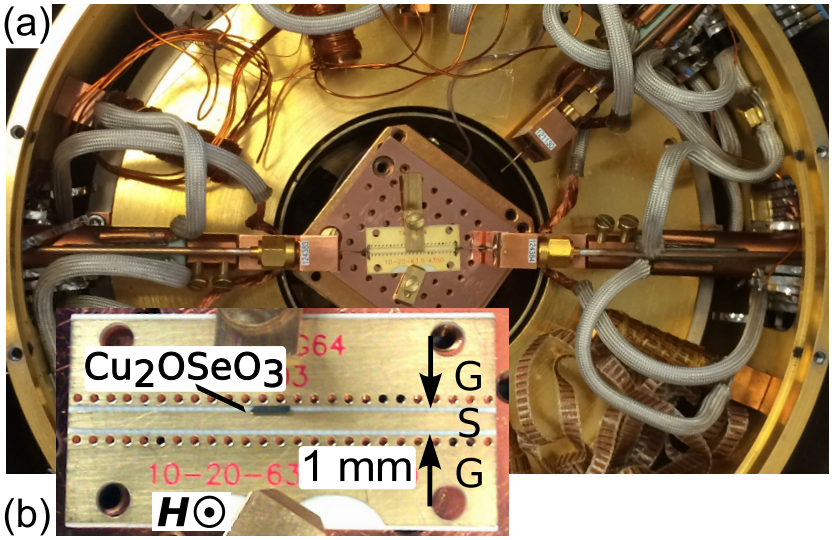

Figure 2.12: (a) Photograph inside the cryostat chamber. Microwave probe tips contact a broad CPW. (b) Magnified view of the broad CPW. The brass clamp holding the sample above the gap and providing thermal contact has been placed aside. A positive static magnetic field **H** points towards the observer.

2.3.1 Measurement procedure

A typical VNA-SWS measurement procedure reads as follows. The temperature was set and stabilized. At a sample temperature of 30K, the temperature stability was better than $\pm 5\,\mathrm{mK}$. Then, the microwave tips were contacted to the CPW. Proper contact was achieved via inspection of the transmission characteristics on the VNA. When contacting the probes at $\mu_0 H_{ext} \approx 1\mathrm{T}$, we obtained less parasitic resonances in our spectra. Remaining resonances originated from the setup and were produced by mechanical drifts during field sweeps. The measurement protocol loaded in a *LabView*[8] program was then carried out: a frequency scan from 100MHz to 26.5 GHz was performed at a fixed field value. All four S-parameters were measured in magnitude and phase. The field was then changed according to the predefined set of values and a new frequency scan was performed until the entire desired field range was scanned through. Field steps varied between 2 mT (high resolution scan) and 100 mT (rapid scan).
A frequency scan at a specific field ($\approx$ 1.0 T) is defined as the reference spectrum S_{ref}, which does not contain any resonances from the sample in the measured frequency range. We define the scans performed at different fields as S_{meas}. The modulus $|S_{ref}|$ is subtracted from $|S_{meas}|$ giving rise to $\Delta S = |S_{meas}| - |S_{ref}|$. This difference technique allows for the suppression of systematic errors from the setup, i.e. cable resonances or calibration errors. The method works best in the absence of temporal or field-induced system drifts.

8 *National Instruments* corp.

2.3.2 Calibration and signal-to-noise ratio

The cables and connectors between the ports of the VNA and the probe tips inside the probing station introduced impedance mismatch causing reflections, signal leakage or crosstalk. We reduced corresponding resonance features via the difference technique and calibration.
Calibration allowed for error correction down to the microwave probe tips. A variety of coplanar precision standards fabricated on alumina[9] were contacted with the microwave probe tips. The VNA then performed frequency scans and calculated the error terms, which were subtracted from further measurement data. In this thesis, the short-open-line-through (SOLT)[10] calibration procedure was used providing vector error correction.
The main factor influencing the signal-to-noise ratio (SNR) of reference-subtracted measurement data was the impedance mismatch along the signal pathway, rather than the calibration. Impedance deviation from the 50 Ω standard caused back-reflection of electromagnetic signals (see Section 2.1.3), which interfered with the magnetically-induced signal of the specimen. To minimize this effect, high-quality commercial components complying to industry standards were installed in our apparatus. The CPW-to-MW-tip contact and the transmission characteristics of the CPW remained the crucial aspects determining system performance. In the framework of this thesis, we optimized the design of CPWs to match with the impedance of the VNA (50 Ω) in order to further increase the electromagnetic

9 Models *CS-5* and *CS-18* from GGB Industries, Inc., U.S.A., for the narrow- and broad-pitch microwave (MW) tips, respectively.

10 SOLT stands for **S**hort, **O**pen, **L**oad and **T**hrough. It consists of four test pads, namely a short circuit between both tips, an open connection, a precision 50 Ω load and a 50 Ω-matched transmission line.

signal throughput by minimizing reflections. The optimization procedure is outlined in Chapter 3.

2.4 Pulsed induced microwave magnetometry

In this work, we have also performed pulsed induced microwave magnetometry (PIMM) [Sil99]. This method is complementary to VNA-SWS (see Section 2.2), as it probes the spin dynamics in the time instead of the frequency domain. In our case, PIMM is implemented by means of *time-domain-reflectometry* measurements, where a *Tektronix DSA 8200* digital serial analyzer (DSA) including two *Tektronix 80E08* electrical sampling modules is connected to the cryogenic probe station described in Section 2.3. Each module sends (detects) voltage pulses with 11.67 ps rise time[11] sent (received) through the microwave tips contacted to the CPW. This is reproduced schematically in Fig. 2.13. We use two different assemblies based on the broad CPW [Fig. 2.13 (a)] and antenna-CPW [Fig. 2.13 (b)] in order to vary the transferred wavevector distribution (see Section 2.2.2) to the sample. As will be discussed later in more detail, we compare measurements obtained from a parallel and perpendicular placement of the bar-shaped Cu_2OSeO_3 sample on the broad CPW.

Impedance mismatch at SMA connectors or MW tips gived rise to characteristic reflection patterns, as the pulse travelled from port 2 through the setup. By the characterization of the signal pathway at room temperature involving delibarate disconnection of mechanical components, we related the time position of these features to their position in space. Accordingly, we located the position of the magnetic specimen with respect to the running time of the microwave signal.

The MW pulse took 15 ps to travel along the specimen, when

11 Defined between 10% and 90% of the pulse height.

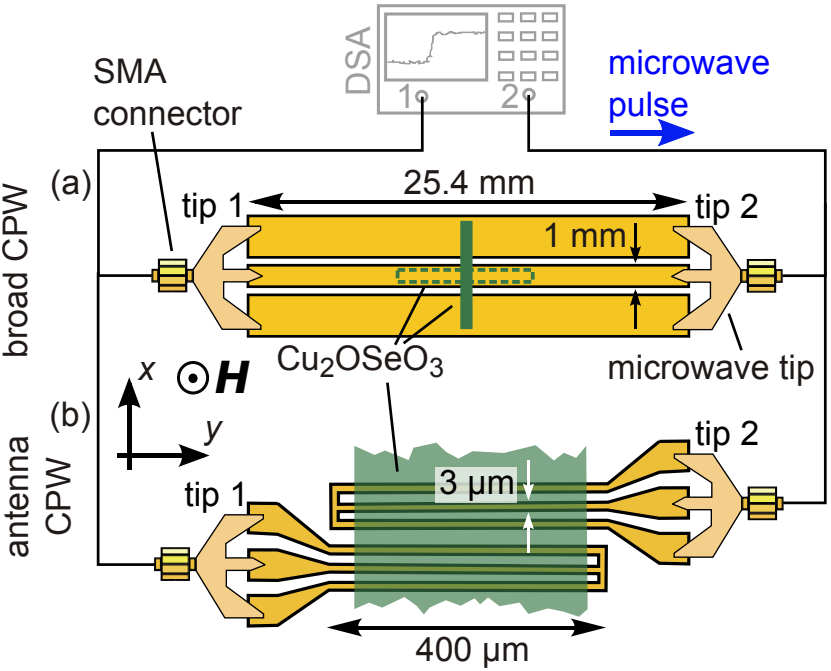

Figure 2.13: Schematic experimental setup for PIMM measurements. (a) The sample is placed perpendicular or parallel on the broad CPW. (b) The sample is placed perpendicular on the shorted antenna pair.

the latter was placed parallel to the CPW. The pulse took 130 ps to travel from one end of the CPW to the other. Hence, we consider an instantaneous excitation of the sample by the magnetic field **h** of the pulse. The spin precessional motion coupled inductively to the CPW and induced a characteristic ringing of the voltage signal $V(t)$ (t is the time). To extract the latter, being significantly lower than the voltage steps from high-frequency components, we subtracted a reference dataset recorded at high fields from all waveforms. The voltage V was recorded strobo-

scopically at a repetition rate of 44 kHz at either port (channel "CH") 1 or port 2. We will refer to the former and latter as time-domain transmission (TDT) and time-domain reflection (TDR) measurements, respectively.
In Fig. 2.14 we compare signals obtained by TDT and TDR measurements with Sample **A** (see Appendix A) placed parallel on the broad CPW. A clear beating pattern is resolved

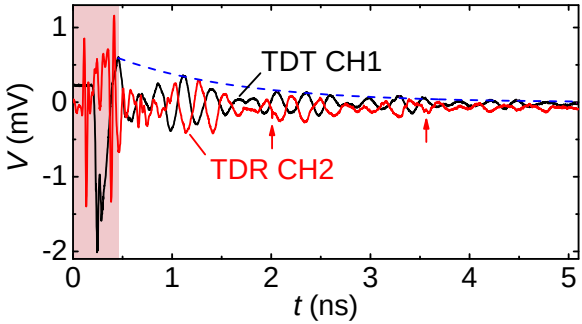

Figure 2.14: Comparison between TDR and TDT waveforms at 20 K; 70 mT measured with sample **A** on the broad CPW. The red-colored area marks the transient regime. The blue dashed line is an exponentially decaying guide to the eye.

for $t > 0.5$ ns and $t > 1$ ns in the TDT and TDR datasets, respectively. We observe several distortions in the TDR data (for $t < 1$ ns and at the positions marked by red arrows). For $t > 0.5$ ns, the maxima of the beating pattern in the TDT data are well-reproduced by an exponential guide to the eye (blue dashed line), in contrast to the prominent double-peak structure for $t < 0.5$ ns with significantly larger amplitude. We use this observation as the defining criterion for the transient regime (red region) in the TDT data. Due to the presence of distortions in the TDR data, we chose to concentrate on TDT data when using the broad CPW. In Section 5.4, we analyze the data in

more detail by fitting two exponentially decaying sine functions to our data. In this way, we extract the characteristic relaxation times τ of the underlying oscillations giving rise to the beating pattern and discuss their origin.
When using the antenna-CPW pair [Fig. 2.13 (b)], we did not resolve a signal of magnetic origin transmitted over the antennae (e.g. travelling spin wave). Hence, in this case we show TDR data. We note that when recording the reflection data at port 2, port 1 is not excited to avoid interference from the corresponding antenna[12].

We conclude with some additional technical remarks. The combined use of the two *Tektronix* 80*E*08 electrical sampling modules results in jitter values in the order of 1 ps [Koro4; Sil99]. To maximize the SNR by minimizing stochastic errors, we average over 4096 waveforms recorded under constant external magnetic field and temperature.
We found that the impedance of the broad CPW at room temperature and at 5 K is $(50 \pm 0.5)\,\Omega$, both with and without the sample installed. The output pulse height is 250 mV and corresponds to 1.25 mW transmitted power, assuming a $50\,\Omega$ line. The excitation power of the TDR sampling modules is thus comparable to the $0\,\text{dBm} = 1\,\text{mW}$ output power level of the VNA during VNA-SWS measurements.
We note that although PIMM is a highly accurate method for probing the time-response of a magnetic system, it is inferior to VNA-SWS in terms of SNR. This is due to the large bandwidth of the detector. We used a bandwidth setting of 20 GHz.

12 Port 1 is also automatically matched to $50\,\Omega$ by the DSA.

2.5 Variable temperature insert

In the framework of this thesis, we have developed a sample holder with GHz cables that allowed us to study spin-wave resonances in a 2D vector magnet.

2.5.1 Experimental apparatus

The setup (Fig. 2.15) consists of the following components: a liquid helium (LHe)-bath cryostat with a vector magnet and a variable temperature insert (VTI)[13]. Additionally, a VNA, temperature controller, 3-axis Gaussmeter, stepper motor driver and magnet power supply (not shown) are used. The VTI is composed of a double-walled, vacuum-isolated sample space, inside which the sample stick is inserted (Fig. 2.16). The sample space is connected with the LHe bath via a flow valve and capillary allowing LHe to flow through a vaporizer heater, around the sample stage and ultimately out of the pumping port. A 50 W heater installed in the vicinity of the sample in combination with an external controller provide temperature control in the range[14] $5 - 300\,\mathrm{K}$ with a stability of $\pm 5\,\mathrm{mK}$. The DC wiring (not shown) and two spirally formed nonmagnetic GHz cables are mounted inside the VTI forming the signal pathway down to the field center of the magnet. The spiral cable shape allows thermally-driven mechanical tensions to relax during cooldown.

13 Both components were purchased from American Magnetics International Inc., Oak Ridge, USA.

14 Lower temperatures can be achieved by introducing LHe into the sample space and lowering the pressure. This requires further optimization of the temperature control loop, going beyond the scope of this thesis.

The sample stage is shown in Fig. 2.17. The broad CPW introduced in Section 2.2 is contacted to nonmagnetic edge launch connectors[15] via soldering. The latter are connected to short MW cables attached at the end of the long cables coming from the top of the sample rod via female-female-connectors (not shown). To obtain a symmetrical signal pathway with respect to the CPW, the upper short MW cable is twisted to compensate for the lower placement of the bottom connector.
The sample is fixed on the CPW with thermally conductive, cryogenic adhesive[16]. The temperature is probed directly on the sample holder by a calibrated Cernox sensor. One axial and two transverse cryogenic Hall sensors are mounted near the sample and provide us with three-dimensional field readout. A fender mounted at the bottom acts as a safety net in case the sample is detached. It is perforated to allow He gas circulation.

15 Model 292-04Z-5, Southwest Microwave, Inc., Arizona, USA.
16 IMI 7031 Varnish, GVL Cryoengineering Dr. George V. Lecomte GmbH, Stolberg, Germany.

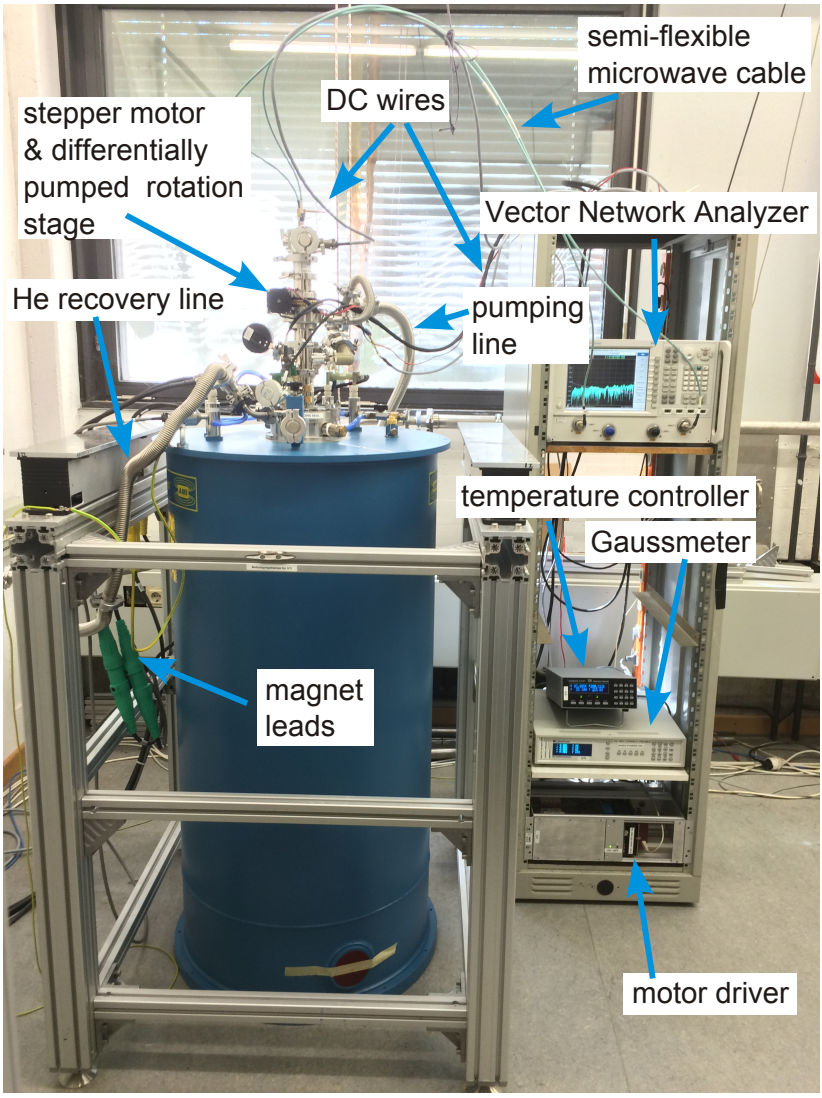

Figure 2.15: Photograph of the VTI installed in the cryostat containing the vector magnet. High stability, low loss semi-flex cables (cyan) connect the GHz lines in the VTI sample stick to the VNA. All measurement devices are controlled via GPIB interface.

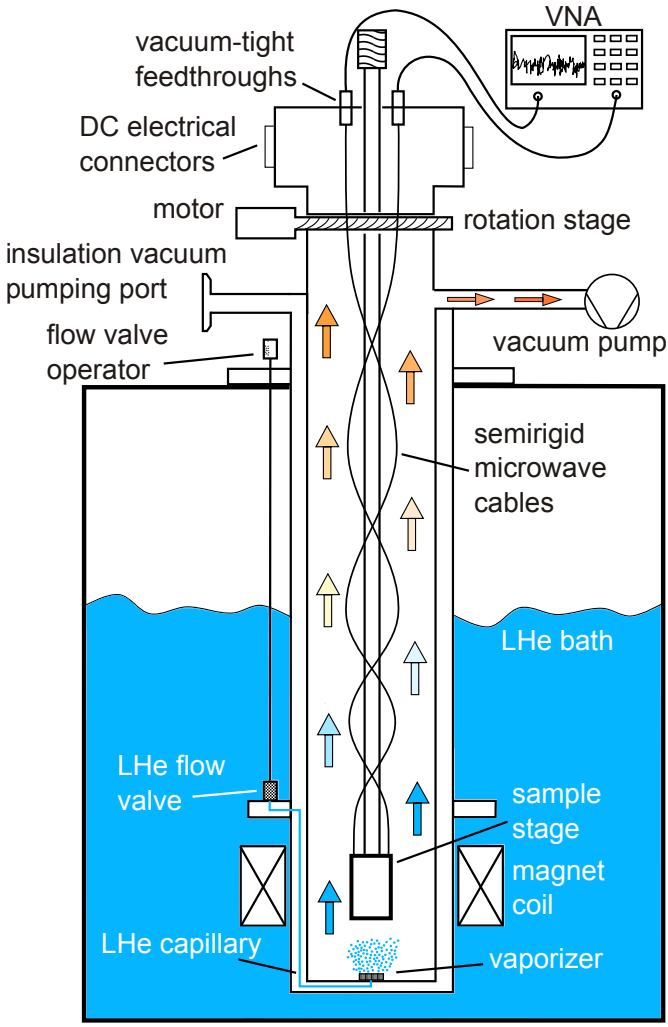

Figure 2.16: Schematic diagram of the apparatus. LHe is pumped into the sample space through a capillary. The He gas (arrows) flows from the vaporizer towards the vacuum pump thereby cooling the sample stage and cables.

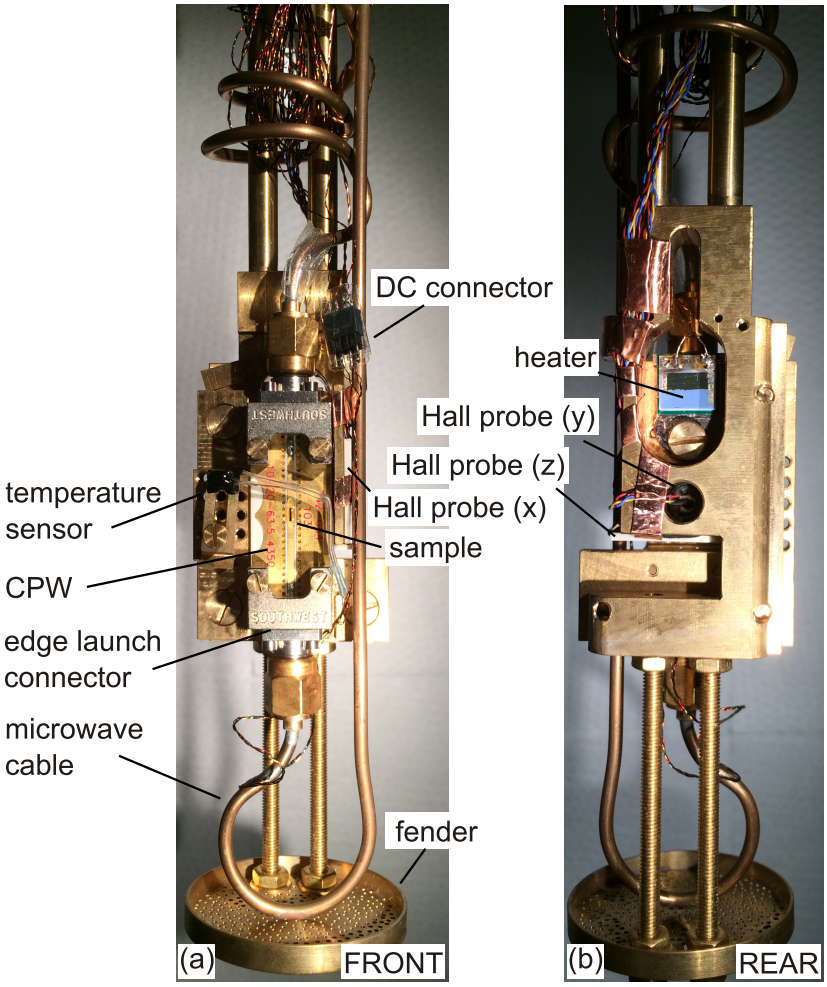

Figure 2.17: Front (a) and rear (b) view of the home-built VTI sample stage. The sample is mounted on the broad CPW, which is connected to the semi-rigid MW cables via edge launch connectors. A set of three Hall probes are mounted around the sample. All components are strictly non ferromagnetic.

2.5.2 3D field access

The vector magnet provides us with a field vector **H** at any angle ϕ within the yz plane [Fig. 2.18 (a)]. This is achieved by the superposition of a H_z and H_y field, provided by a single and a split coil, respectively. A maximum field magnitude of 4.5 T is accessible for rotation of the field vector in the yz plane. The en-

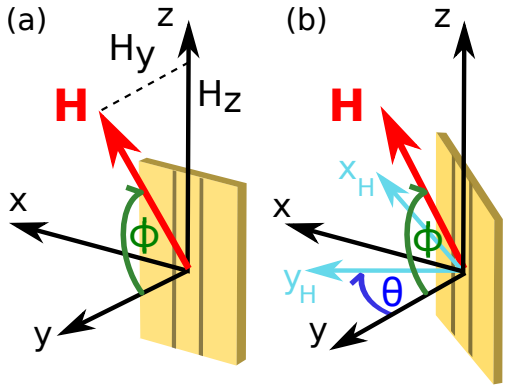

Figure 2.18: The angles defined for the measurements with the variable temperature insert. In (a) H_y lies perpendicular to the CPW plane. The field **H** rotates in the yz plane. The magnet (laboratory) and local coordinate system of the Hall probes overlap. (b) The CPW and its corresponding reference system (cyan) are rotated by θ around the z axis. **H** remains unchanged with respect to the laboratory's reference system yet points along a new direction with respect to the CPW.

tire sample rod is mounted on a differentially pumped rotation stage. A stepper motor rotates the latter around the z-axis by an angle θ [Fig. 2.18 (b)]. The gear ratio of the stage in combination with the step size of the motor yields a minimum angle step

of 0.03°. In this way, a magnetic field with a precisely defined orientation relative to the CPW is applied.

2.5.3 Angle calibration

After each sample installation, the CPW plane is aligned perpendicularly to the y-axis defined by the magnet. This is achieved by applying 1 T along $\phi = 0°$ (see Fig. 2.18) and rotating the sample rod with the motor. While doing this, the signal of the Hall probes is monitored to identify the angle θ_0, for which **H** points perpendicularly out of the CPW plane. This procedure is performed at constant temperature to minimize spurious offset signal generation in the Hall probes. To avoid mechanical hysteresis, θ_0 is approached from one side starting from the reference switch of the motor.
Since the long edge of the CPW is slightly tilted against the z axis, also ϕ_0 is determined in a similar way prior to the measurement. This takes place at θ_0 by tilting **H** in the yz-plane (variation of ϕ).

2.5.4 Measurement procedure

Similar to the procedure described in Section 2.3.1, we apply the difference technique. In this case, we have the choice to record the reference spectrum not only at a specific field magnitude but also at a specific angle. Recording the reference at a different angle θ, i.e. rotating the sample rod and twisting the semi-flex cables still provides data with a good SNR after the subtraction

method. Systematic errors from the setup are highly stable with respect to field variation and sample rotation and are successfully eliminated by the difference technique. Hence, no broadband frequency calibration was necessary.

2.6 Sample preparation

2.6.1 Preparation of coplanar waveguides

Here we describe the fabrication of optimized CPWs developed in this thesis (narrow CPW and antenna-CPW). We use a GaAs substrate and chromium/gold deposition. The conductor width and spacing vary between 3 μm and 20 μm, defined by state-of-the-art optical lithography. The process is schematically illustrated in Fig. 2.19. The substrate is cleaned in acetone and isopropanol and purged with nitrogen. It is then spincoated (4500 rpm, 60 s) with LOR 5A photoresist and hardbaked at 160 °C for 60 s [Fig. 2.19 (a)]. Then, the positive photoresist S1813 is applied (6000 rpm, 40 s) and hardbaked at 115 °C for 60 s. Exposure to ultraviolet light from a mercury arc lamp through a chromium mask follows during 3.5 s [Fig. 2.19 (b)]. The mask contained the specifically designed CPWs. The exposed photoresist is chemically altered [Fig. 2.19 (c)] and removed during development by the base MF26A for 25 s. The development time is sharply defined by rinsing with de-ionized water for 30 s. The isotropic development of the LOR photoresist together with the presence of the second resist S1813 ensures an undercut [Fig. 2.19 (d)] facilitating lift-off processing. Chromium and gold layers of 4.5 nm and 120 nm thickness, respectively, are deposited by electron beam evaporation [Fig. 2.19 (d)-(e)]. This process is performed in a high vacuum chamber (residual pressure $p \approx 10^{-7}$ mbar). Finally the bi-layer resist is lifted off by the microposit remover 1165 leaving the desired film on the substrate.
All steps except the film deposition by evaporation [Fig. 2.19 (d)]

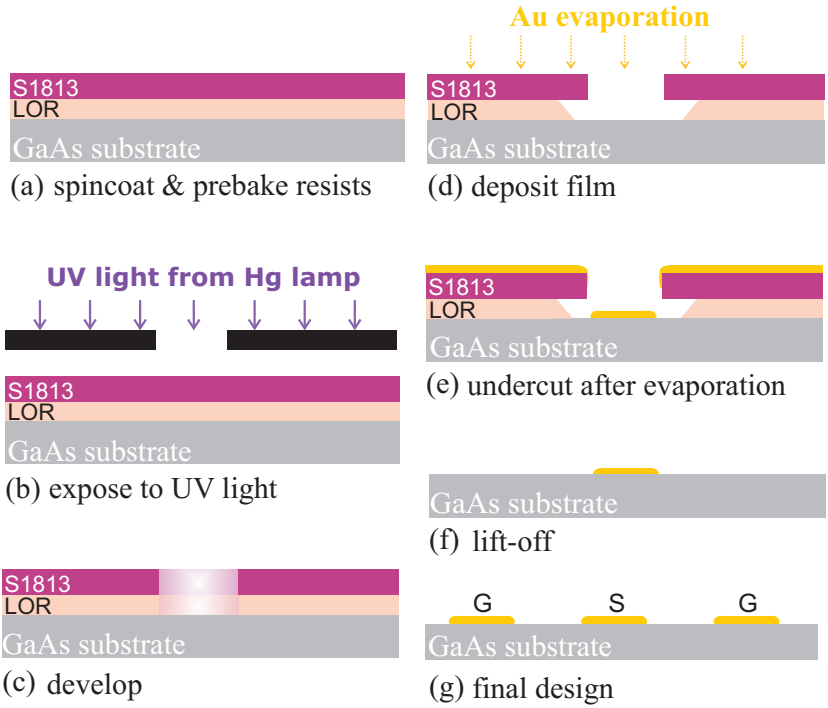

Figure 2.19: Optical lithography steps using a double layer resist. This creates an undercut in the resist double layer providing sharp edges and thus high yield in lift-off processing.

are performed in a cleanroom with stable environmental conditions (21°C, 40-60 % relative humidity). This prevents sample damage by e. g. dust particles and ensures the reproducibility of the recipe, since photoresists are sensitive to temperature and humidity variations.
During spin coating, the photoresist concentrates on the periphery of the substrate, creating thus elevated regions that impede uniform contact with the photomask during exposure. To overcome this, we carefully remove the outer rim of the resist

layer with the help of a sharp cotton stick dipped in 1165 prior to baking. We apply this method to both resist layers, yet only for the preparation of the antenna-CPWs, where this proves to increase the yield and quality of the sample.

2.6.2 Preparation of Cu_2OSeO_3 samples

In our measurements we use rod-shaped samples cut from different crystallites. Single crystals are grown[17] by vapor transport [Bel12; Gne10]. The crystallographic orientations of the crystallites is determined using Laue x-ray diffraction and rod-shaped samples are cut with a wire saw and carefully polished to size. The samples have a size of about $2.3 \times 0.4 \times 0.3\,\mathrm{mm}^3$. The side which is placed on the CPWs is polished with 4000 grit silicon carbide paper ($\approx 3\,\mu\mathrm{m}$ grain size). The exact dimensions and estimated demagnetization factors of our samples are listed in Appendix A.

17 The sample grower is H. Berger, EPFL Lausanne, Switzerland.

3 Optimization of coplanar waveguides

The impedances of the VNA and the microwave probe tips used in this work are set to the value of 50 Ω. For avoiding unwanted signal reflections, achieving high signal throughput and increasing the dynamic range of the setup it is key to realize the same impedance of 50 Ω in connected coplanar waveguides (CPWs). This way the SNR is enhanced, which allows for the resolution of e.g. resonances of weak higher order modes. In this chapter we discuss the optimization procedure of our CPWs relying on a combined analytical (quasi-static) and numerical approach based on finite-element electromagnetic simulations.

3.1 Quasi-static approach

3.1.1 Conformal mapping

In order to calculate the impedance of a CPW based on Eq. (2.19), the overal capacitance per unit length of the system C_{tot} is required. The latter is obtained using a conformal map, i.e. a mathematical function that preserves the angles of the elec-

tromagnetic fields locally and allows the equivalent solution of Maxwell's equations in the conformal image [GC87; GGB79; GGB96]. In this procedure, the half-plane $x > 0$ of the CPW [Fig. 3.1 (a)] is mapped to a parallel plate configuration filled with a material with dielectric constant ϵ_r [Fig. 3.1 (b)]. We consider an infinitely large ground plate width w_g. All conductor plates are assumed infinitely thin and loss-free.

An analytical expression containing elliptical integrals results for the capacitance of the dielectric-filled part of the CPW C_{diel} [GGB96]. The map is repeated for the air-filled region to yield C_{air}. C_{tot} is given by the sum of C_{diel} and C_{air}. The total effective value for the dielectric constant of the whole system $\epsilon_{eff} = (\epsilon_r + 1)/2$ is inserted along with C_{tot} into Eq. (2.19). The resulting expression [Gie05]

$$Z_0 = \frac{29.97\pi}{\sqrt{\epsilon_{eff}}} \cdot \frac{K\big(w_s/(w_s + 2w_{sg})\big)}{K'\big(w_s/(w_s + 2w_{sg})\big)} \tag{3.1}$$

for the characteristic impedance Z_0 is dependent only on the ratio w_s/w_{sg}. w_{sg} is the distance between signal and ground line defined in Fig. 2.3. The functions $K(k)$ and $K'(k) = K\big(\sqrt{1-k^2}\big)$ are the complete elliptic integrals of the first kind, and its complement, respectively. These are calculated with the help of a mathematical software such as *Mathematica*.

Note that a finite thickness t of the conducting plates shifts the wave propagation along z. This effect changes the effective dielectric constant and is considered by defining effective values of conductor width and spacing [GGB79]. Finally, the approach presented in this section holds only in the static case $\omega = 0$. However, due to small structure dimensions, the transverse electromagnetic wave shows little dispersion [GC87] and good agreement with real structures operating at RF is obtained via this method in first approximation.

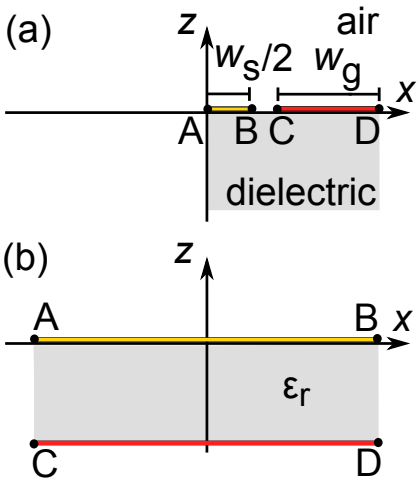

Figure 3.1: Conformal transformation planes for the capacitance calculation of a CPW. (a) CPW half plane including the ground plate (red) and half of the signal line (yellow), both assumed infinitely thin. (b) Conformal map of the CPW, where the conductor plates are parallel. The electromagnetic fields (not shown) are mapped along with the geometrical components.

3.1.2 CPW modes

We now extend the procedure outlined above to CPWs with finite ground plate width w_g and thickness t. Within the framework of the quasi-static analysis, the wave propagation along a field-coupled pair of transmission lines, e.g. the current leads of a CPW, is expressed in terms of two modes exhibiting odd or even symmetry about a perpendicular plane corresponding to a magnetic or electric wall, respectively [GGB79]. This is shown in Fig. 3.2. Each mode is characterized by a distinct impedance, Z_o

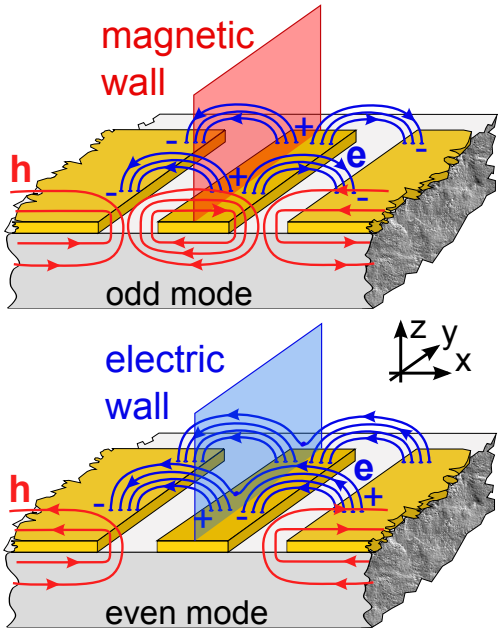

Figure 3.2: Odd (top) and even (bottom) mode field configurations of a CPW. The oscillating magnetic **h** and electric **e** field has only a normal component at the magnetic and electric wall, respectively. After [GGB79].

and Z_e, respectively. The corresponding analytical expressions read [GC87]

$$Z_e = \frac{30\pi}{\sqrt{\epsilon_{\text{eff},e}}} \frac{K(k_2')}{K(k_2)} \tag{3.2}$$

$$Z_o = \frac{120\pi}{\sqrt{\epsilon_{\text{eff},o}}} \frac{K(k_4')}{K(k_4)}, \tag{3.3}$$

where the different effective dielectric susceptibilities are given by

$$\epsilon_{\text{eff,e}} = 1 + (\epsilon_r - 1)\,\frac{K(k_3)K(k_2')}{2K(k_3')K(k_2)} \tag{3.4}$$

$$\epsilon_{\text{eff,o}} = \frac{\epsilon_r + 1}{2}, \tag{3.5}$$

with

$$k_2(a,b,c) = \frac{a}{b}\sqrt{1-\frac{b^2}{c^2}}\sqrt{1-\frac{a^2}{c^2}}^{-1} \tag{3.6}$$

$$k_3(a,b,c) = k_1(a,b)\sqrt{\frac{1-k_{1b}^2}{1-k_{1a}^2}} \tag{3.7}$$

$$k_1(a,b) = \sinh\Big(\frac{\pi\cdot a}{2h}\Big)\Big/\sinh\Big(\frac{\pi\cdot b}{2h}\Big) \tag{3.8}$$

$$k_{1a}(a,b,c) = \sinh\Big(\frac{\pi\cdot a}{2h}\Big)\Big/\sinh\Big(\frac{\pi\cdot c}{2h}\Big) \tag{3.9}$$

$$k_{1b}(a,b,c) = \sinh\Big(\frac{\pi\cdot b}{2h}\Big)\Big/\sinh\Big(\frac{\pi\cdot c}{2h}\Big) \tag{3.10}$$

$$k_4(a,b,c) = \frac{b}{c}\sqrt{1-\frac{a^2}{b^2}}\sqrt{1-\frac{a^2}{c^2}}^{-1}, \tag{3.11}$$

where

$$a = w_s/2 \tag{3.12}$$

$$b = a + w_{sg} \tag{3.13}$$

$$c = b + w_g \tag{3.14}$$

and h is the substrate thicknes.
Different parts of the fields extend into the air layer above the CPW for each mode [GGB79]. This results in different effective dielectric constants and hence phase velocities. The resulting non-synchronous behavior deteriorates the performance of the CPW. For optimized performance impedance-matching of both

even and odd modes needs to be achieved. No analytical relationship for the overall impedance taking into account both modes was found in the literature. It is important to note that a narrow ground line width w_g causes an impedance increase of the odd mode beyond $50\,\Omega$. Thus wide ground lines are necessary for matching the odd mode to $50\,\Omega$. However, ground line width variation has little impact on the impedance of the even mode. The signal-to-ground separation width w_{sg} influences the impedance of both modes significantly. Reduced signal-to-ground line separation allows for smaller ground line width w_g. As a consequence, simultaneous impedance matching for both modes in a CPW is only achieved by a specific set of design parameter values.
Based on this fact and within the framework of the quasi-static description, we have developed the following design algorithm for our CPWs:

1. Choice of the signal line width w_s according to the specific experimental requirements.
2. First guess of the signal-to-ground line separation distance w_{sg} and ground line width w_g. Implementation in expressions for Z_e, Z_o.
3. Tuning of the even mode impedance to $50\,\Omega$ by variation of w_s in the corresponding expression for Z_e.
4. Tuning of the odd mode impedance to $50\,\Omega$ by variation of w_g in the corresponding expression for Z_o.
5. Final tuning of w_s and w_g to achieve $50\,\Omega$ matching for both modes and the desired value for w_s. Small reduction of w_s can help decrease w_g to comply to possible geometrical restrictions, e. g. additional adjacent structures.

While this method provides us with a good starting point for the layout of our home-made CPWs, it does not take into account the frequency dependence of the impedance due to e.g. skin effect. Furthermore, the analytic treatments in the literature have been tested mainly on mm-sized structures and unravel a multidimensional parameter space determining the transmission characteristics of coplanar structures at low scales.

3.2 Electromagnetic simulations

3.2.1 Taper design

A bottom-up, realistic approach in CPW design departing from Maxwell's equations is achieved with the help of a powerful electromagnetic simulation software such as *CST Microwave Studio*. Simulations allow to monitor accurately the electrical field distortions causing impedance mismatch, especially with respect to different taper lengths L′ (see Fig. 3.3). Design elements

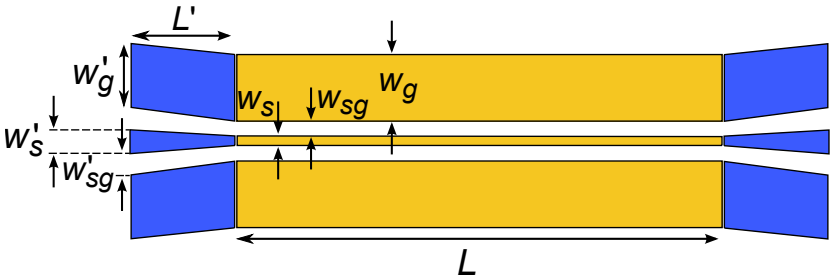

Figure 3.3: Top view of the narrow CPW with annotated design parameters of the main part (yellow) and taper (blue). The same definitions apply to the antenna-CPW. Exact parameter values are given in Appendix B.

are implemented as real, lossy materials providing insight to the skin effect, the dielectric and ohmic losses and the frequency dependence of their electromagnetic properties. Last but not least, optimization tools of the software facilitate the iterative calculation of the optimal dimensions and geometries.
In the following, we summarize our findings regarding the op-

timization of our CPWs going beyond the analytic approach described in the previous section. We focus on the taper part of the narrow CPW, which is required in order to connect the landing pads of the macroscopic MW probes and the main part of the waveguide (shown in yellow in Fig. 3.3). Discussion on the taper design of µm-sized CPWs is rare in the litterature. The existing work concentrated on mm-sized antennae [Fei11], coplanar-to-rectangular waveguide transition elements [Moto5] and tapered impedance transformers [YJ11]. Notably, El-Gibari *et al.* addressed the taper in the framework of transitions between coplanar and µm-sized microstrip lines using the simulation software Ansys HFSS [ElG11].

As discussed in Ref. [Gieo5], the main implication of Eq. (3.1) is that one may change the cross section geometry of a CPW in such a way that the ratio w_s/w_{sg} remains constant without changing the characteristic impedance Z_0. This implies that it is possible to widen the electrodes of the main part linearly as shown in Fig. 3.3 with unchanged impedance. Yet, as structure dimensions vary drastically along this part, reflections are expected to take place between the taper and main part of the CPW. This has serious implications on the transmission characteristics of the overall structure, since the injected signal is deteriorated before even entering the part of the waveguide that is decisive for our experiments.

To confirm that the straight taper geometry shown in Fig. 3.3 represents the optimal design also in the realistic case including finite ground plate width w_g, w'_g and thickness t, we started from an exponentially-shaped taper[1]

$$x(y) = Ae^{\beta y}, \tag{3.15}$$

where x, y are given in µm. This is illustrated in Fig. 3.4. The

1 We were inspired by the exponential form of the silhouette of brass bells used in musical instruments.

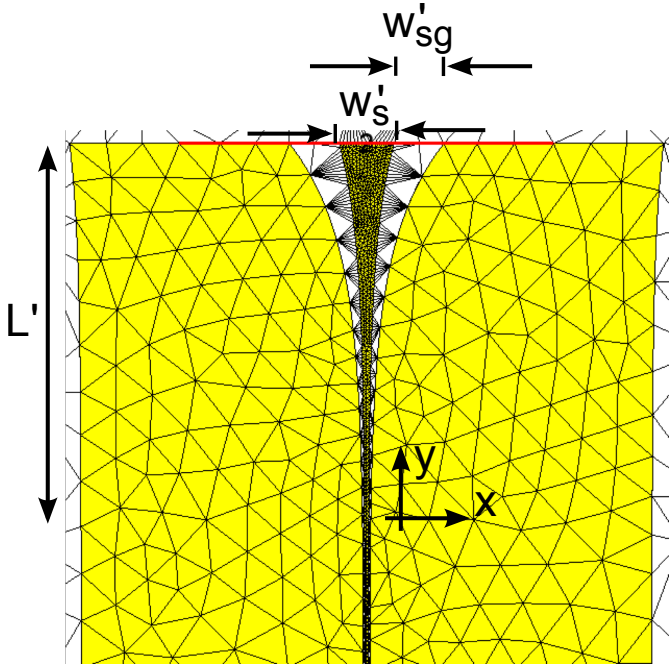

Figure 3.4: Snapshot of the exponential taper implemented in *CST Microwave Studio* for the taper optimization. The red line at the top marks the position of the excitation port.

CPW is depicted in yellow with the mesh cells delimited by black lines. Notice how the region around the signal line and the latter are meshed significantly finer compared to the adjacent ground lines. This is necessary to assure the same calculation accuracy throughout the entire model, despite strongly varying dimensions[2].
We performed simulations for various values of $0.001 \leqslant \beta \leqslant 0.1$ and noticed significant impedance variation only at frequencies

2 Further technical details concerning the simulations with *CST Microwave Studio* are given in Appendix C.

below 1 GHz. The value $\beta \approx 0.001$, corresponding to a practically straight taper design exhibited the highest transmission S_{ij} and lowest reflection S_{ii} with $i, j \in \{1, 2\}; i \neq j$. Hence, in the following we concentrated our efforts on the straight taper design.
The signal line width w_s' was identified as the crucial optimization parameter. A minimum value of 50 µm is required to position MW tips with a 250 µm pitch reproducibly on the signal and ground plates. We obtained the optimal value of $w_s' = 58.2\,\mu m$ for $L' = 450\,\mu m$. When extending the taper length to $L' = 620\,\mu m$, we found that $w_s' = 58.2\,\mu m$ remained as the value satisfying 50 Ω from 10 MHz to 26.5 GHz. For CPWs with narrower signal line width ($w_s = 4\,\mu m$ and $w_s = 2\,\mu m$) the optimum for w_s' also lies at approximately 58.2 µm.

3.2.2 General optimization algorithm

Combining the analytical, quasi-static approach with finite-element electromagnetic simulations, we applied the following design algorithm for our CPWs:

1. Follow the iterative algorithm described in Section 3.1.
2. Optimize the main part of the CPW (without taper) with the optimizer tool of *CST Microwave Studio* by varying the gap w_{sg}, aiming at 50 Ω impedance.
3. Optimize the entire CPW (including the taper) with *CST Microwave Studio* by varying the signal line width of the taper w_s', aiming at 50 Ω impedance. Take care of geometrical constraints, e. g. MW probe pitch and landing precision to ensure proper electrical contact.

4 Magnetic resonance in the field-polarized phase

4.1 Gilbert damping

In this section we investigate the Gilbert damping in Cu_2OSeO_3. To evaluate α_{intr}, we explore the field-polarized (FP) phase, where the two spin sublattices attain the ferrimagnetic arrangement [Bel10]. In Fig. 4.1 (a)-(d) we show spectra recorded using the broad and narrow coplanar waveguides (CPWs) (see Section 2.2.1). The central long axis of the rectangular Cu_2OSeO_3 rods was positioned on the central axis of the waveguides. Only components of the dynamic magnetic field $\mathbf{h} \perp \mathbf{H}$ induce precessional motion in the FP state. For the same applied field H, peaks are found at higher frequency f for $\mathbf{H} \parallel \langle 100 \rangle$ compared to $\mathbf{H} \parallel \langle 111 \rangle$. This observation, related to cubic anisotropy will be discussed in Section 4.3 in further detail.
For the narrow CPW, we observed a broad peak superimposed by a series of resonances that shifted to higher frequencies with increasing H [Fig. 4.1 (a) and (c)]. The field dependence excluded them from being noise or artifacts of the setup. They disappeared with increasing temperature T but the broad peak remained. Their number and relative intensities varied from sample to sample and also upon remounting the same sample in the cryostat (not shown). For the broad CPW [Fig. 4.1 (b)

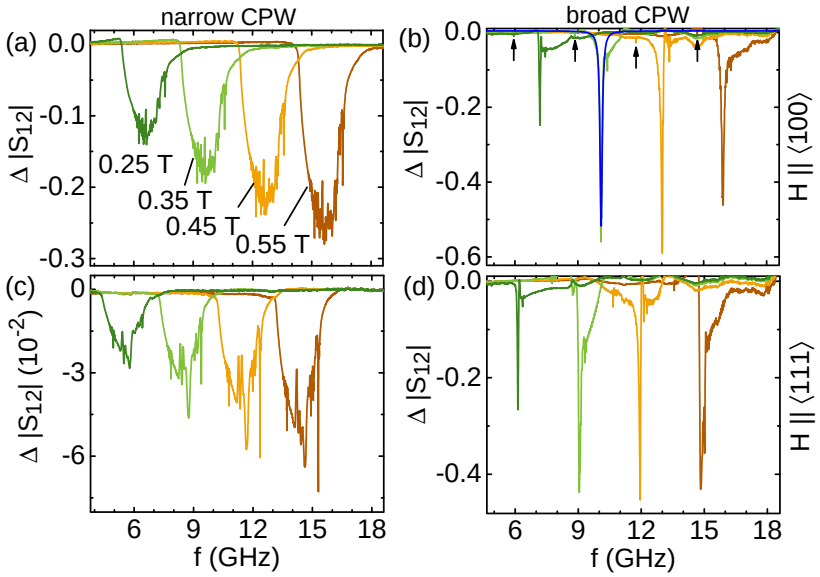

Figure 4.1: Spectra $\Delta|S_{12}|$ obtained at T = 5 K for different H using (a) a narrow and (b) broad CPW when $\mathbf{H} \parallel \langle 100 \rangle$ on sample **A**. Corresponding spectra taken on sample **B** for $\mathbf{H} \parallel \langle 111 \rangle$ are shown in (c) and (d), respectively. Note the strong and sharp resonances in (b) and (d) when using the broad CPW that provides a much more homogeneous excitation field **h**. Arrows mark resonances that have a field-independent offset with the corresponding main peaks and are attributed to standing spin waves. An exemplary Lorentz fit curve is shown in blue color in (b).

and (d)], we measured significantly sharper resonances compared to the narrow CPW. We resolved resonances below the large sharp peaks [arrows in Fig. 4.1 (b)] that exhibited an almost field-independent frequency offset from the main peaks that we will discuss in Section 4.2. Note that, being broader than the sample, the CPW is assumed to excite homogeneously

at $f(k = 0)$ [Igu15] (see also Section 2.2.2). We ascribe thus the intense resonances of Fig. 4.1 (b) and (d) to $f(k = 0)$.
Lorentz curves [blue line in Fig. 4.1 (b)] were fitted to the data recorded with the broad CPW to determine the resonance frequencies and linewidths. Note that the measured linewidth is larger by a factor of $\sqrt{3}$ compared to the linewidth Δf that is conventionally extracted from the imaginary part of the scattering parameters [Sta93]. The linewidths Δf are well described by linear fits based on Eq. (1.34) at different temperatures. This is shown in Fig. 4.2. For comparing the two evaluation routes

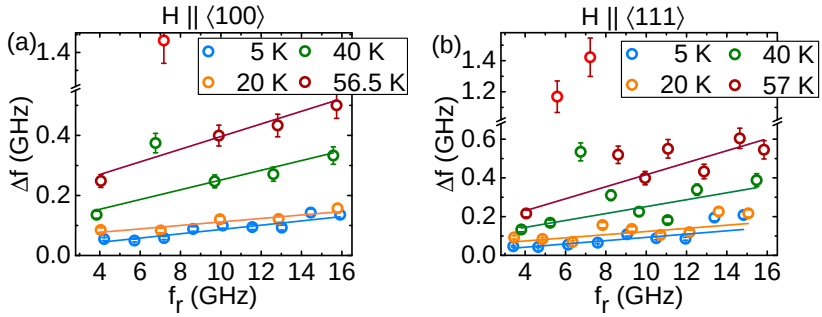

Figure 4.2: Temperature and frequency dependent linewidths for (a) $\mathbf{H} \parallel \langle 100 \rangle$ and (b) $\mathbf{H} \parallel \langle 111 \rangle$ measured with the broad CPW. Linear fits to the data are shown. The red data points have been excluded from the linear fit, because of the presence of strong cable resonances in the spectra, which distort the lineshape.

discussed in Section 1.2.3, we plot the resonance curve taken with the narrow CPW at 15 GHz as a function of field in Fig. 4.3 (a). The curve exhibits no sharp features as H was varied in finite steps (symbols). The linewidth ΔH (symbols) is plotted in Fig. 4.3 (b) for different resonance frequencies and temperatures. Here also we performed the $\sqrt{3}$-correction. The slopes of

linear fits (straight lines) following Eq. (1.33) reflect the intrinsic damping parameters α_{intr}.

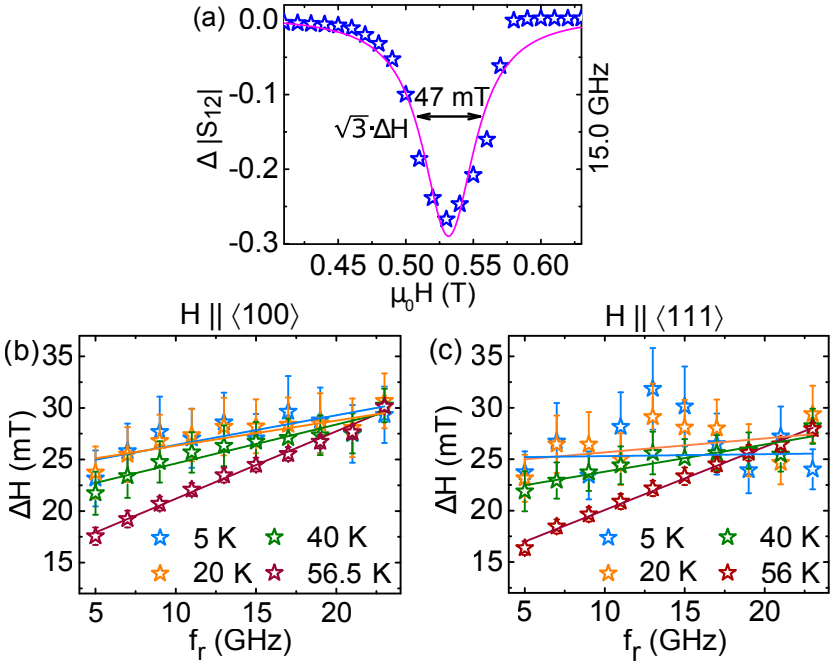

Figure 4.3: (a) Lorentz curve (magneta line) fitted to a resonance (symbols) measured at $f = 15$ GHz as a function of H at 5 K. (b), (c) Frequency dependencies of linewidths ΔH (symbols) for four different T with $\mathbf{H} \parallel \langle 100 \rangle$ and $\mathbf{H} \parallel \langle 111 \rangle$, respectively. The data are well described by linear fits (lines) based on Eq. (1.33).

In Fig. 4.4 (a) and (b) we compare α_{intr} obtained from both the two evaluation routes and different CPWs (circles vs. stars). Note that the resonance peaks measured with the broad CPW were so sharp, as to prevent us from analyzing these data as a function of H. We refrained also from fitting the peaks of Fig. 4.1 (a) and (c) (narrow CPW), due to an asymmetry attributed to the overlap of subresonances at finite wavevector k, as

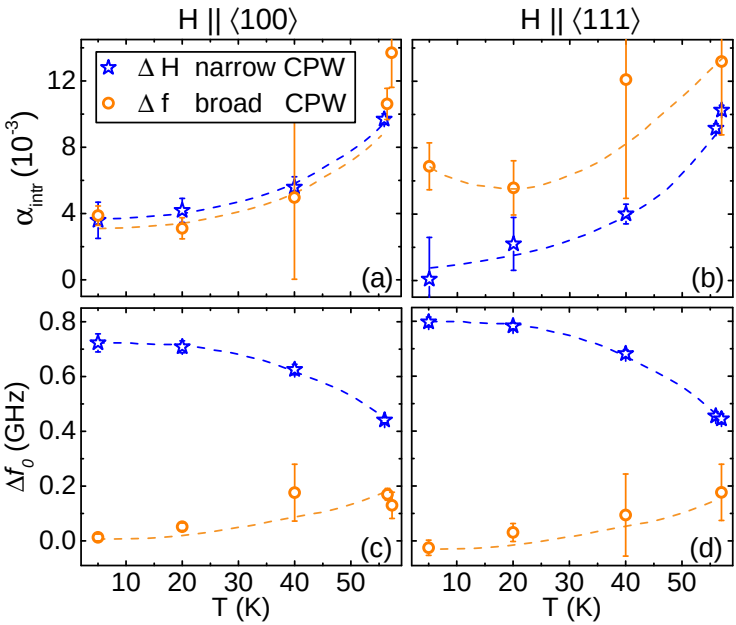

Figure 4.4: (a) and (b) Intrinsic damping parameter α_{intr} and inhomogeneous broadening Δf_0 for two different field directions (see labels) obtained from the slopes and intercepts at $f_r = 0$ of linear fits to the linewidth data [see Fig. 4.3 (b), (c)]. Dashed lines are guides to the eyes.

will be discussed below. For $\mathbf{H} \parallel \langle 100 \rangle$ [Fig. 4.4 (a)], between 5 K and 20 K the lowest value of α_{intr} amounts to $(3.7 \pm 0.4) \times 10^{-3}$. This value is three times lower compared to Ref. [Sch15], due to the increased signal-to-noise ratio (SNR) provided by our CPWs. Beyond 20 K the damping is found to increase. For $\mathbf{H} \parallel \langle 111 \rangle$ [Fig. 4.4 (b)] we extract $(0.6 \pm 0.6) \times 10^{-3}$ as the smallest value. However, we find a discrepancy between the broad and narrow CPW. Note that these values for α_{intr} still contain an extrinsic contribution and thus represent upper bounds for Cu_2OSeO_3,

as we will show later.
For the inhomogeneous broadening Δf_0 in Fig. 4.4 (c), (d) the datasets are consistent (we have used the relation $\Delta f_0 = \gamma \Delta H_0 / 2\pi$ to convert ΔH_0 into Δf_0). We see that Δf_0 increases with T and is small for the broad CPW, independent of the crystallographic direction of H. For the narrow CPW, the inhomogeneous broadening is largest at small T and then decreases by about 40 % up to about 50 K.
In the following, we examine in detail the additional sharp resonances that we observed in our spectra recorded with the narrow CPW [Fig. 4.1 (a) and (c)]. In the insets of Fig. 4.5 (a) and (b) we replot the 0.85 T spectrum for $\mathbf{H} \parallel \langle 100 \rangle$ and $\mathbf{H} \parallel \langle 111 \rangle$, respectively. We highlight prominent and particularly narrow resonances with labels #1, #2 and #3. Their frequency f_r depends linearly on H suggesting a Landé factor $g = 2.14$ at 5 K, only slightly larger than $g = 2.07$ reported for 30 K in Ref. [Sek16].
We now concentrate on mode #1 for $\mathbf{H} \parallel \langle 100 \rangle$ at 5 K that is best resolved. We fit a Lorentzian lineshape as shown in Fig. 4.5 (c) for 0.85 T, and summarize the corresponding linewidths Δf in Fig. 4.5 (d). To determine the Gilbert-type damping, we apply a linear fit to the data points $f_r > 10.6$ GHz and obtain $(9.9 \pm 4.1) \times 10^{-5}$. For $f_r \leqslant 10.6$ GHz the resonance amplitudes of mode #1 were small, degrading thus the confidence of the fitting procedure. Furthermore, at low frequencies, we expect a significant contribution from anisotropy, similar to the results in Ref. [Sil99]. For these reasons, the two points at low f_r were left out for the fit. To check the consistency of the small damping that outperforms metals [Sch16] and comes close to the room temperature value of YIG ($\alpha_{intr} = 3 \times 10^{-5}$ [SCH10]), we evaluated the effective damping $\alpha_{eff} = \Delta f / (2 f_r)$ directly from the linewidth [inset of Fig. 4.5 (d)]. α_{eff} includes both intrinsic damping and inhomogeneous broadening. We find that α_{eff} approaches the value of $(9.9 \pm 4.1) \times 10^{-5}$ with increasing

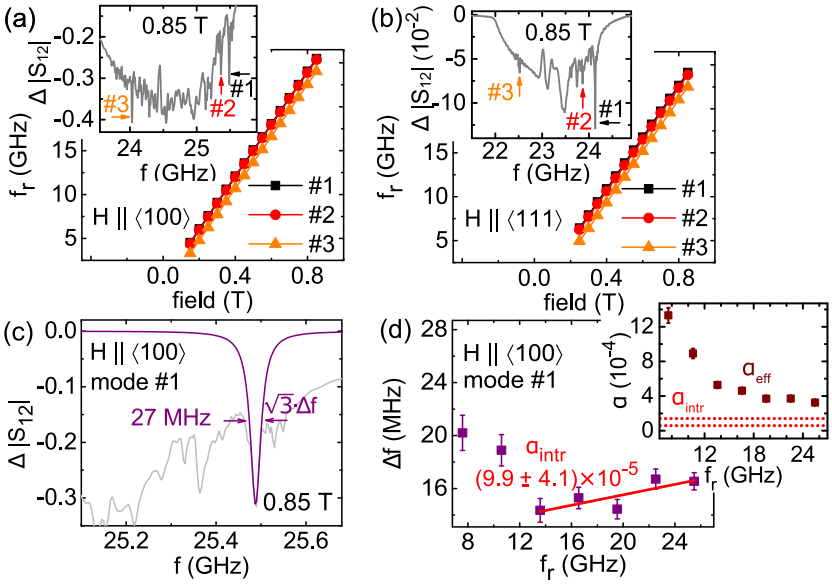

Figure 4.5: (a)-(b) Resonance frequency as a function of field H of selected sharp modes labelled #1 to #3 (see insets) for **H** ∥ ⟨100⟩ and **H** ∥ ⟨111⟩ at T = 5 K. (c) Exemplary Lorentz fit of sharp mode #1 for **H** ∥ ⟨100⟩ at 0.85 T. (d) Extracted linewidth Δf as a function of resonance frequency f_r along with the linear fit performed to determine the intrinsic damping α_{intr} in Cu_2OSeO_3. Inset: Comparison among the extrinsic and intrinsic damping contribution. The red dotted lines mark the error margins of $\alpha_{intr} = (9.9 \pm 4.1) \times 10^{-5}$.

frequency, because the frequency-independent second term in Eq. (1.34) contributes less at large f_r, and Δf becomes dominated by α_{intr}.

Note that our spectra taken with the broad CPW do not show the very small intrinsic linewidth [see Fig. 4.4 (a), (b)]. To confirm this, we evaluated the damping in a third sample with **H** ∥ ⟨100⟩ (sample **C**) using the broad CPW. This is shown in

Fig. 4.6. We obtained $(3.1 \pm 0.3) \times 10^{-3}$, in agreement with the value $(3.7 \pm 0.4) \times 10^{-3}$ reported above.

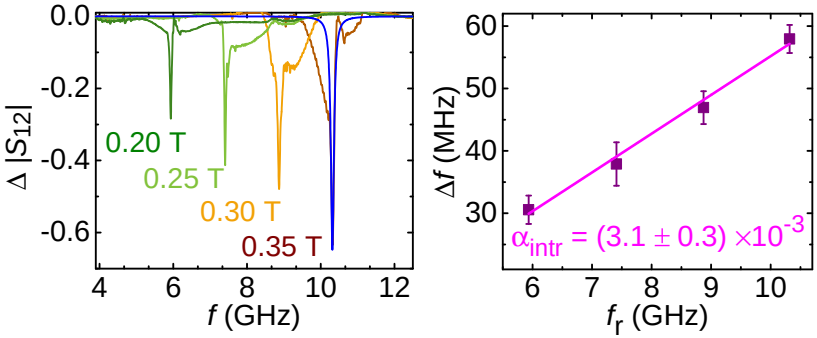

Figure 4.6: (a) Spectra obtained from sample **C** with $\mathbf{H} \parallel \langle 100 \rangle$ at 0.85 T and 5 K using the broad CPW. An exemplary Lorentz fit curve is shown in blue. (b) Frequency dependency of the linewidth Δf (symbols). The evaluated intrinsic damping parameter α_{intr} is in agreement with our results in Fig. 4.4 (a).

Discussion

Preliminary studies on the Gilbert damping parameter α_{intr} in Cu_2OSeO_3 reported a value of 10^{-2} at 5 K [Sch15] and 30 K [Sek16]. The CPW used in Ref. [Sch15] was not optimized, resulting in lower experimental resolution compared to our measurements. In both works, relatively narrow waveguides in the µm range were used and the implications of the excitation profile of the CPWs on the number of modes in the spectra was only partly considered. Seki *et al.* performed Fourier transformation of the dynamic field distribution but did not compare data recorded with CPWs of significantly larger dimensions. Also, data at 5 K were not shown.

In the framework of this thesis, we show that depending on the CPW geometry, considerable extrinsic contribution to the damping Δf_0 arises [Fig. 4.4 (c), (d)] and modifies the distribution of the sharp peaks at 5 K [Fig. 4.1]. The inhomogeneous broadening Δf_0 is found to be smaller for the broad CPW compared to the narrow one. The smaller Δf_0 is consistent with a more homogeneous dynamic field distribution. Still, the intrinsic linewidth is not reached by the broad CPW. At 5 K, the sharp mode #1 yields $\Delta f = 15.3$ MHz at 16.6 GHz [Fig. 4.5 (d)], whereas the dominant peak measured at 0.55 T with the broad CPW has $\Delta f = 129$ MHz at a similar frequency of 15.9 GHz [Fig. 4.1 (b)]. Δf obtained by the broad CPW is thus still a factor of eight larger compared to the intrinsic linewidth, explaining the relatively large Gilbert damping parameter in Fig. 4.4 (a) and (b), compared to the value $\alpha_{\text{intr}} = (9.9 \pm 4.1) \times 10^{-5}$. The discrepancy might arise due to the inhomogeneity of $\mathbf{h}$ as one moves away from the CPW plane (see Section 2.2.1).

We attribute the sharp peaks recorded with the narrow CPW [Fig. 4.1 (a), (c)] to standing spin waves within our sample, allowed for by the low damping. The bulk specimen acts as a resonator with a narrow bandwidth, which naturally selects specific k-vectors provided by the CPW. The narrow CPW transfers more k vectors to the sample compared to the broad CPW (see Section 2.2.2), hence the multitude of sharp peaks in the corresponding spectra. The scaling of $\Delta f(f)$ of individual sharp peaks gives access to the low intrisic damping value $\alpha_{\text{intr}} = (9.9 \pm 4.1) \times 10^{-5}$ reported above.

For comparison, we analyze the sharp peaks shown in the inset of Fig. 4.5 (b), with $\mathbf{H} \parallel \langle 111 \rangle$. We replot the data in Fig. 4.7 (a) and fit the prominent peaks labelled #1 and #4. We summarize the corrected linewidths obtained from a fit to the sharp peak #1 in Fig. 4.7 (b). A linear fit to the data yields $\alpha_{\text{intr}} = (2.6 \pm 0.1) \times 10^{-4}$. There is a discrepancy between α_{intr}

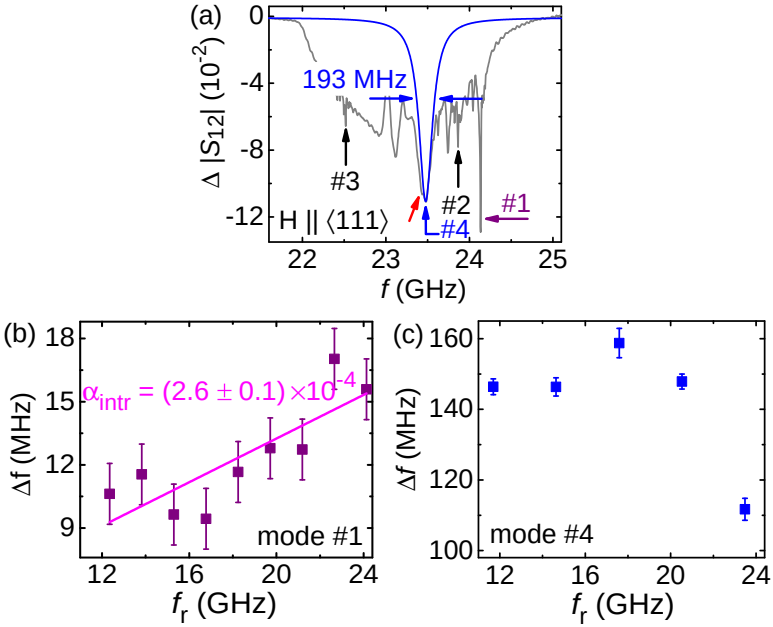

Figure 4.7: (a) Sharp modes for $\mathbf{H} \parallel \langle 111 \rangle$ at 5 K using the narrow CPW. (b), (c) Frequency dependency of the linewidth Δf obtained from modes #1 and #4, respectively. For the latter, we extract α_{intr} from the slope of a linear fit to the data (magenta line). An exemplary Lorentz fit curve of mode #4 is shown in blue.

obtained from the sharp peaks in the case $\mathbf{H} \parallel \langle 111 \rangle$ compared to the value $\alpha_{\text{intr}} = (9.9 \pm 4.1) \times 10^{-5}$, which was obtained when $\mathbf{H} \parallel \langle 100 \rangle$. As will be shown in Section 4.3, we find that the cubic anisotropy energy is extremal for $\mathbf{H} \parallel \langle 100 \rangle$ and $\mathbf{H} \parallel \langle 111 \rangle$, reflecting easy and hard axes, respectively, in Cu_2OSeO_3. We relate the above-mentioned discrepancy to a misalignment of $\mathbf{H}$ with the hard axis, leading to a field-dragging contribution [FZ13].

Note that there is an additional peak to the left of peak #4 (red arrow) with similar intensity as the latter. The rescaled linewidths Δf obtained from peak #4 at different fields [Fig. 4.7 (c)] do not scale linearly with the resonance frequency f_r. We attribute this fact, along with the relatively large linewidth, to the presence of further sharp peaks around 23.5 GHz that were not resolved.

Concerning the temperature dependence, we found that for $\mathbf{H} \parallel \langle 100 \rangle$, the linewidth $\Delta f(T)$ does not scale linearly [Fig. 4.2 (a)]. A deviation from linear scaling was reported for YIG single crystals as well and accounted for by the confluence of a low-k magnon with a phonon or thermally excited magnon [Spa64]. In the case of $\mathbf{H} \parallel \langle 111 \rangle$, we obtain a discrepancy between results from the two evaluation routes and CPWs used [Fig. 4.4 (b)]. We attribute also this to field-dragging contributions from a misalignment of $\mathbf{H}$ with the hard axis $\langle 111 \rangle$. In summary, the comparison between $\mathbf{H} \parallel \langle 100 \rangle$ and $\mathbf{H} \parallel \langle 111 \rangle$ suggests the influence of anisotropy in the latter case, which motivated us to concentrate our standing wave analysis on the case $\mathbf{H} \parallel \langle 100 \rangle$.

Numerous studies on spin wave damping are based on the conversion between frequency and field linewidth (see Ref. [WCS15] and references therein). In their recent work, Wei *et al.* introduced a so-called linewidth contribution ratio to quantify the validity between frequency and field linewidth conversion in thin films [WCS15]. In our bulk measurements we obtain a reasonable conversion for $\mathbf{H} \parallel \langle 100 \rangle$, despite a relatively high ratio value of at least 47 GHz (using $\alpha_{\text{intr}} = 1 \times 10^{-3}$). Also, our analysis fullfills the necessary conditions for the conversion between field and frequency linewidth presented in Section 1.2.3, since we have measured along the easy and hard axes in Cu_2OSeO_3.

4.2 Magnetostatic waves in a bounded medium

We now discuss the origin of the sharp resonances in our spectra. Similar features were reported previously in the FP phase of Cu_2OSeO_3 in Refs. [Kob10; Mai12; Oka15; Ono12]. Kobets *et al.* used a nonellipsoidal sample in a microwave cavity providing a homogeneous excitation field. They attributed sharp features to nonlinear parametric resonances induced by a nonuniformity [Kob10], possibly due to an inhomogeneous internal field [Zhe96]. Furthermore, Kobets and co-workers detected a substructure in the spectra even below the threshold power for nonlinear excitation. Maisuradze *et al.* assigned secondary peaks in thin plates of Cu_2OSeO_3 to standing spin-wave resonance modes.

In the data shown in Fig. 4.1 (b) and recorded with the broad CPW for $\mathbf{H} \parallel \langle 100 \rangle$, we identified sharp resonances that exhibit a characteristic frequency offset δf with the main resonance at all fields (black arrows). We illustrate this in Fig. 4.8 (a) in that we shift spectra of Fig. 4.1 (b) so that the positions of their main resonances overlap.

The magnetization of Cu_2OSeO_3 amounts to $\mu_0 M_S = 0.13\,T$ at 5 K [Ada12]. We discuss data obtained at $\mu_0 H > 0.2\,T$, where H is larger than $(N_z + N_x N_y / N_z) M_S$. Hence the frequency $f(k = 0)$ of uniform precession (FMR) ascribed to the intense resonances of Fig. 4.1 (b) and (d), lies within the expected range for magnetostatic spin waves with a wave vector $k \neq 0$ [GM96]. This means that we deal with frequencies close to the FMR and expression (1.35) provides us with the relaxation time of the spin precession. Using $f_r = 6\,GHz$ and the conservative value $\alpha_{intr} = 3.7 \times 10^{-3}$ at 5 K [Fig. 4.4 (a)], we obtain a minimum relaxation time of $\tau_0^{-1} = 6.6\,ns$. The additional small resonances

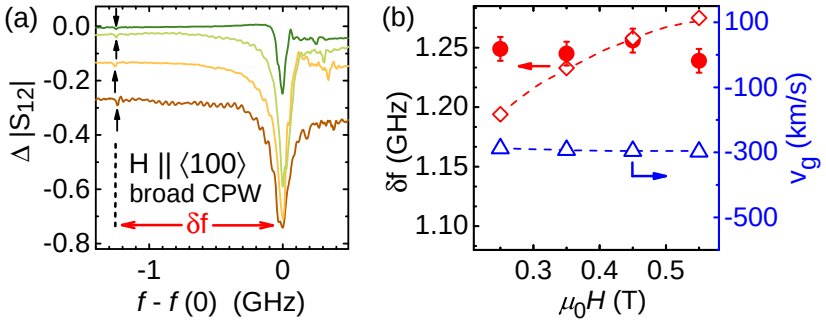

Figure 4.8: (a) Spectra of Fig. 4.1 (b) replotted as $f - f_{k=0}(H)$ for different H such that all main peaks are at zero frequency and the field-independent frequency splitting δf becomes visible. The numerous oscillations seen particularly on the bottom most curve are artefacts from the calibration routine. (b) Experimentally evaluated (filled circles) and theoretically predicted (diamonds) splitting δf using dispersion relations for a platelet. Calculated group velocity v_g at $k = \pi/(0.3\text{ mm})$. Dashed lines are guides to the eyes.

(arrows) in Fig. 4.1 (b) are well below the uniform mode. This is characteristic for standing backward volume magnetostatic spin waves (BVMSWs) with $\mathbf{k} \parallel \mathbf{M}$ [GM96]. Such waves however, can only develop if they are reflected at least once at the bottom and top surface of the sample. The resulting standing waves carry a quasi-momentum $k = n\pi/d$, with order number n and sample thickness $d = 0.3\,\text{mm}$. The BVMSW dispersion relation $f(k)$ of Ref. [Sek16] results in a group velocity $v_g = -300$ km/s at $k = \pi/d$ [triangles in Fig. 4.8 (b)]. Hence, the decay length $l_d = v_g\tau$ amounts to 2 mm. This is larger than twice the sample thickness, thereby allowing standing spin wave modes to form. Based on the dispersion of Ref. [Sek16], we also calculated the frequency splitting $\delta f = f(k = 0) - f(n\pi/d)$ [open diamonds in Fig. 4.8 (b)] when we assume $n = 1$ and $t = 0.4\,\text{mm}$ for the

sample width (the latter enters in the dispersion relation). Filled symbols illustrate the experimental values that agree with the calculated ones within about 60 MHz.
In Fig. 4.9, experimental data (filled symbols) are compared to calculated eigenfrequencies (open symbols) obtained from the spin wave dispersion of Ref. [Sek16][1]. Big and small circles

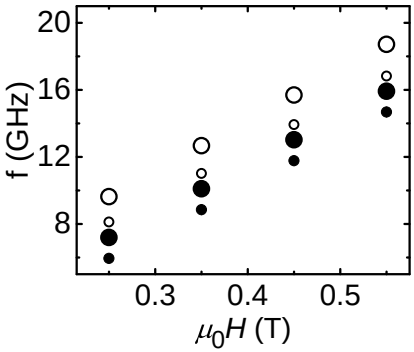

Figure 4.9: Open and filled symbols represent theoretical and experimental data following Ref. [Sek16] and Fig. 4.8 (a), respectively. Large and small symbols indicate the eigenfrequencies of the uniform mode and standing spin wave, respectively.

show the frequency $f(k = 0)$ and $f(k = \pi/d)$, respectively, where $d = 0.3$ mm is the sample thickness along **k**.
Note that the spin-wave propagation in a nonmetallized rectangular rod has no strict analytical solution [GM96] and the dispersion relation taken from Ref. [Sek16] models a platelet instead of a rod. This explains the remaining discrepancy between

1 For consistency, we multiplied our value for the anisotropy constant K (See Section 4.3) by $-2/S^4$, with $S = 0.48$, prior to performing the calculation of Ref. [Sek16]. We considered $M_s = 0.5\,\mu_B/Cu^+$ and $\mu_0 H_{c1} = 0.076$ T at 5 K. Taking this into account, our value for K at 5 K is approximately 3 times higher than the value reported at 30 K in Ref. [Sek16].

closed and open symbols in absolute frequencies. The frequency splitting δf is correctly modelled.

Finally, we discuss two further possible origins of sharp peaks in our spectra. First, localized crystal defects in the order of several hundreds of nanometers or atomic defects are scattering sites for spin waves, that can lead to sharp resonance peaks in resonance measurements [FSW13; HP98; Naz03]. In our analysis of the prominent sharp modes in Fig. 4.5 (a), (b), we showed that the latter exhibit the same Landé factor $g = 2.14$. This value also provides an acurate description of the resonance frequencies measured with the broad CPW and corresponding to the FMR (see next section). As it is not likely that several crystal defects exhibit the same Landé factor, at least the prominent sharp modes mentioned above are not influenced by scattering at localized defects.

Second, the sharp peaks may be provoked by the available directions of $\mathbf{k}$-vectors of our CPWs, combined with the locally nonuniform demagnetization field of our nonellipsoidal samples. Similar observations have been reported in thin films of YIG, where the magnetization dynamics is anisotropic due to dipolar effects [An13]. It has been shown that increasing the inhomogeneity of the internal magnetic field by truncating a spherical YIG sample leads first to the appearance of additional modes clearly separated from the main resonance and eventually to further modes, which broaden the main absorption peak [GC57]. This might be an additional contribution for the observation of various resonances in the spectra of Refs. [Kob10; Mai12] and our work. The thin plates used by Maisuradze et al. exhibit a more homogeneous internal field compared to our rod-shaped samples and presumably of the arbitrarily shaped ones of Ref. [Kob10] (there is no mention of the sample dimensions in their publication). Thus, consistently with our last ex-

planation, a more clear resolution of nonuniform ($k \neq 0$) modes was reported in Ref. [Mai12].

4.3 Cubic anisotropy

We demonstrate the extraction of the anisotropy constant K in Cu_2OSeO_3. In Fig. 4.10, we show the main peak positions f_r recorded with the broad CPW for $\mathbf{H} \parallel \langle 100 \rangle$ (Sample **A**) and $\mathbf{H} \parallel \langle 111 \rangle$ (Sample **B**) at 5 K [see Fig. 4.1 (b), (d)] in the FP phase. We compare this to our calculation (see Section 1.2.2) considering $g = 2.14$ for the Landé factor and fit the value of the anisotropy constant $K = (-0.6 \pm 0.1) \cdot 10^3\,\mathrm{J/m^3}$ to our data. The error corresponds to 5 % deviation between theory and experiment, i.e. approximately half the data point symbol size. We also plot the Kittel formula (1.29) as the gray line, where the cubic anisotropy is neglected.

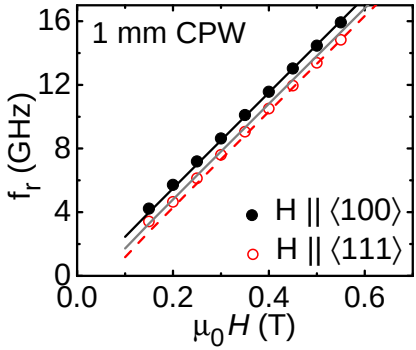

Figure 4.10: Comparison of data recorded with the broad CPW and theoretical calculation including cubic anisotropy at 5 K. The black solid and red dashed lines show the expected resonance frequency for $\mathbf{H} \parallel \langle 100 \rangle$ and $\mathbf{H} \parallel \langle 111 \rangle$, respectively. The gray line corresponds to the Kittel formula (1.29).

5 Magnetic resonance in the noncollinear spin phases

5.1 Linearly polarized magnetization dynamics

For our experiments we mounted the bar-shaped sample **A** on the broad CPW as shown in Fig. 2.12. The static magnetic field **H** is applied perpendicular to the substrate, i.e. along the z axis, being collinear with a $\langle 100 \rangle$ axis of the crystal. As will be shown in the following, we investigate different sample placements by rotation of the sample on the CPW. Note that the demagentization factors N_x and N_y interchange their values if the sample is rotated by 90° in the xy plane [GM96], where our reference system is fixed.
The assembly was cooled down to a temperature in the vicinity of 57 K, where the SkL is present. For each sample placement described in the following, the thermal contact between the sample, the CPW and the sample stage varied. The exact values for T and the H_{c2} values used to normalize the data are given in Tab. 5.1.

Probing configuration	(a)	(b)	(c)	(d)
nominal T (K)	57.3	57.5	56.5	56.5
$\mu_0 H_{c2}$ (mT)	45	48	58	58

Table 5.1: Nominal temperature (measured at the sample stage) and extracted values of the critical field H_{c2} for the different probing configurations shown in Fig. 5.1 (a)-(d). The uncertainty in $\mu_0 H_{c2}$ is estimated to be ± 1 mT.

Experimental results

Figure 5.1 shows spectra recorded for successively decreased fields in the few GHz (RF) frequency regime for the different sample placements and orientations. In Fig. 5.1 (a), the 0.4 mm wide sample **A** lies on the central axis of the 1 mm wide signal line of the CPW. The component h_x of **h** provides the relevant torque [GM96] for spin excitation. In the helical phase ($H = 0$), we resolve a single resonance at $f \approx 1.8$ GHz. For increasing H, the sample enters the conical phase and this resonance shifts to lower frequency. At intermediate fields (red lines at 16-24 mT) two weak resonances are observed. We attribute the corresponding field regime to the SkL phase, consistent with [Ono12] and measurements on thermodynamic properties performed on Cu_2OSeO_3, such as specific heat or magnetic susceptibility (not shown). Following Refs. [Moc12; Ono12], we conclude that h_x excites the counterclockwise (CCW) and clockwise (CW) modes. Next, we place the sample collinear with the CPW and above the gap between ground and signal line [Fig. 5.1 (b)]. We observe a similar sequence of spectra as a function of H, compared to Fig. 5.1 (a). A detailed analysis of eigenfrequencies f is shown in Fig. 5.2 (a). In the SkL phase (red region) the prominent SkL

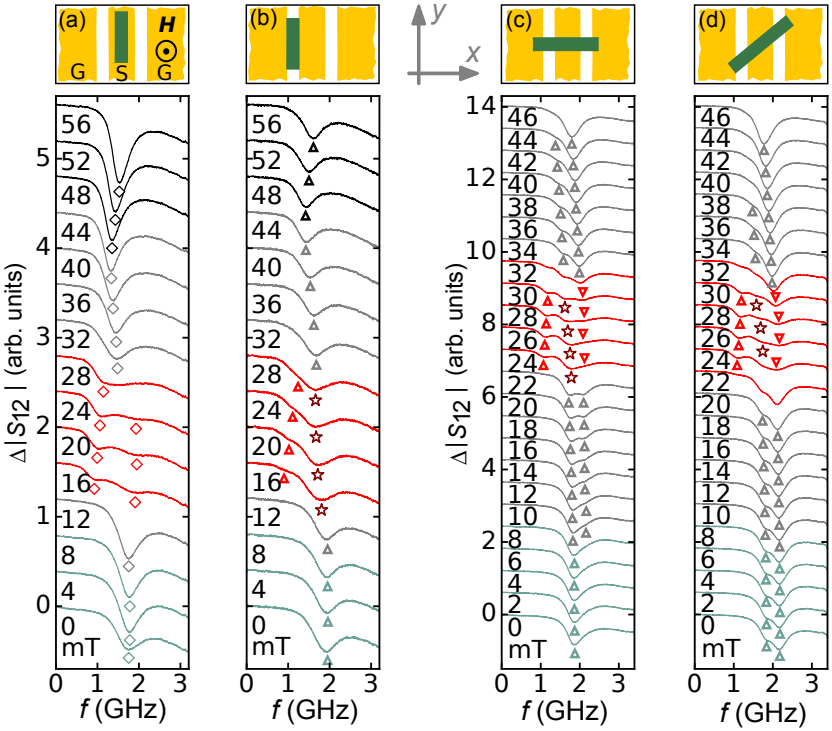

Figure 5.1: Spectra (shifted vertically for clarity) used to extract the field dependencies of resonance frequencies when placing the specimen differently on the broad coplanar waveguide. Spectra taken in the field-polarized (FP), conical (C), Skyrmion (SkL) and helical (H) phase are shown in black, gray, red and green, respectively. Symbols are introduced to mark resonance frequencies (compare Fig. 5.2). Some spectra are taken at field values that coincide with a phase boundary, where phases might have coexisted in the macroscopic sample due to inhomogeneities. Here, the mode allocation is not clear and omitted.

mode recorded with the sample above the gap (brown stars) exhibits a different field dependence and resides elsewhere com-

pared to the first sample placement discussed (red diamonds). We attribute this distinct behavior to the out-of-plane compon-

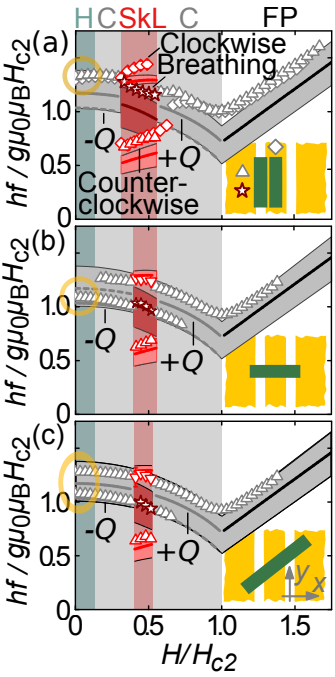

Figure 5.2: Comparison of measured and calculated resonance frequencies in normalized units, following Ref. [Sch15]. Background colors illustrate different phases (see Fig. 5.1). Lines and shaded bands correspond to calculations assuming a homogeneous ($k = 0$) and inhomogeneous ($k \neq 0$) dynamic field, respectively. Dashed lines indicate modes with small spectral weight. Yellow circles highlight the varying number of modes resolved at small H.

ent h_z of **h** (see Fig. 2.4) favoring the excitation of a prominent breathing mode BR [Moc12; Ono12]. The weak shoulder observed at lower frequency in Fig. 5.1 (b) and whose field de-

pendence is tracked in Fig. 5.2 (a) (red triangles) corresponds to the CCW mode. The latter is weakly excited due to the slight overlap of the sample with the signal and ground lines. For the same reason, we resolve resonances in the conical and FP phase at finite fields, which is a priori not expected in the configuration $\mathbf{H} \parallel \mathbf{h}$. We will address this issue in further detail in Section 5.3.

When rotating the sample by 90° [Fig. 5.1 (c)], the spectra change significantly. At 18-22 mT, in the conical state, we resolve two modes that are of similar signal strength. With increasing H, the low-frequency mode successively vanishes (spectra at 34-46 mT). In the SkL phase, all three modes CCW, BR and CW are seen in one-and-the-same spectrum (compare 24-30 mT), due to simultaneous excitation via both h_x (signal line) and h_z (gap). Still, only one resonance is seen in the helical phase at $H = 0$ in Fig. 5.1 (c). Strikingly, for a sample placement at 45° [Fig. 5.1 (d)] we identify two modes at $H = 0$.

Considering Fig. 5.2 (a), we attribute the single resonance, that we resolved in H and C, to mode $+Q$. We did not observe mode $-Q$ when the long axis of the sample and the CPW were collinear. We note that qualitatively, in all the different magnetic phases, the measured eigenfrequencies (symbols) follow well the predicted field dependencies (lines) by the theory of Ref. [Sch15]. The lines show the expected eigenfrequencies for a homogeneous excitation. We observe that the data points lie systematically near the upper gray and dark-red band edges. This corresponds to an inhomogeneity of h_x along z[1]. These observations suggest a nonzero wave vector provided by the the CPW.

From Fig. 5.2 (b) we extract that, rotating the sample by 90° on the CPW, the single resonance detected near $H = 0$ is no longer

1 Interestingly, the upper bad edge for the breathing SkL mode corresponds to an inhomogeneity of h_z along x.

mode +Q, but mode −Q. We thus selected the complementary helical mode at $H = 0$ by interchanging the demagnetization factors. Mode +Q appears only for large H.
Figure 5.2 (c) evidences that for a rotation by 45° both modes +Q and −Q are detected in the same spectrum at $H = 0$. In the litarature, two resonances were sometimes reported [Ono12], but the occurrence or absence of a double peak was not explained. Our experiments now suggest that at small H a cross-polarization exists between the linearly polarized excitation field **h** and either mode −Q or +Q in Fig. 5.2 (a) and 5.2 (b), respectively. Note that the detection of the ferromagnetic resonance in the FP phase does not depend on the sample placement. The DMI-induced spin texture is thus decisive for the characteristic low-field dynamics.

Linear polarization of the average magnetization

We now explain our observations in detail by considering the ellipticity of magnetization precession in the spin helix phases. We make use of the theoretical approach outlined in detail in the Supplementary Information of Ref. [Sch15]. There, spectral weights Γ of different modes were discussed, but ellipticity and polarization of the average magnetization precession were not evaluated.
An RF field within a plane perpendicular to **Q** excites the two modes +Q and −Q with a weight that depends on its polarization within this plane, as we show in the following. It is instructive to introduce the corresponding homogeneous dynamic magnetization $\mathbf{m}_\sigma$ averaged along a helix period ($\sigma = +1$ and -1 for the +Q and −Q mode, respectively). For a helix with **Q**

in z direction, $\mathbf{m}_\sigma = (m_\sigma^x, m_\sigma^y)$ oscillates in the xy plane, characterized by its handedness and ellipticity

$$|\varepsilon_\sigma| = \frac{\sqrt{\left|m_\sigma^{x\,2} - m_\sigma^{y\,2}\right|}}{\max[m_\sigma^x, m_\sigma^y]}, \tag{5.1}$$

in analogy to the case of a ferromagnet [see Eq. (1.37)]. The oscillation of $\mathbf{m}_\sigma$ is always counterclockwise and clockwise for the $+Q$ and $-Q$ mode, respectively, considering that $\mathbf{Q}$ points towards the observer. The handedness of the $+Q$ mode coincides with the one of the local spin precession and thus with the Kittel mode in the FP phase. Therefore, they smoothly connect at H_{c2}, while the weight of the $-Q$ mode vanishes close to the critical field H_{c2}.

Disc-shaped sample

In a disk-shaped sample ($N_x = N_y = 0.235$) at $H = 0$ the oscillation is circular with zero ellipticity for symmetry reasons [Fig. 5.3 (a)]. As a linearly polarized excitation field $\mathbf{h}$ in the xy plane is equivalent to the superposition of left- and right-circularly polarized components, it couples equally well to the two modes $+Q$ and $-Q$ and leads to the same nonzero spectral weight Γ_σ for both modes [Fig. 5.3 (c)]. For $H \neq 0$ applied along $\mathbf{Q}$, the precessional motion stays circularly polarized. The mode $-Q$, however, being right-circular, does not comply to the left-handedness imposed by the Landau-Lifshitz equation of motion (see Section 1.2.1). The resulting imbalance in precession amplitude compared to $+Q$ is indicated by bold and broken lines in Fig. 5.3 (c) (see Γ_σ at $N_x = 0.235$). The imbalance increases with increasing H. Hence, for a disk-shaped sample the $\pm Q$

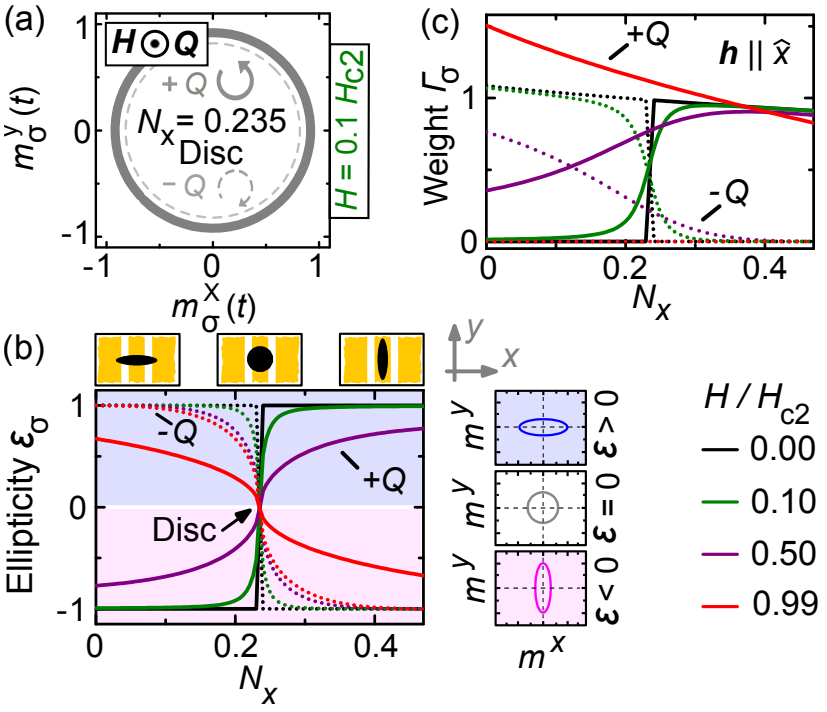

Figure 5.3: (a), Dynamic components of the circularly polarized modes $+Q$ and $-Q$ in a round, flat sample ($N_x = N_y < N_z$) with a small field H applied along $\hat{z}$. The width of lines indicates the relative signal strength. (b) Ellipticity ε_σ of the conical modes as a function of the demagnetization factor N_x ($N_z = 0.53$) calculated for different magnetic fields (colors). Solid and dotted lines represent modes $+Q$ and $-Q$. The insets illustrate the sample shapes corresponding to N_x (top) and the elliptic trajectory of the average spin precessional motion (right). (c) Spectral weight Γ_σ of the conical modes (arb. units) for an excitation field $\mathbf{h}$ along $\hat{x}$.

modes are circularly polarized ($\varepsilon_\sigma = 0$) for all fields $H < H_{c2}$ for symmetry reasons.

Elliptically-shaped sample

As soon as the rotational symmetry of the sample shape is broken, e.g. an ellipsoidal shape within the xy plane, where $N_x \neq N_y$, the polarization of the $\pm$ Q modes is no longer circular and ε_σ becomes finite. This is illustrated in the main panel of Fig. 5.3 (b), where we show ellipticities calculated for $0 \leqslant N_x \leqslant 1 - N_z$ at different field values. We set ε_σ positive and negative for the long principal axis being along $\hat{x}$ and $\hat{y}$, respectively [sketches on the right side of Fig. 5.3 (b)].
We first focus on ε_σ in zero field (black lines) where ε_σ is fully determined by the symmetries of the helix. For a disc ($N_x = N_y$), the screw symmetry of the helix ensures that the two excitation modes are degenerate at $H = 0$ so that any polarization can be achieved. This degeneracy is lifted for $N_x \neq N_y$ and the modes become strictly linearly polarized. In zero field, the spins of the chiral magnet align perpendicular to the helical propagation vector $\mathbf{Q}$, so that the helix possesses a 180°-rotation symmetry around each of its spins. By virtue of this symmetry, there exist always pairs of spins within the helix, whose precessional motion conspire to yield a linear polarization along one of the principal axes, i.e. x or y. As a consequence, the ellipticities of modes $+Q$ (solid line) and $-Q$ (dotted line) follow *step functions*

$$\varepsilon_\sigma|_{H=0} = \operatorname{sgn}\left[\sigma \cdot (N_x - N_y)\right] \tag{5.2}$$

with $\sigma = \pm 1$. This reflects an unexpectedly pronounced sensitivity regarding the sample shape.
The characteristic shape dependence of ε_σ has an impact on the

spectral weights Γ_σ [Fig. 5.3 (c)]. For the spectral weight of the $\pm Q$ modes at $H = 0$ for an ac field $\mathbf{h}$ along the x direction we find[2]

$$\Gamma_\sigma(N_x, N_y)\big|_{H=0} \propto \frac{\Theta\big[\sigma \cdot (N_x - N_y)\big]}{1 + (2 + N_x)\chi^{\text{int}}_{\text{con}}/6}, \tag{5.3}$$

with the internal conical susceptibility $\chi^{\text{int}}_{\text{con}}$ [see Eq. (1.48)] and the Heaviside step function $\Theta(s) = 1$ for $s > 0$ and zero otherwise. Hence, selective excitation of either mode $+Q$ or $-Q$ can be realized. For instance, mode $+Q$ is polarized along $\hat{y}$ ($\epsilon_+ = -1$) for $N_x < N_y$. This is illustrated in Fig.[3] 5.4 (a). An rf field $\mathbf{h}$ along $\hat{x}$ does not couple to its precessional motion and, as a consequence, the spectral weight Γ_+ is zero in the helical phase at $H = 0$ (full black line in Fig. 5.3 (c) for $N_x < 0.235$). For mode $-Q$, $\epsilon_- = +1$ [polarized along $\hat{x} \parallel \mathbf{h}$ in Fig. 5.4 (b)] and Γ_- is large [dotted black line in Fig. 5.3 (c) for $N_x < 0.235$].

For $H > 0$, spins within the helix cant towards the field direction forming the conical state. Note that considering the ellipticities and spectral weights of both modes in Fig. 5.3 (b) and (c), respectively, their field dependencies are not symmetric with respect to $N_x = 0.235$ (disk-like shape). For $N_x \ll N_y$, ε_- of mode $-Q$ stays close to $+1$ [colored dotted lines in Fig. 5.3 (b) for $N_x < 0.235$] and its linear polarization persists over a remarkably large field range. We extract $\varepsilon_- = 0.999$ at $H = 0.5\, H_{c2}$ for $N_x = 0.07$ (our sample) so that an rf field $\mathbf{h} \parallel \hat{x}$ can couple to the $-Q$ mode. Nevertheless, the spectral weight Γ_- decreases significantly with increasing H towards H_{c2} [colored dotted lines in Fig. 5.3 (c)] because of the mismatch of handedness with the Kittel mode within the FP phase as discussed above. Conversely, Γ_+ grows much with H as the ellipticity $|\varepsilon_+|$ of

2 The calculation was performed by Johannes Waizner (University of Cologne) and Markus Garst (TU Dresden).

3 Johannes Waizner, private communication.

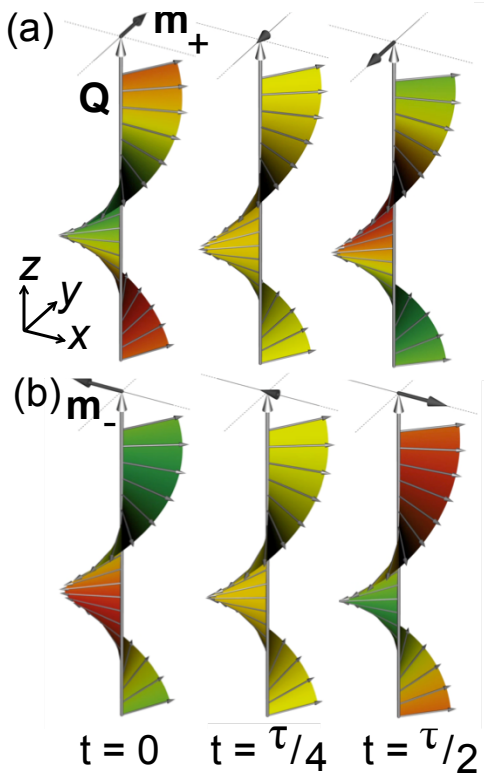

Figure 5.4: Illustrations of precessional motion of spins (thin gray arrows) and averaged dynamic magnetization $\mathbf{m}_\sigma(x, y, t)$ with $\sigma = +, -$ (dark arrows) for selected times t during a period τ of modes (a) $+Q$ and (b) $-Q$. Colors indicate the phase evolution along the helical propagation vector $\mathbf{Q}$. Red and green color highlights, respectively, smaller and larger misalignment angle between neighboring spins compared to their equilibrium position (yellow). We modelled our sample with $N_x < N_y$ at $H = 0$, evidencing the extraordinary linear polarization of $\mathbf{m}$.

the mode +Q first decreases reaching circular polarization at $H_{circ} \approx 0.76\, H_{c2}$ and then increases again staying below $\varepsilon_+ = 1$ [colored full lines in Fig. 5.3 (b)]. These features explain our experimental observations in Fig. 5.1 (c) and 5.1 (f), in which signal strengths of mode −Q and +Q interchange completely with increasing H. The diagonal placement of Fig. 5.1 (d) allows us to detect both modes +Q and −Q at $H = 0$ as $\mathbf{h} \parallel \hat{x}$ can be decomposed into equal components along and transverse to the bar-shaped Cu_2OSeO_3. Still, the signal strengths of mode +Q and −Q are found to be different at $H = 0$.

We have applied the same formalism to the three eigenmodes of the SkL phase. As this phase only exists at a finite magnetic field H, the clockwise and counterclockwise modes are always elliptically polarized with a finite ε, whereas the breathing mode is linearly polarized by symmetry and can be excited only with the help of a longitudinal dynamical field h_z.

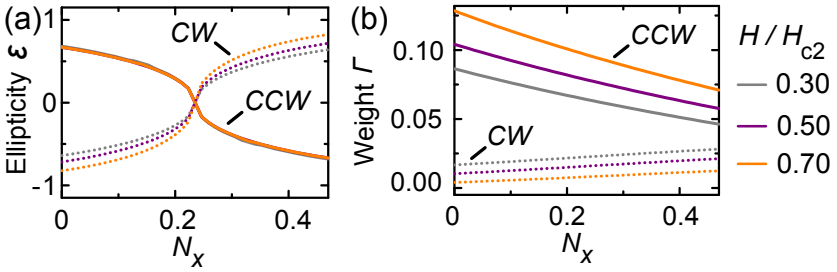

Figure 5.5: (a) Ellipticity ε of the gyrational SkL modes as a function of the demagnetization factor N_x ($N_z = 0.53$) calculated for different magnetic fields (colors), at which the SkL is stable. Solid and dotted lines represent the counter-clockwise (CCW) and clockwise (CW) SkL modes, respectively. (b) Spectral weight Γ of SkL modes for an excitation field **h** along $\hat{x}$.

In Fig. 5.5 we show the results of our calculation for the el-

lipticity and spectral weight distribution of the gyrational SkL modes, CCW and CW. We concentrate on field values around $0.5\,H_{c2}$, where the SkL phase is stable. We find that linear polarization, i.e. $|\varepsilon| = 1$ is not achieved for any sample shape. The spectral weight Γ of the CCW mode is larger compared to the CW mode for every sample shape. The mean magnetization oscillates counter-clockwise and clockwise for the CCW and CW mode, respectively, within the plane perpendicular to the applied magnetic field H (pointing towards the observer). The spectral weight of the CCW mode increases with increasing field. For the CW mode one finds the opposite trend. Note that the ellipticity of the CCW mode is practically independent of the field and already well described by the Kittel expression of Eq. (1.38). This fact indicates that the dynamics of the CCW mode is effectively dominated by the polarized background. As the CCW and CW modes are elliptically polarized, either sample placement that covers CPW signal line *and* gaps allows one to monitor them in the same spectrum.

Discussion

We have observed linearly polarized magnetization dynamics for the modes $+Q$ and $-Q$ of the magnetic helix in Cu_2OSeO_3. In the spin helix, the effective magnetic field $\mathbf{H}_{\text{eff}}$ is inhomogeneous and rotates, as one moves along the pitch vector $\mathbf{Q}$. Hence, for each spin there is another one pointing in the opposite direction. At $H = 0$, the *added* precession within such a spin pair is linearly polarized, similar to the superposition of right- and left-circular polarized light resulting in linearly-polarized light. This mechanism is already known from easy-plane antiferromagnets (AFMs) [ST63], where spins with opposite orientation belong to two sublattices. In the spin helix phase, however, there

exists a *continuum* of spin sublattices with different orientations, which all conspire to yield linear polarization of the average magnetization along a single, well-defined axis of polarization. A priori, this is not obvious due to the multitude of available precession directions and the inhomogeneous precession of the spins within a helix pitch length λ_{helix}.
Another important difference of the helix dynamics compared to easy-plane AFMs with linear polarization is the low eigenfrequency of the former ($\approx 2\,\text{GHz}$). For comparison, typical eigenfrequencies in AFMs lie in the THz-regime [Kam11; Kla04; ST63]. This difference is explained by the fact that the dynamics in the spin helix and in AFMs is dominated by the dipolar and exchange interaction, respectively (see Section 1.1). Additionally, following Eq. (5.2), the linear polarization in chiral magnets arises as soon as the sample shape deviates from a perfect rotational symmetry, such as a flat disc, cylinder or sphere. This striking sensitivity on the sample shape is not anticipated for ferromagnets (see Section 1.2.4). Furthermore, it is known neither from ferrimagnets or easy-plane AFMs. These unique features are attributed to the presence of DMI in chiral magnets and have not been addressed before. Last but not least, the polarization characteristics in Cu_2OSeO_3 are modified and controlled by fields on the order of $10^{-2}\,\text{T}$.

In terms of technological applications, the precession of magnetic moments is exploited in e.g. power limiters, oscillators and tunable bandpass filters. Spheres prepared from the bulk ferrimagnetic insulator YIG offer excellent quality factors in such applications. Moreover, the nonreciprocal characteristics of magnetic materials are functionalized in microwave circulators and isolators. Yet, for an efficient operation, the magnetic excitations and microwaves require a common polarization, which is usually not the case. Microwaves provided by stand-

ard coaxial cables, CPWs and microwave cavities are linearly polarized. In case of a YIG sphere, the polarization is circular ($\epsilon = 0$). Hence 50 % of the microwave energy is not coupled to the spin system and might be wasted. Nonreciprocal devices do not function due to the mismatch of polarization. This is a drawback for future on-chip resonators in particular, that exploit coupled magnons and photons for quantum information processing [Gor14; Hue13; Tab14; Zha14].

To tackle this coupling issue, sophisticated waveguides and cavity designs had to be invented to produce microwaves with a high degree of circular polarization [Dun57; Poo67; Wen69; Yas16]. Demagnetization fields also help increasing the ellipticity of the magnetization precession in ferromagnetic rods with extremely large length-to-diameter ratios and very thin films [GM96; Grü08; LL35; Ziv02]. Here, the ellipticity approaches values close to one, but strict linear polarization is not achievable (see Section 1.2.4). Alternatively, magnetocrystalline anisotropy and antiferromagnetism may be considered to enlarge the ellipticity even in spherical samples. However, the working frequency increases to several 10 GHz or even near-infrared frequencies (THz) [Kam11; Kla04; ST63] exceeding by far the relevant frequency range for microwave applications. The above shows that integration with microwave electronics could be significantly improved with a ferrimagnetic insulator similar to YIG, but possessing linearly polarized magnetization dynamics in the few-GHz regime.

In Fig. 5.6 we show the real part of the complex effective microwave susceptibility χ_{eff} [see Eq. (2.29) and Fig. 1.3] recorded at 57.3 K for different fields in Cu_2OSeO_3. The resonance positions (inflection points) of the curves coincide and their amplitude is similar. At resonance, the susceptibility is characterized by the saturation magnetization M and the intrinsic Gilbert damping α_{intr} [see Eq. (1.28)]. Cu_2OSeO_3 and the

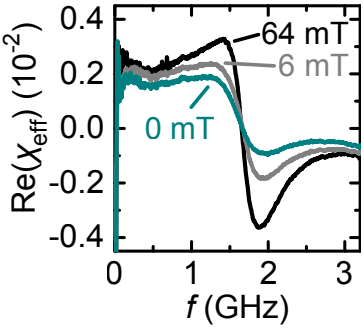

Figure 5.6: Real part of the effective dynamic susceptibility at resonance in the helical (0 mT), conical (6 mT), and field-polarised (64 mT) phase at 57.3 K. χ_{eff} was rotated by an angle of 30° to compensate for the slight impedance mismatch between the sample and CPW. The phases corresponding to the spectra shown here exhibit different polarizations [see Fig. 5.3 (b)].

benchmark material YIG share a similar magnetization $\mu_0 M$ of 0.13 T [Ada12; Sch15] and 0.18 T [dKel13], respectively. In Section 4.1 we showed that α_{intr} is low in Cu_2OSeO_3. These facts suggest that both materials have similar dynamic susceptibility values and that insulating chiral magnets with similar properties to Cu_2OSeO_3 are relevant for microwave applications. Additionally, in such materials the transition between different energetically degenerate phases with similar $\text{Re}(\chi_{\text{eff}})$, and with different polarization (linear and elliptical) is possible via application of an external magnetic field [see Fig. 5.6 and Fig. 5.3 (b)]. The switching between the two extreme cases of linear and almost circular polarization is possible by tailoring of the sample shape. These novel features of chiral magnets add up new functionalities on top of the variety of their fascinating topological properties [FCS13; Jon10; Mil13; Neu09; NT13; Sch12].

5.2 Cubic anisotropy

Samples **D** and **B** were positioned on the narrow CPW as shown in the top inset of Figs. 5.7 (a) and (b), respectively. The field H is parallel to $\langle 100 \rangle$ and $\langle 111 \rangle$ for each sample, respectively. In agreement with the results discussed in Section 5.1, the spectra recorded at 57 K contain three modes in the SkL phase (red) and a single resonance in the helical/conical state (green and gray, respectively) attributed to the +Q mode. We encounter only a small shift of eigenfrequencies among spectra recorded at the same field.

In Fig. 5.7 (c) we plot the resonance frequencies against the theoretical prediction for a homogeneous excitation (lines) in a rod-shaped sample, neglecting cubic anisotropy. The data for both crystallographic directions overlap and show excellent agreement with the theory. These results are consistent with the cubic anisotropy being the weakest energy scale in the chiral magnet [BJ80].

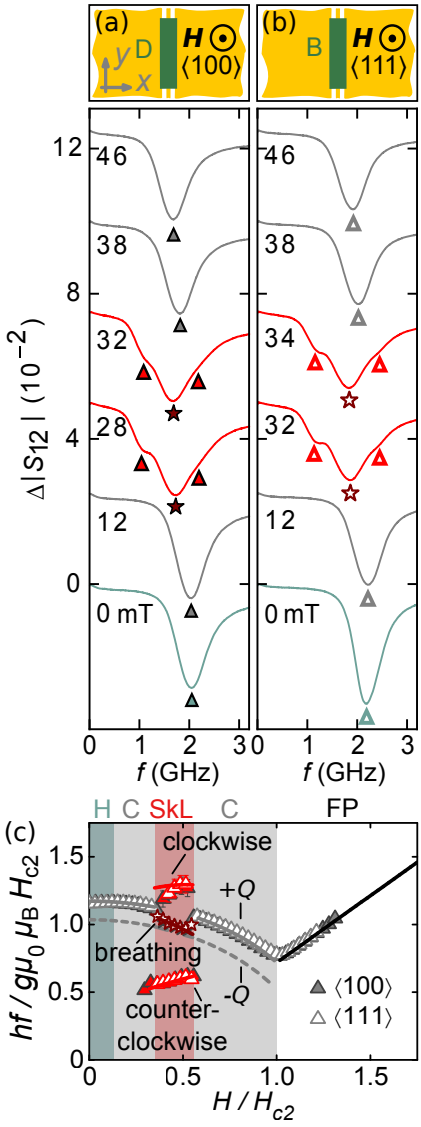

Figure 5.7: Spectra recorded with the narrow CPW for (a) H ∥ ⟨100⟩ and (b) H ∥ ⟨111⟩ at 57 K. (c), The resonance frequencies for both crystallographic directions (open and filled triangles) overlap and show excellent agreement with the calculation.

5.3 VTI measurements

In this section, we present data recorded on Sample **D**, mounted with the long axis parallel to the broad CPW, i.e. there are no parts of the sample over the gap between the signal and ground lines. Hence, only an excitation field $\mathbf{h}$ lying in the plane of the CPW is present (see sketch in Fig. 5.8 and Fig. 2.4). Also, based on our results in Section 5.1, we expect the excitation only of the $+Q$ helix eigenmode, because the long axis of the sample is always perpendicular to $\mathbf{h}$. The temperature at the sensor was 52.3 K. The temperature at the sample is estimated to be about 57 K, since we resolve the dynamics of the SkL, as will be shown in the following. For all the $|\Delta S_{12}|$ data presented in this section we have applied the reference subtraction method (see Section 2.5.4) using a reference dataset recorded at 0.3 T.

The superconducting split coil of the magnet provides us with the field along $\phi = 0°$ (see Fig. 5.8 for the angle definitions) and has a remanence of (28 ± 1) mT. We corrected the data recorded at $\phi = 0°$ by the offset of 28 mT. When measuring with the nominal setting $\phi = 90°$, we plot our data against the applied H_z component (provided by the single superconducting coil). Under this setting, the remanent field along y is present.

In Fig. 5.8 (a) we show color-coded microwave absorption data recorded at $\phi = \theta = 0°$, i.e. $\mathbf{H} \perp \mathbf{h}$. Dark blue regions denote high energy absorption by the specimen. A weak signal (arrows) is observed at about $\mu_0 H = \pm 24$ mT.

We rotated the sample rod around the z-axis to obtain the configuration $\phi = 0°$, $\theta = 90°$, i.e. $\mathbf{H} \parallel \mathbf{h}$. In the corresponding data [Fig. 5.8 (b)], only three regions show microwave absorption within the entire parameter space covered. The regions marked by arrows are of similar extent as in Fig. 5.8 (a) and are found in a similar field regime, yet they lie somewhat higher in

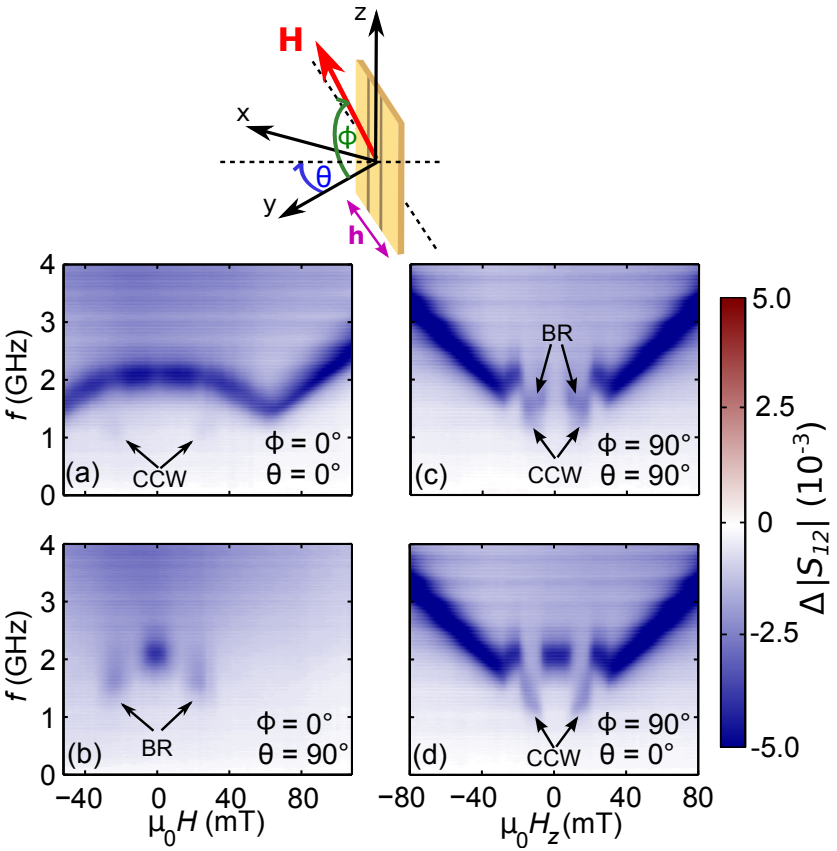

Figure 5.8: Color-coded absorption resonance data for different nominal external field orientations (ϕ, θ) (see sketch). In (c), (d) we plot the applied field in z direction. Here, a remanent field of 28 mT is present along y. Modes assigned to the counter-clockwise (CCW) and breathing (BR) SkL modes are marked by arrows.

frequency and are more intense.
In Fig. 5.8 (c), we choose $\phi = \theta = 90°$, i.e. $\mathbf{H}$ is parallel to z

and perpendicular to $\mathbf{h}$. We observe the reappearance of several modes, which differ however from our results in Fig. 5.8 (a): the resonance is interrupted around $H_z = 0$ and two modes are resolved around 1.3 GHz and 1.6 GHz (arrows).

We now explain these observations. The signatures marked by arrows in Fig. 5.8 (a) correspond to the counterclockwise (CCW) gyrational SkL mode, in agreement with our measurements in Section 5.1 in terms of field range and eigenfrequency. The rest of the resonance is ascribed to the FP and conical resonance.

The features marked by arrows in Fig. 5.8 (b) correspond to the excitation of the breathing (BR) SkL mode, which lies at slightly higher frequency compared to the CCW mode. Since $\mathbf{H} \parallel \mathbf{h}$, we expect only this mode to be activated in the SkL phase. For the spin helix, no eigenmodes are predicted for this excitation geometry, where $\mathbf{h} \parallel \mathbf{Q} \parallel \mathbf{H}$. Onose *et al.* performed measurements with $\mathbf{h} \parallel \mathbf{Q} \parallel \mathbf{H} \parallel \langle 110 \rangle$ and reported similar observations. They detected a resonance only in the SkL field range, which they ascribed to the BR mode and resolved a resonance at $H = 0$ [Ono12]. The resonance at zero field is excited, because in Cu_2OSeO_3 $\mathbf{Q} \parallel \langle 100 \rangle$ due to crystal anisotropy [Ada12]. In our case, we applied $\mathbf{H}$ along a specific $\langle 100 \rangle$ axis and then reduced the field to zero. For $H < H_{c1}$, the helices are distributed such that $\mathbf{Q}$ points along the three equivalent $\langle 100 \rangle$ directions [Bel12]. This leads to the presence of several helices with $\mathbf{Q} \perp \mathbf{h}$ and hence the excitation of the resonance around $H = 0$ in Fig. 5.8 (b).

In Fig. 5.8 (c) we resolve the BR and CCW modes and the resonances of the spin helix at finite fields. Note that under this configuration with the nominal setting $\mathbf{H} \parallel z \perp \mathbf{h}$, we do not expect the excitation of the BR mode. However, the remanent field in the y-coil is strong enough to tilt the SkL and to provide a finite component of $\mathbf{h}$ pointing out of the SkL plane. Around $H_z = 0$, the remanent field orients the helix along $\mathbf{h}$, leading

to the configuration $\mathbf{h} \parallel \mathbf{Q}$, for which no helix eigenmodes are predicted.

In the absence of remanence, we expect the field configuration in Fig. 5.8 (d) to be equivalent to the configuration in Fig. 5.8 (c) due to the rotational symmetry of the experimental setup. However, in Fig. 5.8 (d) we resolve a prominent resonance around $H_z = 0$ and only the CCW mode around $\mu_0 H_z = \pm 15\,\mathrm{mT}$. At $H_z = 0$, the remanent field in the y-coil orients $\mathbf{Q}$ out of the CPW plane, so that $\mathbf{Q} \perp \mathbf{h}$, which leads to the excitation of the helical eigenmode. At $\mu_0 H_z = \pm 15\,\mathrm{mT}$, the superposition of the remanent field along y and the applied field along z leads to a tilting of the SkL plane so that $\mathbf{h}$ lies within the SkL plane and can couple only to the gyrational modes.

The above observations confirm our undestanding of the dynamics in the noncollinear spin phases of Cu_2OSeO_3 (Section 5.1), combined with the field distribution in the broad CPW presented in Section 2.2.1. In particular, based on our results in Fig. 5.8 (c), we confirm that the weak shoulder resolved in Fig. 5.1 (b) in the SkL phase and the resonances excited in the conical and FP phase of the same dataset are due to the presence of a finite in-plane field h_x arising from the overlap of the sample with the signal line of the CPW.

Note that in all the data presented in Fig. 5.8, we do not resolve the high-frequency clockwise SkL mode due to its weak spectral weight [Sch15].

5.4 Time-resolved dynamics

In this section we address the time-resolved dynamics in the spin helix phase using pulsed induced microwave magnetometry (PIMM) (see Section 2.4). To address each helix eigenmode separately, we make use of our findings in Section 5.1, i.e. we compare data obtained for the perpendicular (90°) and parallel (0°) sample placement on the broad CPW (the angle refers to the orientation between the long axis of the CPW and of the sample). We measured the bar-shaped samples **A** and **E** and used the broad and antenna CPW (see Fig. 2.13).
The different sample portion L (in mm) covering the CPW results in a different absolute signal amplitude for each placement. We take this into account by dividing the induced voltage $V(t)$ recorded at 0° and 90° by $L = 0.35\,\mathrm{mm}$ and $L = 1.9\,\mathrm{mm}$, respectively. In Fig. 5.9 (a) we show the corresponding data recorded at 5 K and 0 mT. We observe an oscillation up to 8 ns. The Fourier transform (FT) data (inset) reveal peaks at 5 GHz and 4 GHz for the 0° and 90° placements, respectively. We attribute the peaks to the $+Q$ and $-Q$ eigenmodes, respectively. We fit a single exponentially decaying function

$$V(t) = V_0 + e^{-(t-t_0)/\tau_+} \cdot \cos(2\pi f_+(t-t_0) + \phi_+) \qquad (5.4)$$

to the 0°-data (blue) and obtain a frequency of $f_+ = (4.96 \pm 0.03)\,\mathrm{GHz}$ and relaxation time $\tau_+ = (2.2 \pm 0.1)\,\mathrm{ns}$. V_0, t_0, ϕ_+ denote the voltage offset, the initial time and the initial phase, respectively. The subscript $+$ refers to the $+Q$ mode. We restrict the fitting algorithm to the region after the transient regime (red), in which a strong initial spike does not allow to perform the analysis based on Eq. (5.4) (see Section 2.4 for more details).
The data obtained with the sample perpendicular to the CPW

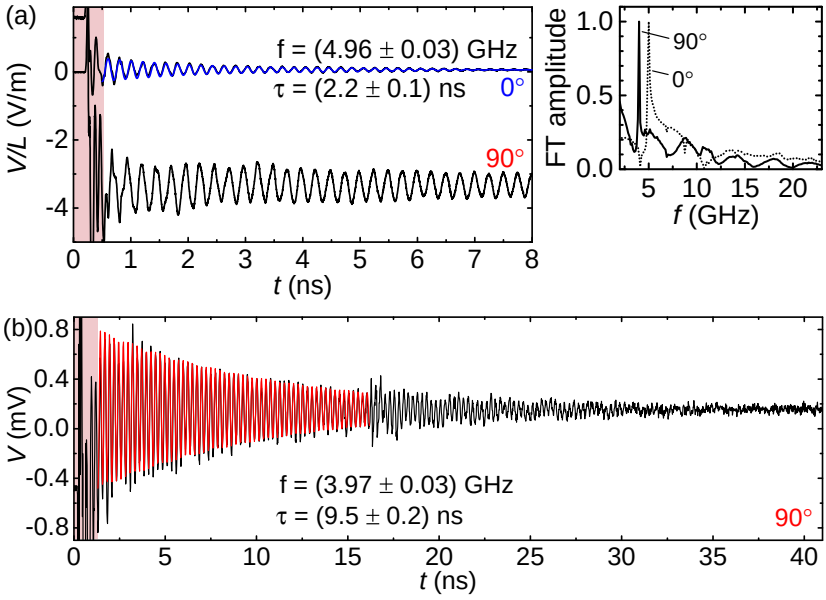

Figure 5.9: (a) Long-lasting oscillation measured in sample **E**, placed parallel (0°) and perpendicular (90°) to the broad CPW at 5 K and 0 mT. A fit curve is shown in blue. Inset: Fourier-transformed data revealing the corresponding resonance frequency. (b) Data of the 90°-placement recorded for a longer time interval. A fit curve is shown in red.

(90°) exhibit a significantly longer relaxation time and a narrower FT peak (inset) compared to 0°. To investigate this in detail, we measured the dynamics for a longer time interval. This is shown in Fig. 5.9 (b). We observe a ringing for several tens of ns with a pronounced feature at $t = 16$ ns. The latter is present both in the reference and subsequently recorded waveforms. The microwave pulse takes 8 ns to travel from one port of the DSA to the magnetic specimen. We attribute the feature in our data to the second excitation of the spin system by the

reflected pulse at port 1 of the DSA. After applying a fit (red) to the data for $t < 16\,\text{ns}$, we obtain $f_- = (3.97 \pm 0.03)\,\text{GHz}$ and $\tau_- = (9.5 \pm 0.2)\,\text{ns}$ for the $-Q$ eigenmode. f_- agrees with the FT data in the inset.

In Fig. 5.10 (a), (b), we extend the comparison among the two sample placements for different fields within the conical phase at 5 K. To show the full dataset, we replot the data for 0° of

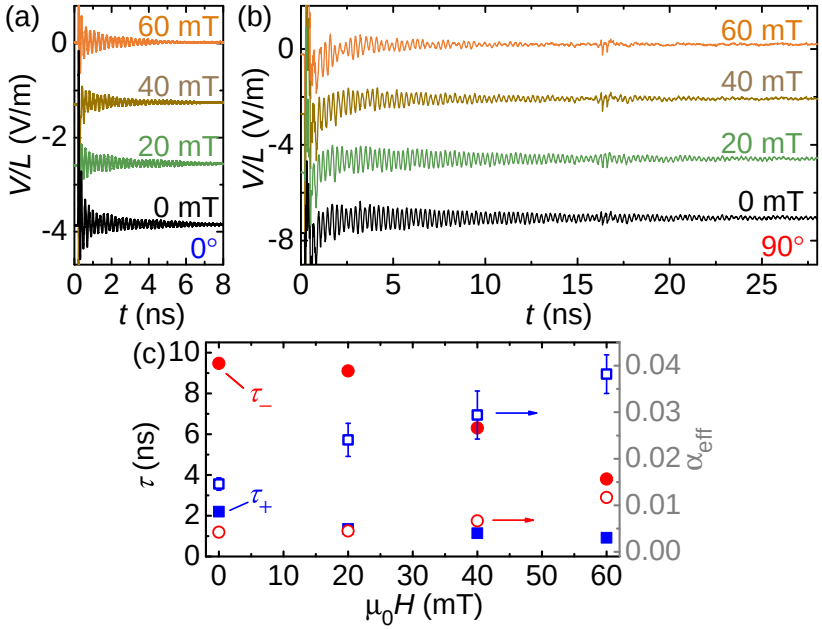

Figure 5.10: Data obtained in sample **E** placed (a) parallel (0°) and (b) perpendicularly (90°) on the broad CPW at 5 K and different fields. (c) Extracted relaxation time τ (filled symbols) and effective damping parameter α_{eff} (open symbols). Blue squares and red circles correspond to 0° and 90°, respectively.

Fig. 5.9 (a) and for 90° of Fig. 5.9 (b) in Fig. 5.10 (a) and Fig. 5.10 (b), respectively. The data for 90° in Fig. 5.10 (b) contain a

slowly varying nonlinear background signal that levels off above $t \approx 3\,\mathrm{ns}$. As outlined in Section 2.4, the data shown here result from the subtraction of two step pulse signals of relatively large amplitude (250 mV). For $0\,\mathrm{ns} < t < 3\,\mathrm{ns}$, the magnetically induced signal is superimposed on the step slope of the pulse, hence small field-dependent drifts (e.g. of the microwave tips) induce the above-mentioned background.

In Fig. 5.10 (c) we show the manually extracted relaxation times for each mode. We see that τ_- (filled red circles) is systematically larger (up to four times) compared to τ_+ (filled blue squares) at the same field.

We apply a FT on the data of Fig. 5.10 (a), (b) to obtain the resonance frequency and determine the effective Gilbert damping parameter α_{eff} according to Eq. (1.35). The results are shown in Fig. 5.10 (c) (open symbols) for both sample placements.

The field evolution of the waveforms in Fig. 5.10 (a), (b) differ significantly. In Fig. 5.10 (a), the decay is characterized by a single characteristic oscillation, whereas in Fig. 5.10 (b) for $\mu_0 H = 60\,\mathrm{mT}$, a beating pattern is resolved. This is because the $+Q$ mode gains spectral weight with increasing field (see Section 5.1) and is excited simultaneously with the $-Q$ mode.

In the aim of obtaining a more pronounced beating and studying this phenomenon in more detail, we need to optimize the measuring parameters. On the one hand, there is an optimum external field value, at which the eigenfrequencies of the conical modes have similar spectral weight. On the other hand, the absolute splitting (in GHz) among the conical eigenfrequencies scales with the critical field H_{c2}, as shown in Fig. 1.11. With increasing temperature, $H_{c2}(T)$ decreases (Fig. 1.7) and hence the frequency splitting is reduced. Finally, the induced signal strength in our CPWs decreases with increasing temperature. Considering all the above issues, we recorded data at 20 K and 70 mT on sample **A** placed perpendicularly on the broad CPW

(Fig. 5.11). We observe a pronounced beating pattern in $V(t)$ and

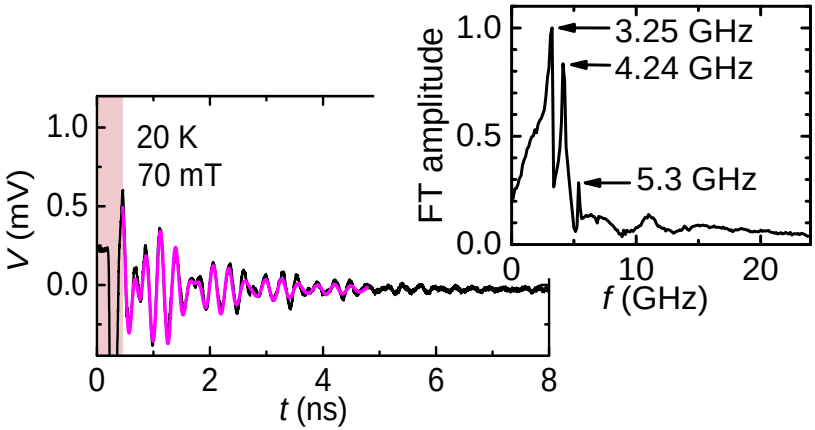

Figure 5.11: Sample **A** measured at 20 K and 70 mT placed perpendicularly on the broad CPW. The fit (magenta) is in agreement with the resonance frequency of the prominent $\pm Q$ modes resolved in the FT data.

peaks of almost equal height in the FT data (inset). The spike at 5.3 GHz corresponds to a spurious resonance due to connector mismatch, identified also in the VNA-SWS data in Fig. 5.12.
We fit the sum of two exponentially decaying functions

$$V(t) = V_0 + e^{-(t-t_0)/\tau_+} \cdot \cos(2\pi f_+(t-t_0) + \phi_+) + e^{-(t-t_0)/\tau_-} \cdot \cos(2\pi f_-(t-t_0) + \phi_-) \tag{5.5}$$

(magenta line in Fig. 5.11) restricted to the region after the transient regime (red) and within the time range, where the oscillation is clearly resolved. We get frequencies $f_+ = (4.22 \pm 0.02)$ GHz and $f_- = (3.23 \pm 0.03)$ GHz, in agreement with the FT data (inset). The fitted relaxation times read $\tau_+ = (0.90 \pm 0.03)$ ns and $\tau_- = (1.5 \pm 0.1)$ ns.
Interestingly, the FT data in the inset of Fig. 5.9 suggest the pres-

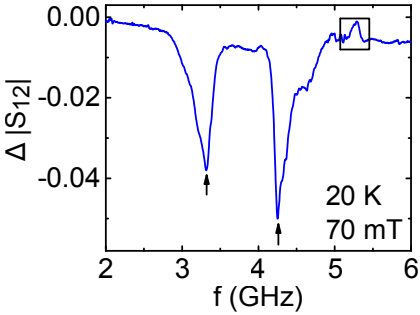

Figure 5.12: VNA-SWS spectrum recorded at 20 K and 70 mT with sample **A** placed perpendicularly on the broad CPW. Arrows and square mark the resonances of the $\pm$Q modes at 3.31 GHz and 4.25 GHz and the spurious resonance at $\approx$ 5.3 GHz, respectively.

ence of higher-frequency oscillations above the main mode. On the one hand, domains ringing at a slightly different resonance frequency due to e.g. varying cubic anisotropy might contribute to this observation. On the other hand, the nonuniform excitation provided by the CPW (see Fig. 2.8) might play a role, leading to the generation of spin waves with finite k vector in the magnetostatic regime [GM96]. To examine the latter hypothesis, we place sample **E** perpendicularly on the antenna CPW [Fig. 2.13 (b)]. In Fig. 5.13, we observe a short relaxation time $\tau_- = (0.29 \pm 0.01)$ ns at 0 mT and 5 K, i.e. approximately 30 times less compared to Fig. 5.10 (b). The corresponding resonance curve measured by VNA-SWS (inset) is remarkably broad and shows a clear deviation from a Lorentzian lineshape (green line).

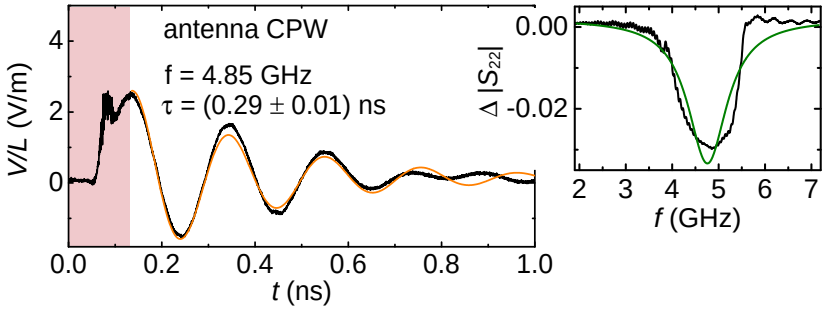

Figure 5.13: Data recorded with sample **E** placed perpedicularly on the antenna CPW at 0 mT and 5 K. A single exponential decay fit (orange) yields $\tau_- = (0.29 \pm 0.01)$ ns. The inset shows the corresponding VNA-SWS data, and a Lorentzian lineshape (green line) for comparison.

Discussion

The lowest effective damping parameter estimated for the spin helix amounts to 0.004 [Fig. 5.10 (c)]. We believe this value to be an upper limit for the intrinsic Gilbert damping α_{intr}, because of extrinsic damping contribution by the inhomogeneous excitation field of the CPW. This hypothesis is supported by the fast decay obtained with the antenna CPW, which generates a significantly broader distribution of wavevectors k transferred to the sample compared to the broad CPW (see Section 2.2.2). We explain the fast decay in the measurements with the antenna CPW, in that the excited spin waves dephase and cancel the overall induced voltage signal. Note that we did not observe a significant change in τ as a function of temperature while using the antenna CPW. This suggests that dephasing of the spin ensemble is the dominant extrinsic damping mechanism present under an inhomogeneous excitation.
In their study on optically-excited, time-resolved dynamics in

Cu_2OSeO_3, Ogawa *et al.* measured waveforms with beating patterns [OST15]. The authors performed a Fourier analysis of their data to study the dynamics of each conical eigenmode. In the framework of this thesis, we have shown how to separately address the $\pm Q$ modes. By this means, we found that the $-Q$ mode exhibits a long-lasting oscillation with $\tau_- = (9.5 \pm 0.2)\,\mathrm{ns}$ at 5 K and 0 mT. This is about a factor of four larger than τ_+. Ogawa *et al.* reported $\tau_- \approx 6\,\tau_+$ at 40 K [OST15]. Our value $\tau_- = (9.5 \pm 0.2)\,\mathrm{ns}$ at 5 K is the largest reported so far for Cu_2OSeO_3. For comparison, we note that typical values for the relaxation time τ of $Ni_{81}Fe_{19}$ and YIG lie in the 1-3 ns and ms range, respectively [Koro4; Sil99; SL60].

In this work, we estimated the effective damping parameter based on the relaxation times via Eq. (1.35). This approach is based on the phenomenological framework of Gilbert damping [Sta93], where it is assumed that all the relevant damping mechanisms are well-described by a single damping parameter α_{intr}. As a first step towards understanding the difference between τ_+ and τ_-, we propose to include the Gilbert damping in the theoretical description of the dynamics in chiral magnets as a small perturbation and draw a comparison to our experimental findings. At the microscopic level, the relaxation of the dynamic magnetization into the thermal bath (phonons) is usually considered as the main contribution to the Gilbert damping. However, scattering within the magnetic subsystem, i.e. interactions between magnons (magnon-magnon scattering) or between magnons and impurities may also take place in general [Leno6]. In case the spin helix relaxation process is dominated by such contributions, one needs to go beyond the phenomenological approach of Gilbert damping. In particular, the question arises whether the difference in the relaxation times of the $\pm Q$ modes is related to their linear polarization or handedness of precession (see Section 5.1). For example, the decay of

the $-Q$ mode into a spin wave with finite wave vector might take place at a lower rate compared to the $+Q$, because of conservation of the sense of precession. In order to summarize the contribution of different effects to the overall relaxation time τ_{tot} measured in experiments, we suggest the use of Matthiessen's ansatz [Dav98]

$$\frac{1}{\tau_{tot}} = \frac{1}{\tau_{ph}} + \frac{1}{\tau_{mm}} + ... \tag{5.6}$$

as a first approximation. Here, τ_{ph} and τ_{mm} describe the contribution from individual scattering processes (magnon-phonon, magnon-magnon and others). Note that this approach is valid only if individual scattering processes do not interfere with each other.

Finally, we also performed TDT measurements in the antenna CPW setup [Fig. 2.13 (b)], but did not observe a ringing in $V(t)$ that would indicate travelling spin waves in the noncollinear spin phases of Cu_2OSeO_3. The 3 µm grain size of the silicon carbide paper used to polish our samples is large compared to the decay length of the dynamic field amplitude above the antenna (see Fig. 2.7). Hence, we attribute the absence of the indication of travelling spin waves to the weak coupling among our mechanically polished sample and the antennae.

6 Summary and Outlook

In the framework of this thesis we measured the spin dynamics in bar-shaped specimens of Cu_2OSeO_3 using vector network analyzer-based spin wave spectroscopy (VNA-SWS). Hereby, we showed that the average dynamic magnetization is linearly polarized at an unexpectedly small frequency of about 2 GHz and zero magnetic field. This results in linear dichroism, the phenomenon of polarization-dependent absorption of electromagnetic waves. While this effect is routinely exploited in applications as diverse as structure determination of DNA molecules or polarization filters in optical technologies, it was not observed in magnetic excitations in the few GHz frequency regime for more than eight decades. Unlike optical filters, we found that tiny variations of the bulk sample shape allow one to switch the polarization plane of a given mode by 90°.

We developed a sample holder with GHz cables that allowed us to study magnetic resonances in a 2D vector magnet. Combining measurements with this apparatus and detailed simulations of the high-frequency properties of our optimized coplanar waveguides (CPWs), we have shown how to deliberately address resonance modes of distinct symmetry in the Skyrmion lattice (SkL) phase.

We addressed the Gilbert damping in Cu_2OSeO_3. In the field-polarized phase we used two different optimized CPWs and extracted $\alpha_{\mathrm{intr}} \approx 1 \times 10^{-4}$ at 5 K. This value is only three times

higher than the best value known in yttrium-iron-garnet (YIG). The numerous sharp resonances resolved in our spectra were attributed to modes that are spatially confined across the macroscopic sample and allowed for by the low damping.
The dynamics in the spin helix phase was additionally explored by time-resolved pulsed induced microwave magnetometry (PIMM). Based on our results regarding the polarization of the spin helix eigenmodes, we addressed the dynamics of the $+Q$ and $-Q$ mode individually. We found that the relaxation time $\tau_- \approx 10\,\mathrm{ns}$ of the latter is four times larger than τ_+ at $5\,\mathrm{K}$ and $0\,\mathrm{mT}$, which might be related to the handedness of the modes. Using two different CPWs, we modified the wavevectors that are transferred to the sample and observed a variation of τ_- by approximately a factor of 30 at $5\,\mathrm{K}$ and zero field. We attribute this finding to the dephasing of the spin wave ensemble excited by the CPW.

Considering the results of our study, insulating chiral magnets turn out to be promising candidates when exploring complex chiral spin structures for high-frequency applications. On the one hand, the small damping in Cu_2OSeO_3 highlights the relevance of insulating chiral magnets for future applications in magnonics and spintronics. On the other hand, our findings on the linear dichroism shed a new light on magnetization dynamics in that spin helices induced by Dzyaloshinskii-Moriya interaction (DMI) offer strict linear polarization for a broad spectrum of sample and environmental parameters. This opens up an unexpected perspective for the polarization control of microwaves in frequency regimes that are key for modern telecommunication networks, especially once room-temperature insulating chiral magnets are realized. For example, a conventional linear polarizer for free-space GHz radiation consists of a large grid prepared from macroscopic metallic rods mounted

on a large frame. Contrastingly, our results offer a field-tunable magnetic polarizer based on a compact material. Magnon-photon cavities is a future technology where DMI-induced linear dichroism offers novel, exciting perspectives for microwave control with integrated magnetic components by boosting the coupling between photons and magnons [Gor14; Hue13; Tab14; Zha14].

The relatively long relaxation time τ of the spin helix is promising regarding the investigation of spin wave propagation in the noncollinear spin phases of chiral magnets. Seki *et al.* resolved signals of travelling spin waves between two coplanar antennae in the field-polarized phase of a bulk Cu_2OSeO_3 sample [Sek16]. We propose using meander-shaped antennae, ideally integrated on top of chiral magnet thin films by evaporation, to perform spin wave transmission studies. This type of antennae is characterized by a narrow distribution of the wave vectors transferred to the sample [VB10], which might be decisive to minimize dephasing of the excited spin waves and thus resolve the corresponding signals. The use of integrated antennae on thin films will improve the inductive coupling between the microwave and the spins in the sample.

Finally, the sample rod designed in the framework of this thesis combined with the 2D vector magnet is a valuable tool for future studies. For example, in thin films of chiral magnets [HC12; Kar10; Li13; Men13; PCM12; PGM14; Wil13; Yok14; Zan11], the exact orientation of the SkL plane relative to the film plane has been controversially discussed in the litterature (see Ref. [Wie14] and references therein). We expect the SkL eigenmodes in thin films to exhibit characteristic features similar to the ones known from bulk specimens. By applying the magnetic field along specific directions relative to the film plane and monitoring the excitation of modes with different

symmetry (gyrational versus breathing), one may determine the orientation of the SkL.

A List of samples

The following table gives an overview of the samples used in this work. The first column shows the identifier used throughout this thesis and the crystallite identification where this sample was cut from. The components of the demagnetization tensor N_i were estimated according to Ref. [Aha98] based on the sample dimensions. The sketches illustrate the crystallographic orientation of the samples.

Name Sample ID Crystallite ID	Dimensions $x \times y \times z$ (mm)	Demag- netization factors	
A SW_011 VTG-1-10	$2.24 \times 0.38 \times 0.28$	$N_x = 0.07$ $N_y = 0.40$ $N_z = 0.53$	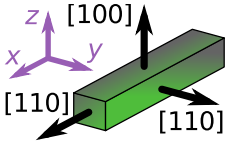
B SW_012 VTG-1-9	$2.36 \times 0.39 \times 0.29$	$N_x = 0.07$ $N_y = 0.40$ $N_z = 0.53$	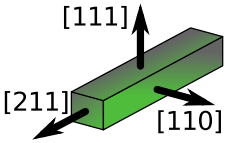
C VTG-1-11 VTG-1-11	$3 \times 0.49 \times 0.47$	$N_x = 0.07$ $N_y = 0.46$ $N_z = 0.47$	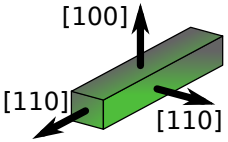
D SW_002 VTG-1-10	$2.40 \times 0.46 \times 0.34$	$N_x = 0.07$ $N_y = 0.40$ $N_z = 0.53$	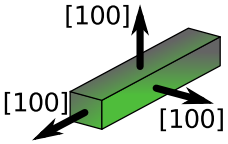
E VTG-1-10 VTG-1-10	$1.9 \times 0.35 \times 0.17$	$N_x = 0.06$ $N_y = 0.32$ $N_z = 0.62$	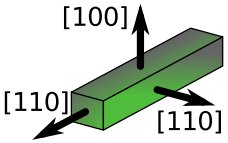

B CPW dimensions

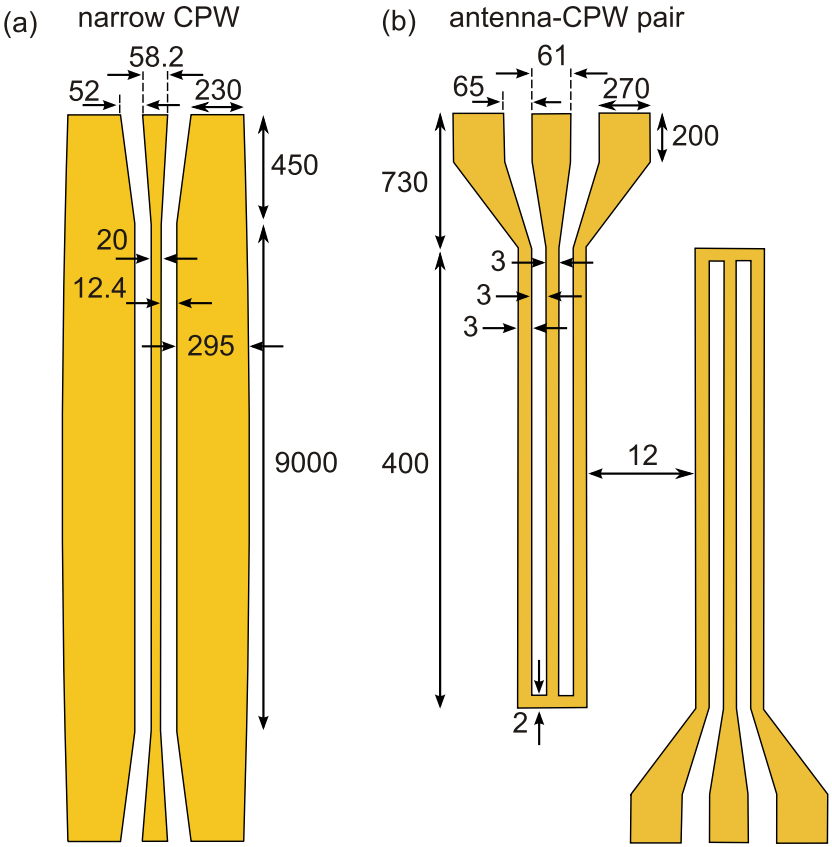

Figure B.1: Detailed design parameters of the lithographically fabricated CPWs used in this work. Not to scale; all dimensions in μm. The metallic leads are composed out of 4.5 nm Cr / 120 nm Au.

C Simulation parameters

For the implementation of the CPW layout in the software *CST Microwave Studio*, we followed the approach of Ref. [WTM08] and considered the suggestions available in the software documentation (user help files). In particular, appropriate port size is a crucial factor for obtaining accurate results and avoid spurious electromagnetic modes in the simulation.
A bounding box with the condition $E = 0$ and background with surrounding space distance of 1 mm in all directions was placed around the model. All material components were modelled as real, lossy conductors and were imported from the software library. We used the frequency solver.
A lot of care was invested in optimizing the 3D tetrahedral legacy-type mesh. We aimed for the presence of a minimum of three cells in the crossection of each current lead of the CPW. This was achieved by explicitely defining local mesh properties for each conductor plate. Mesh cells with sharp edges may arise from a coarse mesh and cause errors. Therefore, the aspect ratio of the tetrahedrons was verified visually by means of cross-sections of the model.
To keep the number of cells low and accelerate the simulation, the substrate thickness of the broad CPW was reduced compared to the real structure. The minimum thickness is given by the penetration depth of the electromagnetic fields and was determined iteratively. In the case of the antenna-CPW pair, a

"mini-substrate" of about 1/10 of the entire substrate size is implemented as an alcove inside the larger GaAs substrate, around the CPW. This part serves as a transition element between the coarse substrate and fine CPW mesh.
A detailed list of the mesh parameters used are summarized in Table C.1. Simulation time is based on a 8-processor[1] *DELL*

parameter \ CPW	narrow	broad	antenna
approx. number of cells	415,000	657,000	1,500,000
approx. simulation time (h)	48	72	72
steps/wavelength (global)	20	10	12
min. step number (global)	20	20	20
max. step width (G)	100	350	7
max. step width (S)	20	350	7
max. step width (substrate)	0	0	0
max. step width (mini-substrate)	—	—	60

Table C.1: Mesh parameters for modelling the electromagnetic response of the CPWs used in this work. Global and local mesh settings are given. G, S denote ground and signal lines, respectively.

server with 24 GB physical memory (RAM). Typical memory allocation during simulation was as high as 18 GB. Note that memory, rather than processor power is decisive for fast and large simulations.

1 Intel Xeon X5450.

Bibliography

[Ada12] T. Adams, A. Chacon, M. Wagner, A. Bauer, G. Brandl, B. Pedersen, H. Berger, P. Lemmens and C. Pfleiderer, *Long-Wavelength Helimagnetic Order and Skyrmion Lattice Phase in* Cu_2OSeO_3, Phys. Rev. Lett. **108**, 237204, (2012).

[Aha98] A. Aharoni, *Demagnetizing factors for rectangular ferromagnetic prisms*, J. Appl. Phys. **83**, 3432, (1998).

[AM76] N. Ashcroft and D. Mermin, *Solid State Physics*. Harcourt College Publishers, Orlando, (1976).

[An13] T. An, V. I. Vasyuchka, K. Uchida, A. V. Chumak, K. Yamaguchi, K. Harii, J. Ohe, M. B. Jungfleisch, Y. Kajiwara, H. Adachi, B. Hillebrands, S. Maekawa and E. Saitoh, *Unidirectional spin-wave heat conveyer*, Nat. Mater. **12**, 549, (2013).

[Bar86] W. Barry, *A Broad-Band, Automated, Stripline Technique for the Simultaneous Measurement of Complex Permittivity and Permeability*, IEEE Trans. Microw. Theory Techn. **34**, 80, (1986).

[Bau14] A. Bauer, *Investigation of itinerant antiferromagnets and cubic chiral helimagnets*. PhD thesis, Technische Universität München, (2014).

[Bel10] M. Belesi, I. Rousochatzakis, H. C. Wu, H. Berger, I. V. Shvets, F. Mila and J. P. Ansermet, *Ferrimagnetism of the magnetoelectric compound Cu_2OSeO_3 probed by ^{77}Se NMR*, Phys. Rev. B **82**, 094422, (2010).

[Bel12] M. Belesi, I. Rousochatzakis, M. Abid, U. K. Rößler, H. Berger and J.-P. Ansermet, *Magnetoelectric effects in single crystals of the cubic ferrimagnetic helimagnet Cu_2OSeO_3*, Phys. Rev. B **85**, 224413, (2012).

[BF13] S. Buhrandt and L. Fritz, *Skyrmion lattice phase in three-dimensional chiral magnets from Monte Carlo simulations*, Phys. Rev. B **88**, 195137, (2013).

[BGP13] A. Bauer, M. Garst and C. Pfleiderer, *Specific Heat of the Skyrmion Lattice Phase and Field-Induced Tricritical Point in MnSi*, Phys. Rev. Lett. **110**, 177207, (2013).

[Bil07] C. Bilzer, *Microwave susceptibility of thin ferromagnetic films: metrology and insight into magnetization dynamics*. PhD thesis, Université Paris Sud-Paris XI, (2007).

[BJ80] P. Bak and M. H. Jensen, *Theory of helical magnetic structures and phase transitions in MnSi and FeGe*, J. Phys. C: Solid State **13**, L881, (1980).

[Bou16] O. Boulle, J. Vogel, H. Yang, S. Pizzini, D. de Souza Chaves, A. Locatelli, T. O. Menteş, A. Sala, L. D. Buda-Prejbeanu, O. Klein, M. Belmeguenai, Y. Roussigné, A. Stashkevich, S. M. Chérif, L. Aballe, M. Foerster, M. Chshiev, S. Auffret, I. M. Miron and G. Gaudin, *Room-temperature chiral magnetic skyrmions in ultrathin magnetic nanostructures*, Nat. Nanotech. **11**, 449, (2016).

[BR01] A. N. Bogdanov and U. K. Rößler, *Chiral Symmetry Breaking in Magnetic Thin Films and Multilayers*, Phys. Rev. Lett. **87**, 037203, (2001).

[But15] F. Buttner, C. Moutafis, M. Schneider, B. Kruger, C. M. Gunther, J. Geilhufe, C. v. K. Schmising, J. Mohanty, B. Pfau, S. Schaffert, A. Bisig, M. Foerster, T. Schulz, C. A. F. Vaz, J. H. Franken, H. J. M. Swagten, M. Klaui and S. Eisebitt, *Dynamics and inertia of skyrmionic spin structures*, Nat. Phys. **11**, 225, (2015).

[CDL86] C. Cohen-Tannoudji, B. Diu and F. Laloë, *Mécanique Quantique Tome II*. Hermann Éditeurs des Sciences et des Arts, Paris, (1986).

[Chu15] A. V. Chumak, V. I. Vasyuchka, A. A. Serga and B. Hillebrands, *Magnon spintronics*, Nat. Phys. **11**, 453, (2015).

[CL98] A. Crépieux and C. Lacroix, *Dzyaloshinsky–Moriya interactions induced by symmetry breaking at a surface*, J. Magn. Magn. Mater. **182**, 341, (1998).

[Dav98] J. H. Davies, *The Physics of Low-dimensional Semiconductors: An Introduction*. Cambridge University Press, Cambridge, (1998).

[dKel13] O. d'Allivy Kelly, A. Anane, R. Bernard, J. Ben Youssef, C. Hahn, A. H. Molpeceres, C. Carrétéro, E. Jacquet, C. Deranlot, P. Bortolotti, R. Lebourgeois, J.-C. Mage, G. de Loubens, O. Klein, V. Cros and A. Fert, *Inverse spin Hall effect in nanometer-thick yttrium iron garnet/Pt system*, Appl. Phys. Lett. **103**, 082408, (2013).

[DS06] J. Detlefsen and U. Siart, *Grundlagen der Hochfrequenztechnik*. Oldenburg Verlag, München-Wien, (2006).

[Dun57] B. J. Duncan, L. Swern, K. Tomiyasu and J. Hannwacker, *Design Considerations for Broad-Band Ferrite Coaxial Line Isolators*, Proc. IRE **45**, 483, (1957).

[Dzy58] I. Dzyaloshinsky, *A thermodynamic theory of weak ferromagnetism of antiferromagnetics*, J. Phys. Chem. Solids **4**, 241, (1958).

[ElG11] M. El-Gibari, D. Averty, C. Lupi, Y. Mahé Hongwu Li and S. Toutain, *Ultra Wideband Communications: Novel Trends - Antennas and Propagation*. InTech, (2011).

[EP86] H. Effenberger and F. Pertlik, *The crystal structures of the copper(II)-oxo-selenites Cu2O(SeO3) (cubic and monoclinic), and Cu4O(SeO3)3 (monoclinic and triclinic)*, Chemical Monthly **117**, 887, (1986).

[Eve12] K. Everschor, *Current-Induced Dynamics of Chiral Magnetic Structures*. PhD thesis, University of Cologne, (2012).

[FCS13] A. Fert, V. Cros and J. Sampaio, *Skyrmions on the track*, Nat. Nanotech. **8**, 152, (2013).

[Fei11] P. Fei, Y.-C. Jiao, Y. Ding and F.-S. Zhang, *A compact coplanar waveguide fed wide tapered slot ultra-wideband antenna*, PIER Letters **25**, 77, (2011).

[FSW13] M. Farle, T. Silva and G. Woltersdorf, *Magnetic Nanostructures: Spin Dynamics and Spin Transport*. Springer, Berlin, Heidelberg, (2013).

[FZ13] M. Farle and H. Zabel, *Magnetic Nanostructures Spin Dynamics and Spin Transport*. Springer Tracts in Modern Physics, Heidelberg, (2013).

[GC57] S. Geschwind and A. M. Clogston, *Narrowing Effect of Dipole Forces on Inhomogeneously Broadened Lines*, Phys. Rev. **108**, 49, (1957).

[GC87] G. Ghione and C. U. Naldi, *Coplanar Waveguides for MMIC Applications: Effect of Upper Shielding, Conductor Backing, Finite-Extent Ground Planes, and Line-to-Line Coupling*, IEEE Trans. Microw. Theory Techn. **35**, 260, (1987).

[GGB79] K. C. Gupta, R. Garg and I. J. Bahl, *Microstrip Lines and Slotlines*. Artech House, London, (1979).

[GGB96] K. C. Gupta, R. Garg and P. Bhartia, *Microstrip Lines and Slotlines*. Artech House, London, (1996).

[Gie05] F. Giesen, *Magnetization Dynamics of Nanostructured Ferromagnetic Rings and Rectangular Elements*. PhD thesis, University of Hamburg, (2005).

[Gil04] T. Gilbert, *A Phenomenological Theory of Damping in Ferromagnetic Materials*, IEEE Trans. Magn. **40**, 3443, (2004).

[GM96] A. G. Gurevich and G. A. Melkov, *Magnetization Oscillations and Waves*. CRC Press, Boca Raton, (1996).

[Gne10] V. P. Gnezdilov, K. V. Lamonova, Y. G. Pashkevich, P. Lemmens, H. Berger, F. Bussy and S. L. Gnatchenko, *Magnetoelectricity in the ferrimagnetic Cu_2OSeO_3: symmetry analysis and Raman scattering study*, Low Temp. Phys. **36**, 550, (2010).

[Gor14] M. Goryachev, W. G. Farr, D. L. Creedon, Y. Fan, M. Kostylev and M. E. Tobar, *High-Cooperativity Cavity QED with Magnons at Microwave Frequencies*, Phys. Rev. Appl. **2**, 054002, (2014).

[Grü08] P. A. Grünberg, *Nobel Lecture: From spin waves to giant magnetoresistance and beyond*, Rev. Mod. Phys. **80**, 1531, (2008).

[HC12] S. X. Huang and C. L. Chien, *Extended Skyrmion Phase in Epitaxial* FeGe(111) *Thin Films*, Phys. Rev. Lett. **108**, 267201, (2012).

[HCH85] B. Heinrich, J. F. Cochran and R. Hasegawa, *FMR linebroadening in metals due to twomagnon scattering*, J. Appl. Phys. **57**, 3690, (1985).

[Heu05] H. Heuermann, *Hochfrequenztechnik*. Vieweg, Berlin, (2005).

[HK51] C. Herring and C. Kittel, *On the Theory of Spin Waves in Ferromagnetic Media*, Phys. Rev. **81**, 869, (1951).

[HP98] M. J. Hurben and C. E. Patton, *Theory of two magnon scattering microwave relaxation and ferromagnetic resonance linewidth in magnetic thin films*, J. Appl. Phys. **83**, 4344, (1998).

[Hue13] H. Huebl, C. W. Zollitsch, J. Lotze, F. Hocke, M. Greifenstein, A. Marx, R. Gross and S. T. B. Goennenwein, *High Cooperativity in Coupled Microwave Resonator Ferrimagnetic Insulator Hybrids*, Phys. Rev. Lett. **111**, 127003, (2013).

[HUW02] B. Heinrich, R. Urban and G. Woltersdorf, *Magnetic relaxations in metallic multilayers*, IEEE Trans. Magn. **38**, 2496, (2002).

[Igu15] Y. Iguchi, S. Uemura, K. Ueno and Y. Onose, *Nonreciprocal magnon propagation in a noncentrosymmetric ferromagnet $LiFe_5O_8$*, Phys. Rev. B **92**, 184419, (2015).

[Jac62] J. D. Jackson, *Classical Electrodynamics*. John Wiley & Sons, New York, (1962).

[Jia15] W. Jiang, P. Upadhyaya, W. Zhang, G. Yu, M. B. Jungfleisch, F. Y. Fradin, J. E. Pearson, Y. Tserkovnyak, K. L. Wang, O. Heinonen, S. G. E. te Velthuis and A. Hoffmann, *Blowing magnetic skyrmion bubbles*, Science **349**, 283, (2015).

[Jon10] F. Jonietz, S. Mühlbauer, C. Pfleiderer, A. Neubauer, W. Münzer, A. Bauer, T. Adams, R. Georgii, P. Böni, R. A. Duine, K. Everschor, M. Garst and A. Rosch, *Spin Transfer Torques in MnSi at Ultralow Current Densities*, Science **330**, 1648, (2010).

[Kal06] S. S. Kalarickal, P. Krivosik, M. Wu, C. E. Patton, M. L. Schneider, P. Kabos, T. J. Silva and J. P. Nibarger, *Ferromagnetic resonance linewidth in metallic thin films: Comparison of measurement methods*, J. Appl. Phys. **99**, 093909, (2006).

[Kam11] T. Kampfrath, A. Sell, G. Klatt, A. Pashkin, S. Mahrlein, T. Dekorsy, M. Wolf, M. Fiebig, A. Leitenstorfer and R. Huber, *Coherent terahertz control of antiferromagnetic spin waves*, Nat. Photon. **5**, 31, (2011).

[Kan16] W. Kang, Y. Huang, C. Zheng, W. Lv, N. Lei, Y. Zhang, X. Zhang, Y. Zhou and W. Zhao, *Voltage*

Controlled Magnetic Skyrmion Motion for Racetrack Memory, Sci. Rep. **6**, 23164, (2016).

[Kar10] E. Karhu, S. Kahwaji, T. L. Monchesky, C. Parsons, M. D. Robertson and C. Maunders, *Structure and magnetic properties of MnSi epitaxial thin films*, Phys. Rev. B **82**, 184417, (2010).

[KCC05] B. Kuanr, R. E. Camley and Z. Celinski, *Narrowing of the frequency-linewidth in structured magnetic strips: Experiment and theory*, Appl. Phys. Lett. **87**, 012502, (2005).

[KDG10] V. V. Kruglyak, S. O. Demokritov and D. Grundler, *Magnonics*, J. Phys. D: Appl. Phys. **43**, 264001, (2010).

[KG14] M. Krawczyk and D. Grundler, *Review and prospects of magnonic crystalsand devices with reprogrammable band structure*, J. Phys.: Condens. Matter **26**, 123202, (2014).

[Kit47] C. Kittel, *Interpretation of Anomalous Larmor Frequencies in Ferromagnetic Resonance Experiment*, Phys. Rev. **71**, 270, (1947).

[Kit48] C. Kittel, *On the Theory of Ferromagnetic Resonance Absorption*, Phys. Rev. **73**, 155, (1948).

[Kit66] C. Kittel, *Introduction to Solid State Physics*. Wiley, New York, (1966).

[Kla04] S. N. Klausen, K. Lefmann, P.-A. Lindgård, L. T. Kuhn, C. R. H. Bahl, C. Frandsen, S. Mørup, B. Roessli, N. Cavadini and C. Niedermayer, *Magnetic anisotropy and quantized spin waves in hematite nanoparticles*, Phys. Rev. B **70**, 214411, (2004).

[Kob10] M. I. Kobets, K. G. Dergachev, E. N. Khatsko, A. I. Rykova, P. Lemmens, D. Wulferding and H. Berger, *Microwave absorption in the frustrated ferrimagnet Cu2OSeO3*, Low Temperature Physics **36**, 176, (2010).

[Koro4] T. Korn, *Zeitaufgelöste Magnetisierungsmessungen an ferromagnetischen Filmen und Mikrostrukturen*. Cuvillier Verlag, Göttingen, (2004).

[Leno6] K. Lenz, H. Wende, W. Kuch, K. Baberschke, K. Nagy and A. Jánossy, *Two-magnon scattering and viscous Gilbert damping in ultrathin ferromagnets*, Phys. Rev. B **73**, 144424, (2006).

[Li13] Y. Li, N. Kanazawa, X. Z. Yu, A. Tsukazaki, M. Kawasaki, M. Ichikawa, X. F. Jin, F. Kagawa and Y. Tokura, *Robust Formation of Skyrmions and Topological Hall Effect Anomaly in Epitaxial Thin Films of MnSi*, Phys. Rev. Lett. **110**, 117202, (2013).

[LL35] L. Landau and E. Lifshitz, *On the Theory of the Dispersion of Magnetic Permeability in Ferromagnetic Bodies*, Physikalische Zeitschrift der Sowjetunion **8**, 153–169, (1935).

[Mai12] A. Maisuradze, A. Shengelaya, H. Berger, D. M. Djoki ć and H. Keller, *Magnetoelectric Coupling in Single Crystal* Cu_2OSeO_3 *Studied by a Novel Electron Spin Resonance Technique*, Phys. Rev. Lett. **108**, 247211, (2012).

[Men13] D. Menzel, J. Engelke, T. Reimann and S. Süllow, *Enhanced critical fields in MnSi thin films*, J. Korean Phys. Soc. **62**, 1580, (2013).

[Mil13] P. Milde, D. Köhler, J. Seidel, L. M. Eng, A. Bauer, A. Chacon, J. Kindervater, S. Mühlbauer, C. Pfleiderer, S. Buhrandt, C. Schütte and A. Rosch, *Unwinding of a Skyrmion Lattice by Magnetic Monopoles*, Science **340**, 1076–1080, (2013).

[Moc12] M. Mochizuki, *Spin-Wave Modes and Their Intense Excitation Effects in Skyrmion Crystals*, Phys. Rev. Lett. **108**, 017601, (2012).

[Moc15] M. Mochizuki, *Microwave Magnetochiral Effect in* Cu_2OSeO_3, Phys. Rev. Lett. **114**, 197203, (2015).

[Mor16] C. Moreau-Luchaire, C. Moutafis, N. Reyren, J. Sampaio, C. A. F. Vaz, N. Van Horne, K. Bouzehouane, K. Garcia, C. Deranlot, P. Warnicke, P. Wohlhüter, J.-M. George, M. Weigand, J. Raabe, V. Cros and A. Fert, *Additive interfacial chiral interaction in multilayers for stabilization of small individual skyrmions at room temperature*, Nat. Nanotech. **11**, 444, (2016).

[Mor60] T. Moriya, *New Mechanism of Anisotropic Superexchange Interaction*, Phys. Rev. Lett. **4**, 228, (1960).

[Mot05] V. S. Mottonen, *Wideband coplanar waveguide-to-rectangular waveguide transition using fin-line taper*, IEEE Microwave and Wireless Components Letters **15**, 119, (2005).

[Müh09] S. Mühlbauer, B. Binz, F. Jonietz, C. Pfleiderer, A. Rosch, A. Neubauer, R. Georgii and P. Böni, *Skyrmion Lattice in a Chiral Magnet*, Science **323**, 915, (2009).

[MW15] M. Mochizuki and Y. Watanabe, *Writing a skyrmion on multiferroic materials*, Appl. Phys. Lett. **107**, 082409, (2015).

[Nak80] O. Nakanishi, A. Yanase, A. Hasegawa and M. Kataoka, *The origin of the helical spin density wave in MnSi*, Solid State Communications **35**, 995, (1980).

[Naz03] A. V. Nazarov, D. Ménard, J. J. Green, C. E. Patton, G. M. Argentina and H. J. Van Hook, *Near theoretical microwave loss in hot isostatic pressed (hipped) polycrystalline yttrium iron garnet*, J. Appl. Phys. **94**, 7227, (2003).

[Neu09] A. Neubauer, C. Pfleiderer, B. Binz, A. Rosch, R. Ritz, P. G. Niklowitz and P. Böni, *Topological Hall Effect in the A Phase of MnSi*, Phys. Rev. Lett. **102**, 186602, (2009).

[NT13] N. Nagaosa and Y. Tokura, *Topological properties and dynamics of magnetic skyrmions*, Nat. Nanotech. **8**, 899, (2013).

[OHa00] R. C. O'Handley, *Modern Magnetic Materials, Priciples and Applications*. Wiley, New York, (2000).

[Oka13] Y. Okamura, F. Kagawa, M. Mochizuki, M. Kubota, S. Seki, S. Ishiwata, M. Kawasaki, Y. Onose and Y. Tokura, *Microwave magnetoelectric effect via skyrmion resonance modes in a helimagnetic multiferroic*, Nat. Commun. **4**, 2391, (2013).

[Oka15] Y. Okamura, F. Kagawa, S. Seki, M. Kubota, M. Kawasaki and Y. Tokura, *Microwave Magnetochiral Dichroism in the Chiral-Lattice Magnet* Cu_2OSeO_3, Phys. Rev. Lett. **114**, 197202, (2015).

[Ono12] Y. Onose, Y. Okamura, S. Seki, S. Ishiwata and Y. Tokura, *Observation of Magnetic Excitations of Skyrmion Crystal in a Helimagnetic Insulator Cu_2OSeO_3*, Phys. Rev. Lett. **109**, 037603, (2012).

[OST15] N. Ogawa, S. Seki and Y. Tokura, *Ultrafast optical excitation of magnetic skyrmions*, Sci. Rep. **5**, 9552, (2015).

[Pat68] C. E. Patton, *Linewidth and Relaxation Processes for the Main Resonance in the SpinWave Spectra of Ni–Fe Alloy Films*, J. Appl. Phys. **39**, 3060, (1968).

[PCM12] N. A. Porter, G. L. Creeth and C. H. Marrows, *Magnetoresistance in polycrystalline and epitaxial $Fe_{1-x}Co_xSi$ thin films*, Phys. Rev. B **86**, 064423, (2012).

[PGM14] N. A. Porter, J. C. Gartside and C. H. Marrows, *Scattering mechanisms in textured FeGe thin films: Magnetoresistance and the anomalous Hall effect*, Phys. Rev. B **90**, 024403, (2014).

[Poo67] C. P. Poole, *Electron Spin Resonance — A Comprehensive Treatise on Experimental Techniques*. Interscience Publishers, New York, (1967).

[Rez13] S. M. Rezende, R. L. Rodríguez-Suárez, M. M. Soares, L. H. Vilela-Leão, D. Ley Domínguez and A. Azevedo, *Enhanced spin pumping damping in yttrium iron garnet/Pt bilayers*, Appl. Phys. Lett. **102**, 012402, (2013).

[Rom13] N. Romming, C. Hanneken, M. Menzel, J. E. Bickel, B. Wolter, K. von Bergmann, A. Kubetzka and R. Wiesendanger, *Writing and Deleting Single Magnetic Skyrmions*, Science **341**, 636, (2013).

[RWV94] S. Ramo, J. Whinnery and T. Van Duzer, *Fields and Waves in Communication Electronics*. John Wiley and Sons, New York, (1994).

[Sam13] J. Sampaio, V. Cros, S. Rohart, A. Thiaville and A. Fert, *Nucleation, stability and current-induced motion of isolated magnetic skyrmions in nanostructures*, Nat. Nanotech. **8**, 839, (2013).

[Sar43] R. I. Sarbacher, *Hyper and Ultrahigh Frequency Engineering*. Wiley, New York, (1943).

[SCH10] A. A. Serga, A. V. Chumak and B. Hillebrands, *YIG magnonics*, J. Phys. D: Appl. Phys. **43**, 264002, (2010).

[Sch12] T. Schulz, R. Ritz, A. Bauer, M. Halder, M. Wagner, C. Franz, C. Pfleiderer, K. Everschor, M. Garst and A. Rosch, *Emergent electrodynamics of skyrmions in a chiral magnet*, Nat. Phys. **8**, 301, (2012).

[Sch15] T. Schwarze, J. Waizner, M. Garst, A. Bauer, I. Stasinopoulos, H. Berger, C. Pfleiderer and D. Grundler, *Universal helimagnon and skyrmion excitations in metallic, semiconducting and insulating chiral magnets*, Nat. Mater. **14**, 478, (2015).

[Sch16] M. A. W. Schoen, D. Thonig, M. L. Schneider, T. J. Silva, H. T. Nembach, O. Eriksson, O. Karis and J. M. Shaw, *Ultra-low magnetic damping of a metallic ferromagnet*, Nat. Phys. **12**, 839, (2016).

[Sek12] S. Seki, X. Z. Yu, S. Ishiwata and Y. Tokura, *Observation of Skyrmions in a Multiferroic Material*, Science **336**, 198, (2012).

[Sek16] S. Seki, Y. Okamura, K. Kondou, K. Shibata, M. Kubota, R. Takagi, F. Kagawa, M. Kawasaki, G. Tatara, Y. Otani and Y. Tokura, *Magnetochiral nonreciprocity of volume spin wave propagation in chiral-lattice ferromagnets*, Phys. Rev. B **93**, 235131, (2016).

[Sil99] T. J. Silva, C. S. Lee, T. M. Crawford and C. T. Rogers, *Inductive measurement of ultrafast magnetization dynamics in thin-film Permalloy*, J. Appl. Phys. **85**, 7849, (1999).

[Sim01] R. N. Simons, *Coplanar Waveguide Circuits, Components, and Systems*. John Wiley and Sons Inc., New York, (2001).

[SIT12] S. Seki, S. Ishiwata and Y. Tokura, *Magnetoelectric nature of skyrmions in a chiral magnetic insulator Cu2OSeO3*, Phys. Rev. B **86**, 060403, (2012).

[SL60] E. G. Spencer and R. C. LeCraw, *Spin-Lattice Relaxation in Yttrium Iron Garnet*, Phys. Rev. Lett. **4**, 130, (1960).

[SLK61] M. Sparks, R. Loudon and C. Kittel, *Ferromagnetic relaxation. I. Theory of the relaxation of the uniform precession and the degenerate spectrum in insulators at low temperatures*, Phys. Rev. **122**, 791, (1961).

[Spa64] M. Sparks, *Ferromagnetic-Relaxation Theory*. McGraw-Hill, New York, (1964).

[ST63] A. J. Sievers and M. Tinkham, *Far Infrared Antiferromagnetic Resonance in MnO and NiO*, Phys. Rev. **129**, 1566, (1963).

[Sta93] D. D. Stancil, *Theory of Magnetostatic Waves*. Springer, New York, (1993).

[Tab14] Y. Tabuchi, S. Ishino, T. Ishikawa, R. Yamazaki, K. Usami and Y. Nakamura, *Hybridizing Ferromagnetic Magnons and Microwave Photons in the Quantum Limit*, Phys. Rev. Lett. **113**, 083603, (2014).

[Tok15] Y. Tokunaga, X. Z. Yu, J. S. White, H. M. Ronnow, D. Morikawa, Y. Taguchi and Y. Tokura, *A new class of chiral materials hosting magnetic skyrmions beyond room temperature*, Nat. Commun. **6**, 7638, (2015).

[VB10] V. Vlaminck and M. Bailleul, *Spin-wave transduction at the submicrometer scale: Experiment and modeling*, Phys. Rev. B **81**, 014425, (2010).

[Vla08] V. Vlaminck, *Décalage Doppler d'onde de spin induit par un courant électrique*. PhD thesis, Université Louis Pasteur, Strasbourg, (2008).

[Wai13] J. Waizner, *Dynamics in chiral magnets - magnetic and electric excitations of helices and skyrmions*. Diploma thesis, Univ. of Cologne, (2013).

[WCS15] Y. Wei, S. L. Chin and P. Svedlindh, *On the frequency and field linewidth conversion of ferromagnetic resonance spectra*, J. Phys. D: Appl. Phys. **48**, 335005, (2015).

[Wen69] C. P. Wen, *Coplanar waveguide: a surface strip transmission line suitable for nonreciprocal gyromagnetic device applications*, IEEE Trans. Microw. Theory Techn. **17**, 1087, (1969).

[Wie14] B. M. Wiedemann, *Magnetic and Structural Properties of Fe and MnSi Thin Films Investigated by Scat-*

tering Techniques. PhD thesis, Technische Universität München, (2014).

[Wie16] R. Wiesendanger, *Nanoscale magnetic skyrmions in metallic films and multilayers: a new twist for spintronics*, Nat. Rev. Mater. **1**, 16044, (2016).

[Wil13] M. N. Wilson, E. A. Karhu, D. P. Lake, A. S. Quigley, S. Meynell, A. N. Bogdanov, H. Fritzsche, U. K. Rößler and T. L. Monchesky, *Discrete helicoidal states in chiral magnetic thin films*, Phys. Rev. B **88**, 214420, (2013).

[Woo16] S. Woo, K. Litzius, B. Kruger, M.-Y. Im, L. Caretta, K. Richter, M. Mann, A. Krone, R. M. Reeve, M. Weigand, P. Agrawal, I. Lemesh, M.-A. Mawass, P. Fischer, M. Klaui and G. S. D. Beach, *Observation of room-temperature magnetic skyrmions and their current-driven dynamics in ultrathin metallic ferromagnets*, Nat. Mater. **15**, 501, (2016).

[WTM08] T. Weiland, M. Timm and I. Munteanu, *A practical guide to 3-D simulation*, IEEE Microwave Magazine **9**, 62, (2008).

[Yas16] T. Yasukawa, A. J. Sigillito, B. C. Rose, A. M. Tyryshkin and S. A. Lyon, *Addressing spin transitions on* ^{209}Bi *donors in silicon using circularly polarized microwaves*, Phys. Rev. B **93**, 121306, (2016).

[YJ11] X. Yao and N. A. F. Jaeger, *Ultra-wide-band coplanar waveguide based impedance transformer using slow-wave electrodes*, Proc. SPIE **8007**, 80070, (2011).

[Yok14] T. Yokouchi, N. Kanazawa, A. Tsukazaki, Y. Kozuka, M. Kawasaki, M. Ichikawa, F. Kagawa and Y. Tokura,

Stability of two-dimensional skyrmions in thin films of $Mn_{1-x}Fe_xSi$ investigated by the topological Hall effect, Phys. Rev. B **89**, 064416, (2014).

[Yu16] G. Yu, P. Upadhyaya, X. Li, W. Li, S. K. Kim, Y. Fan, K. L. Wong, Y. Tserkovnyak, P. K. Amiri and K. L. Wang, *Room-Temperature Creation and Spin–Orbit Torque Manipulation of Skyrmions in Thin Films with Engineered Asymmetry*, Nano Lett. **16**, 1981, (2016).

[Zak07] K. Zakeri, J. Lindner, I. Barsukov, R. Meckenstock, M. Farle, U. von Hörsten, H. Wende, W. Keune, J. Rocker, S. S. Kalarickal, K. Lenz, W. Kuch, K. Baberschke and Z. Frait, *Spin dynamics in ferromagnets: Gilbert damping and two-magnon scattering*, Phys. Rev. B **76**, 104416, (2007).

[Zan11] J. Zang, M. Mostovoy, J. H. Han and N. Nagaosa, *Dynamics of Skyrmion Crystals in Metallic Thin Films*, Phys. Rev. Lett. **107**, 136804, (2011).

[ZD11] I. Zutic and H. Dery, *Spintronics: Taming spin currents*, Nat. Mater. **10**, 647, (2011).

[ZEZ15] X. Zhang, M. Ezawa and Y. Zhou, *Magnetic skyrmion logic gates: conversion, duplication and merging of skyrmions*, Sci. Rep. **5**, 9400, (2015).

[Zha14] X. Zhang, C.-L. Zou, L. Jiang and H. X. Tang, *Strongly Coupled Magnons and Cavity Microwave Photons*, Phys. Rev. Lett. **113**, 156401, (2014).

[Zha16] S. L. Zhang, A. Bauer, D. M. Burn, P. Milde, E. Neuber, L. M. Eng, H. Berger, C. Pfleiderer, G. van

der Laan and T. Hesjedal, *Multidomain Skyrmion Lattice State in Cu_2OSeO_3*, Nano Letters **16**, 3285, (2016).

[Zhe96] G. Zheng, M. Pardavi Horvath, X. Huang, B. Keszei and J. Vandlik, *Experimental determination of an effective demagnetization factor for nonellipsoidal geometries*, J. Appl. Phys. **79**, 5742, (1996).

[Ziv02] R. Zivieri, P. Vavassori, L. Giovannini, F. Nizzoli, E. E. Fullerton, M. Grimsditch and V. Metlushko, *Stokesanti-Stokes Brillouin intensity asymmetry of spin-wave modes in ferromagnetic films and multilayers*, Phys. Rev. B **65**, 165406, (2002).

List of Figures

Figure 1	Schematic representation of a chiral Skyrmion	vii
Figure 1.1	Angle definition for the crystal anisotropy energy	6
Figure 1.2	Precessional motion of the macrospin	8
Figure 1.3	Real and imaginary parts of the dynamic susceptibility $\chi_{xx}(f)$	12
Figure 1.4	Ellipticity in a ferromagnet	16
Figure 1.5	Crystal structure of Cu_2OSeO_3	18
Figure 1.6	Spin configuration in the spin helix phases	19
Figure 1.7	Phase diagram of Cu_2OSeO_3	20
Figure 1.8	Sketch of the Skyrmion lattice	21
Figure 1.9	Eigenmodes of the spin helix	28
Figure 1.10	Eigenmodes of the Skyrmion lattice	30
Figure 1.11	Resonance frequencies in a spere of a chiral magnet	31
Figure 2.1	Equivalent circuit of a high-frequency transmission line section	34
Figure 2.2	Illustration of the S-parameters and normalized waves	41
Figure 2.3	CPWs used in this thesis	44
Figure 2.4	Near-field distribution of the broad CPW	47
Figure 2.5	Far-field distribution of the broad CPW	49
Figure 2.6	Field distribution of the narrow CPW	50
Figure 2.7	Field distribution of the antenna-CPW	52
Figure 2.8	Wave vector distribution for the broad CPW	54

Figure 2.9	Wave vector distribution for the narrow CPW	56
Figure 2.10	Wave vector distribution for the antenna-CPW	57
Figure 2.11	Photograph of the LHe-flow cryostat apparatus	59
Figure 2.12	Photograph of the cryostat chamber	61
Figure 2.13	Schematic overview of the PIMM setup	66
Figure 2.14	Comparison between TDR and TDT waveforms	67
Figure 2.15	Photograph of the VTI and vector magnet	71
Figure 2.16	Schematic diagram of the VTI	72
Figure 2.17	Photograph of the VTI sample stage.	73
Figure 2.18	Angle definition for the VTI measurements	74
Figure 2.19	Optical lithography steps	78
Figure 3.1	Conformal map	83
Figure 3.2	Odd and even CPW modes	84
Figure 3.3	Design parameters of the narrow CPW	88
Figure 3.4	Exponential taper	90
Figure 4.1	Spectra in the field-polarized phase of Cu_2OSeO_3 at 5 K	94
Figure 4.2	Temperature and frequency dependent linewidths Δf at 5 K	95
Figure 4.3	Temperature and frequency dependent linewidths ΔH	96
Figure 4.4	Temperature-dependent intrinsic damping parameter α_{intr} and inhomogeneous broadening Δf_0	97
Figure 4.5	Analysis of the sharp modes recorded with the narrow CPW	99
Figure 4.6	Additional data recorded on sample **C**	100
Figure 4.7	Detailed analysis of the sharp modes for $\mathbf{H} \parallel \langle 111 \rangle$	102

Figure 4.8 Field-independent frequency splitting of standing BVMSWs 105
Figure 4.9 Comparison between theoretical and experimental resonance frequencies 106
Figure 4.10 Determination of the cubic anisotropy constant at 5 K 109
Figure 5.1 Spectra from various placements of the Cu_2OSeO_3 bar-shaped sample 113
Figure 5.2 Comparison of measured and calculated resonance frequencies 114
Figure 5.3 Ellipticity and spectral weight of the spin helix modes 118
Figure 5.4 Linear polarization of the spin helix precession 121
Figure 5.5 Ellipticity and spectral weight in the Skyrmion lattice phase 122
Figure 5.6 Effective dynamic susceptibility in different phases of Cu_2OSeO_3 126
Figure 5.7 Cubic anisotropy at high temperatures . . 128
Figure 5.8 Color-coded data recored with the VTI . 130
Figure 5.9 Time-resolved zero-field data of the conical eigenmodes 134
Figure 5.10 Relaxation time and damping of the conical eigenmodes 135
Figure 5.11 Beating pattern at 20 K and 70 mT 137
Figure 5.12 Frequency spectrum at 20 K and 70 mT . 138
Figure 5.13 Dephasing of the conical eigenmode $-Q$ 139
Figure B.1 Design parameter set of the narrow and antenna-CPW 149

Acknowledgements

Hereby I wish to express my gratitude to the following people that provided me with invaluable help throughout this work:

- **Prof. N. N.** for supervision of the PhD examination, **Prof. Dirk Grundler** for being the first examiner and **Prof. Christian Pfleiderer** for being the second examiner.
- **Prof. Dirk Grundler** for offering me the chance of working at E10 and supervising my work. His enthusiasm always boosted my excitement about physics and experimental work, and his valuable advice was of great help regarding technical and physical problems. I greatly appreciate the trust, freedom, support and respect he gave my work and ideas, his guidance and disposition at all times. Last but not least, his advice extended beyond scientific aspects over to formal issues, funding applications, student supervision, teaching and safety at work, which proved to be valuable skills for my past and future activities.
- **Prof. Christian Pfleiderer** For the opportunity to collaborate with his group in the exciting field of Skyrmions and his support to our group in the last months.
- **Dr. Andreas Bauer** for providing the samples. Additionaly, his vast knowledge and experience regarding Skyrmion-related research, which he openly shared with me during numerous lengthy discussions were highly valuable for my

work. Last but not least, I always admired his commitment in our collaboration activities and disposition at all times.

- **PD Dr. Markus Garst** and **Johannes Wainzer** for the long, fruitful collaboration by bringing in their expertise in the theoretical modelling of our measurements. Their enthusiasm regarding our experimental data and their strive to capture the exciting physics of chiral magnets was uninterrupted. Also, the friendly informal atmosphere that surrounded us throughout our work and common activities was never missing.
- **The students** Stefan Weichselbaumer, Petio Natzkin, Filip Lisiecki, Sho Watanabe, Markus Kleinhans and Hiroto Sakimura, who engaged in their scientific activities with great enthusiasm, eager for knowledge, provided great support and contributed additional skills but also cheerfulness to our group.
- **Dipl. Ing. Susanne Mayr** working at the crystal lab of the physics department for preparing the samples for our measurements with great care and reliability.
- **Further collaboration partners:** Prof. Alois Loidl, Dr. Hans-Albrecht Krug von Nidda, Dieter Ehlers, Prof. Istvan Kézsmárki, Prof. T. Hesjedal, S. Zhang, Laura Köhler and Jan Müller
- **My colleagues at our chair**, Stefan Mändl, Stephan Albert, Vinayak Bhat, Florian Heimbach, Florian Herzog, Florian Brandl, Schorsch Sauther, Haiming Yu, Matthias Dodenhöft and Korbinian Baumgärtl for providing a pleasant working atmosphere in our group. Many thanks especially to Marc Wilde for his valuable advice regarding administration, safety in the lab and technical issues.

- **Dr. Rupert Huber** for giving me and my fellow students that enlightening and inspiring 15-minute lab tour after supervising us during our lab course in 2012. Rupert's initiative triggered my interest in spin waves and persuaded me to join the research at our chair.
- **The technical staff** Thomas Rapp, Stephan Lichtenauer, Johannes Seitz, Herbert Hetzl, Thomas Neukel, Mafred Pfaller and his team at the workshop for the immediate and skilled support on technical matters. Also Marco Halder from E51 for his valuable advice on measurement techniques and control systems.
- **Claudine Voelcker** for her effective and friendly support with administration and organisational matters. Many thanks also to **Silvia Petat** and **Chenh Dung Lai** for support with matters of the SFB/TRR80 research programe.
- **My friends**, in which I also count my former supervisor Dr. Thomas Schwarze, that supported me and accompanied me in numerous activities outside the lab.
- **My parents**, who always stood by me throughout my studies providing endless support and comfort.
- **The Deutsche Forschungsgemeinschaft (DFG)** for funding through project DFG/SFB/TRR80 "From electronic correlations to functionality". Financial support from the TUM-Graduate School, the German Physical Society (DPG) and the "Wilhelm und Else Heraeus-Stiftung" is gratefully acknowledged.

List of Publications

- I. Stasinopoulos, A. Bauer, H. Berger, C. Pfleiderer, and D. Grundler, *Time-resolved spin helix dynamics in the chiral magnet Cu_2OSeO_3*, in preparation
- I. Stasinopoulos, S. Weichselbaumer, A. Bauer, J. Waizner, H. Berger, S. Maendl, M. Garst, C. Pfleiderer, and D. Grundler, *Low spin wave damping in the insulating chiral magnet Cu_2OSeO_3*, submitted (2016)
- I. Stasinopoulos, S. Weichselbaumer, A. Bauer, J. Waizner, H. Berger, M. Garst, C. Pfleiderer, and D. Grundler, *Discovery of linearly polarized GHz magnetization dynamics in the chiral ferrimagnetic insulator Cu_2OSeO_3*, submitted (2016)
- S. L. Zhang, I. Stasinopoulos, T. Lancaster, F. Xiao, A. Bauer, F. Rucker, A. A. Baker, A. I. Figueroa, Z. Salman, F. L. Pratt, S. J. Blundell, T. Prokscha, A. Suter, J. Waizner, M. Garst, D. Grundler, G. van der Laan, C. Pfleiderer, and T. Hesjedal, *Room-temperature helimagnetism in FeGe thin films*, Sci. Rep. **7**, 123 (2017)
- D. Ehlers, I. Stasinopoulos, I. Kézsmárki, T. Fehér, V. Tsurkan, H.-A. Krug von Nidda, D. Grundler, and A. Loidl, *Exchange anisotropy in the skyrmion host GaV_4S_8*, J. Phys. Cond. Mat. **29**, 065803 (2016)
- D. Ehlers, I. Stasinopoulos, V. Tsurkan, H.-A. Krug von Nidda, T. Fehér, A. Leonov, I. Kézsmárki, D. Grundler, and

A. Loidl, *Skyrmion dynamics under uniaxial anisotropy*, Phys. Rev. B **94**, 014406 (2016)

- V. S. Bhat, F. Heimbach, I. Stasinopoulos, and D. Grundler, *Magnetization dynamics of topological defects and the spin solid in a kagome artificial spin ice*, Phys. Rev. B **93**, 140401 (2016)
- T. Schwarze, J. Waizner, M. Garst, A. Bauer, I. Stasinopoulos, H. Berger, C. Pfleiderer and D. Grundler, *Universal helimagnon and skyrmion excitations in metallic, semiconducting and insulating chiral magnets*, Nat. Mater. **14**, 478 (2015)
- Haiming Yu, O. d'Allivy Kelly, V. Cros, R. Bernard, P. Bortolotti, A. Anane, F. Brandl, R. Huber, I. Stasinopoulos and D. Grundler, *Magnetic thin-film insulator with ultra-low spin wave damping for coherent nanomagnonics*, Sci. Rep. **4**, 6848 (2014)